12-14-2017

Ultrafast Processes in 2d Materials

Seyyedeh Azar Oliaei Motlagh

Recommended Citation

Oliaei Motlagh, Seyyedeh Azar, "Ultrafast Processes in 2d Materials." Dissertation, Georgia State University, 2017.
doi: https://doi.org/10.57709/11161062

ULTRAFAST PROCESSES IN 2D MATERIALS

by

SEYYEDEH AZAR OLIAEI MOTLAGH

Under the Direction of Mark I. Stockman, PhD

ABSTRACT

In this dissertation, we study theoretically ultrafast processes accessible via the interaction of the ultrafast and intense laser pulses with 2D materials. The ultrafast and strong laser pulse has a duration of a few femtoseconds, and the amplitude of the electric field is about several V/Å. We investigate the ultrafast electron dynamics in graphene, on a surface of a 3D topological insulator, and on a surface of a 3D crystalline topological insulator. Due to the gapless structure of graphene, surface states of the 3D topological insulator, and a 3D crystalline topological insulator, the electron dynamics is highly irreversible. The irreversibility of the electron dynamics is characterized by nonzero conduction band population in the reciprocal space after the pulse ends. Unlike graphene, electron dynamics on the surface of the 3D topological insulator is chiral in the presence of a single cycle of a circularly polarized pulse. We define the chirality of electron dynamics using the distribution of the residual conduction band population in the reciprocal space. The chirality of the electron dynamics of a 3D topological insulator is due to a cubic term known as a hexagonal warping term in the low energy Hamiltonian. This warping term breaks down the full rotational symmetry of the crystal to the threefold symmetry. Unlike graphene which has a linear energy dispersion at valleys in its Brillouin zone, the crystalline topological insulator has a quadratic energy dispersion at the M point in its (001) crystal face. The ultrafast electron dynamics on the surface of the crystalline topological insulator is anisotropic, i.e., the distribution of the residual conduction band population changes with the angle of the polarization of the applied linearly polarized pulse. For all different 2D materials studied in this work, applied ultrafast laser pulses generate ultrafast charge currents. The generated ultrafast currents follow the vector potentials of the pulse's electric fields. The asymmetric profile of the ultrafast electric current produces a nonzero transferred charge which also determines the final polarization of the materials.

INDEX WORDS: Ultrafast processes, 2D Material, Graphene, Topological insulator, Crystalline topological insulator, Ultrafast laser pulse, Electron dynamics, Current, Transferred charge, Electric field, Interband transition

ULTRAFAST PROCESSES IN 2D MATERIALS

by

SEYYEDEH AZAR OLIAEI MOTLAGH

A Dissertation Submitted in Partial Fulfillment of the Requirements for the Degree of

Doctor of Philosophy
in the College of Arts and Sciences
Georgia State University
2017

ULTRAFAST PROCESSES IN 2D MATERIALS

by

SEYYEDEH AZAR OLIAEI MOTLAGH

Committee Chair:	Mark I. Stockman
Committee:	Vadym Apalkov A. G. Unil Perera Alexander Kozhanov Fabien Baron

Electronic Version Approved:

Office of Graduate Studies
College of Arts and Sciences
Georgia State University
December 2017

DEDICATION

To my beloved parents,
and brothers.

ACKNOWLEDGEMENTS

”In the name of God, the Most Gracious, the Most Merciful”

I would like to express my most profound appreciation to Professor Mark I. Stockman and Professor Vadym Apalkov for their guidance and advice during the past three years. I believe that I am tremendously fortunate to have them as my advisors. My sincerest gratitude and thanks also go to my committee members, Professor A. G. Unil Perera, Professor Alexander Kozhanov, and Professor Fabien Baron for supporting the scientific ideas in my dissertation. I would like to express my sincerest gratitude to the lab coordinator Ms. Carola Butler who impressed me by her helpful proofreading-comments on my dissertation.

I am extending my thanks to the graduate adviser, Professor Xiaochun He, the chair of physics and astronomy department, Professor Mike Crenshaw and all professors at GSU for enriching classes. I would like to thank Dr. Jhih-Sheng Wu, my colleagues in the center for nano-optics, and all my friends.

I am extremely grateful to my parents, grandmother, brothers, aunts, and uncles for their continuous love, prayers, support, and encouragement. I am so lucky to have a great family.

TABLE OF CONTENTS

LIST OF FIGURES

LIST OF ABBREVIATIONS

- 1D - One dimensional
- 2D - Two dimensional
- 3D - Three dimensional
- BZ - Brillouin zone
- CTI - Crystalline topological insulator
- DFT - Density functional theory
- SOC - Spin-orbit coupling
- TB - Tight binding
- TDSE - Time-dependent Schrodinger equation
- TI - Topological insulator

CHAPTER 1

INTRODUCTION

1.1 Interaction of ultrashort optical pulses with solids

Advanced femtosecond and attosecond laser technologies lead to the availability of intense few-cycle laser pulses with the duration of few femtoseconds(1 fs=10^{-15} s). These laser pulses have electric field components which are comparable to binding fields of electrons in solids [2, 3, 4, 5, 6, 7]. Since the durations of ultrafast laser pulses are on the scale of femtosecond , transmitted energy as heat to solids is minimal [8] in these ultrafast pulse-matter interactions. Consequently, ultrafast laser technologies provide opportunities to study ultrafast and extermely nonlinear processes on attosecond to femtosecond time scales in solids. The availability of one-cycle intense laser pulses offers a unique opportunity to study and control nonperturbative and field-driven electron dynamics with high precision. [9, 2, 3, 4, 5, 6, 7]. In the following, we introduce a process associated with pulse-matter interactions.

1.1.1 Solids in Strong Fields

High intensity laser pulses cause nonlinear photoionizations of solids. Two well known photoionization processes are multiphoton ionization and tunnel ionization. The theory of photoionizations originated with Keldysh [17] who proposed an adiabatic parameter, γ, known as Keldysh parameter to indicate the regimes in which these two different photoionizations process happen

$$\gamma = \frac{\omega\sqrt{m^{*}\Delta_g}}{eF} \tag{1.1}$$

where ω is the frequency of applied pulses, m^{*} is the effective mass of an electron, Δ_g the bandgap of the solid, e is the electron mass, and F is the amplitude of the applied electric field [10, 11]. Depending on the Keldysh parameter, $\gamma >> 1$ or $\gamma << 1$ the multiphoton ionization or photo-induced tunneling respectively would be a dominant ionization process [11, 10, 12]. For gapless 2D materials $\gamma = 0$ photo-induced tunneling is more probable to happen.

In this chapter, we review several theoretical studies and experimental researches in the field of laser pulse-matter interactions.

1.1.2 Theoretical Approach to Laser Pulse-Matter Interactions

Field-driven electron dynamics in pulse-matter interactions have been a subject of massive theoretical and experimental researches [13, 6, 14, 15, 16, 17, 18, 19, 20, 21, 22, 23, 24, 25, 5, 26, 27, 28, 29]. In a general approach to a many-body system, time-dependent density-functional theory (DFT) is applied to an insulator subjected to an ultrafast laser pulse. Field-driven electron dynamics is quantum mechanically described by time dependent Kohn-Sham equations written in the velocity gauge [30]

$$i\hbar\frac{\partial}{\partial t}\psi_i(\mathbf{r},t) = \left[\frac{1}{2m}\left(p+\frac{e}{c}\mathbf{A}_{tot}\right)^2 + V_{ion}(\mathbf{r}) + \int d\mathbf{r}'\frac{e^2}{|\mathbf{r}-\mathbf{r}'|}n(\mathbf{r}',t) + V_{xc}(\mathbf{r},t)\right]\psi_i(\mathbf{r},t) \quad (1.2)$$

where $n(\mathbf{r},t) = \sum_i |\psi_i(\mathbf{r},t)|^2$ is the time dependent density, and $V_{xc}(\mathbf{r},t)$ is the exchange-correlation potential. The total vector potential $\mathbf{A}_{\text{tot}}$ is given by $\mathbf{A}_{\text{tot}} = \mathbf{A}_{\text{ext}} + \mathbf{A}_{\text{ind}}$ where $\mathbf{A}_{\text{ext}}$ is the vector potential of the applied field, and $\mathbf{A}_{\text{ind}}$ is the induced vector potential due to the induced polarization of solids . In the time-dependent Kohn-Sham equation, the pulse-matter interaction can be treated in the length gauge or the dipole approximation [31]

$$i\hbar\frac{\partial}{\partial t}\psi_i(\mathbf{r},t) = \left[-\frac{1}{2}\frac{\partial^2}{\partial\mathbf{r}^2} + V_{ion}(\mathbf{r}) + \int d\mathbf{r}'\frac{e^2}{|\mathbf{r}-\mathbf{r}'|}n(\mathbf{r}',t) + V_{xc}(\mathbf{r},t) + \mathbf{F}(t)\cdot\mathbf{r}\right]\psi_i(\mathbf{r},t) \quad (1.3)$$

where $\mathbf{F}(t)$ is the applied electric field component of the laser pulse. This method is applied to crystalline silicon subjected to a strong laser pulse with intensity $10^{10} - 10^{15}$ W/cm^2 and duration about 21 fs [32]. However, DFT requires large simulation and long processing time which is. not economically sufficient [33]

In semiclassical approach , the rate equation is used to describe the noncoherent electron dynamics [34]. In this approach, the carrier relaxation and generation times are taken into accounts. Also, the electric field of the pulse generates an electron-hole plasma through multiphoton and electron avalanche (impact) ionizations. In this model, these ionization processes are included in the rate equations. as below :

$$\frac{\partial n_e}{\partial t} = \frac{n_v - n_e}{n_v}(\omega_{PI} + n_e \omega_{II}) - \frac{n_e}{\tau_r} \tag{1.4}$$

where n_e is the electron density, n_v is the initial electron density in valence bands, ω_{PI} is photoionizaton in $cm^{-3}s^{-1}$ ω_{II} is avalace ionization rate in s^{-1}, and τ_r is a time constant.

To find coherent electron dynamics in solids subjected to ultrashort intense pulses with duration about 4 fs, the time dependent schrodinger equation is applied [26]

$$i\hbar\frac{\partial \Psi}{\partial t} = H\Psi \tag{1.5}$$

where $H = H_0 + eF(z,t)r$ and H_0 is tight binding Hamiltonian or low energy effective Hamiltonian derived by $k \cdot p$ perturbation theory, and F(z,t) is the electric field inside the material calculated from Maxwell's equations

$$\begin{aligned} \Delta \cdot \mathbf{D} &= 0 && (1.6)\\ \Delta \cdot \mathbf{B} &= 0 && (1.7)\\ \Delta \times \mathbf{F} &= -\frac{1}{c}\frac{\partial \mathbf{B}}{t} && (1.8)\\ \Delta \times \mathbf{B} &= \frac{1}{c}\frac{\partial \mathbf{F}}{\partial t} + \frac{4\pi}{c}\frac{\partial \mathbf{P}}{\partial t} && (1.9) \end{aligned}$$

where $\mathbf{B}$ is magnetic field, $\mathbf{F}$ is electric field, and $\mathbf{D} = \mathbf{F} + 4\pi\mathbf{P}$ is the electric displacement field.

This method is applied to a nanofilm of silica with a thickness of $\leq$ 150 nm which is subjected to ultrafast and intense laser pulses with the intensity of 1-3.6 V/Å, the frequency carrier about 1.5 eV, and duration of about 4 fs. The electron dynamics is predicted to be coherent, adiabatic, field-driven and deeply nonlinear [26].

The time-dependent Schrodinger equation describes electron dynamics in metallic nanofilms, gold, and silver, subjected to ultrafast laser pulses with electric field amplitude $>= 3V/\AA$ and subcycle times =< 1fs. The interaction of strong and ultrashort pulses with metallic nanofilms is predicted to decrease the reflectivity of metals and increase their transmissivity significantly. In this approach an effective 1D model is used to describe 3D lattice of perfect metals, gold, and silver. The Maxwell's equations are solved to describe the propagation of the pulse inside and outside of the metallic nanofilms where the time-dependent Schrodinger equation determines the quantum electron dynamics which govern the dielectric polarization of metallic nanofilms. The response of the nanofilms is predicted to be nonlinear and nonadiabatic due to the nonexistence of a band gap between the highest valence band and the lowest conduction band [27].

In continue of studying optical responses of different materials subjected to the ultrafast and intense laser pulses, 2D materials become subjects of theoretical study in this field.

1.1.3 2D Materials subjected to ultrafast Laser Pulses

2D materials have interesting properties which can make them capable of being used in electronics and optical applications.

Ultrafast and intense laser pulses with duration ≈4 fs and electric field amplitude of about few V/Å are normally applied to graphene and the time-dependent Schrodinger is solved for each initial k in the reciprocal space to find coherent electron dynamics [35]. Due to the unique dispersion relation of graphene, there are gapless points in the reciprocal space called K and K′ where the inter-band dipole matrix has a singularity [35]. The singularity of the interband dipole matrix leads to nonadiabatic and irreversible electron dynamics. After the pulse ends, there remain populations on the conduction band called residual conduction band populations. The residual conduction band population is used as a factor to determine the irreversibility of the electron system. Additionally, the distribution of residual conduction band population in the reciprocal space includes hotspots or fringes whose period does not change with changing the amplitude of the applied field [35].

Irreversibility in optical responses is predicted to be controlled in buckled Dirac materials [36, 37, 38, 39, 40, 41, 42, 43] by the component of the applied pulse which is normal to the surface and the propagation with respect to their orientation of crystallographic planes [44]. For example, silicene and germanene have buckled structures due to the larger reduces of Si and Ge atoms in comparison to the radius of C atom in graphene. Spin-orbit coupling in silicene and germanene opens energy gaps at Dirac points which can be controlled by the normal component of the applied field. Additionally, the normal component of the ultrafast field is predicted to generate a current normal to the plane and subsequently create a net transferred charge in the same direction [44].

In the following section, we review some experimental researches done in the field of ultrashort laser pulse-matter interactions.

1.1.4 Laser Pulse-Matter interactions in Experimental Researches

A few cycles of an intense optical pulse with the amplitude of the electric field $\approx 1(\mathrm{V/Å})$ was applied to the fused silica which has a band gap of about 9 eV [4]. The few cycles of the intense optical pulses were used to overcome dielectric breakdowns in strong fields. These experimental results proved that the ultrafast laser pulse generates an ultrafast electrical current. The generation of ultrafast current gives rise to the electrical polarization in this dielectric due to the nonzero transferred charge. Also, the results show that the current can be controlled by strong ultrafast fields turned on or off in the performance range of ≈ 1 fs. The experimental results [4] proved the predicted results of Ref [26].

In their experimental work, Kwon et al. tried to find out if semi metalization in the presence of an ultrashort optical pulse is a universal phenomenon for dielectrics regardless differences in their lattice structures [45]. To find a response for this critical question, they did experiments on three dielectrics: quartz, sapphire, and calcium fluoride. These dielectrics with band gaps 9 eV, 8.8 eV, and 12.2 eV have different lattice structures, rhombohedra, hexagonal, and cubic respectively. Under the weak fields their responses are based on their dielectric permittivities. The structural difference of these dielectrics makes the responses of these materials to weak fields different from each other. In contrast, they responded in the same way to applied ultrafast and intense electric fields. Their findings proved the universality of the semi metalization for all dielectrics belonging to various crystal structures. Zener-Keldyish tunneling formula does not well explain the semi metalization phenomena. However, it is well described by the quantum mechanical theoretical model suggested in Ref [26] which takes into account the interband and intraband coupling of electronic states.

Continuing the progress in experimental works done in the field of interaction of intense and ultrashort pulses with solids, a semiconductor, gallium nitride (GaN), was subjected to intense and ultrafast pulses [46]. Since GaN has a bandgap ≈ 3.4 eV which is smaller than the band-gaps of dielectrics, it has been demonstrated that the required field amplitudes for controlling the ultrafast current, are lower than those required for dielectrics[46]. As far as the frequency of the applied laser pulse (ω_L) satisfies the adiabatic condition $\omega_L << \Delta_g/\hbar$ where Δ_g is the band-gap of materials the response of materials to the laser pulse is reversible.

The most recent experimental work has been done on graphene in 2017. In this study, graphene is subjected to two-cycle laser pulses with the frequency of about 1.5 eV, duration of about 5.4 fs, and pulse amplitude of up to 0.31 V/Å [47]. It has been shown that a current induced in graphene depends on the electric field waveform which is modified by a carrier envelope phase [47]. Moreover, the dependence of the current on the amplitude of the applied linearly pulse is not monotonic. With an amplitude of about 0.2 V/Å the current changes its sign. This was explained by the overcoming of interband transition to intraband transitions in the strong field regime. The experimental results of this work agreed with the theoretical work which predicts that the interband transition happens instantaneously even for weak fields [47, 35].

1.2 Outline

In this chapter, we reviewed theoretical and experimental approaches to the subject of ultrafast laser pulse-matter interactions. In chapter 2, we explain the method that we use to simulate the interaction of the ultrafast and strong laser pulse with a 2D material theoretically and numerically. In chapter 3, we predict that ultrafast electrical responses of graphene subjected to linearly polarized pulses to be sensitive to field waveforms. In chapter 4, a topological insulator is subjected to ultrafast laser pulses; linear results of this paper is published in a conference paper [48]. In chapter 5, a crystalline topological insulator is subjected to an ultrafast linearly polarized pulse; the major part of this chapter is published in the Physical review B journal [49]. The last chapter includes the summary.

CHAPTER 2

METHODOLOGY

2.1 Main Equations

We start with the Hamiltonian of a 2D material, H_0, which is derived either by the tight-binding method for graphene or by $k \cdot p$ perturbation theory for 3D topological insulators (TIs) and the surface states of 3D crystalline topological insulators (CTIs) . The Hamiltonian H_0, depending on the type of 2D material, includes the spin-orbit coupling (SOC) term.

We apply the strong laser pulse to 2D materials graphene, the crystalline topological insulator (CTI), and the topological insulator (TI) to study ultrafast processes in the range of few femtosecond. In the presence of an intense laser pulse, the field-matter interaction term is written in the length gauge or the dipole approximation as the following expression

$$H^{\text{int}} = -e\mathbf{F}(t)\mathbf{r} \tag{2.1}$$

where $e\mathbf{r}$ is the dipole operator, e is elementary charge, and $\mathbf{F}(t) = (F_x(t), F_y(t))$ is the optical electric field. Therefor the total Hamiltonian is expressed as the following

$$H(t) = H_0 - e\mathbf{F}(t)\mathbf{r}, \tag{2.2}$$

To find the non-relativistic electron dynamics in 2D materials subjected to the strong and ultrafast laser pulse, we solve the time dependent Schrodinger equation (TDSE)

$$i\hbar\frac{d\Psi}{dt} = H(t)\Psi. \tag{2.3}$$

Intraband (within a single band) electron dynamics is determined by the Bloch acceleration theorem [50], which describes the electron intraband dynamics for both conduction and valence bands

$$\hbar \frac{d\mathbf{k}}{dt} = e\mathbf{F}(t). \tag{2.4}$$

For an electron with initial wave vector (lattice momentum) $\mathbf{q}$, the intraband electron dynamics is described by the time-dependent wave vector, $\mathbf{k(q,t)}$, which is given by the solution of Eq. (2.4)

$$\mathbf{k}(\mathbf{q},t) = \mathbf{q} + \frac{e}{\hbar}\int_{-\infty}^{t} \mathbf{F}(t_1)dt_1. \tag{2.5}$$

For solving TDSE in the presence of an applied weak field there are several approximation methods such as time dependent perturbation theory and time dependent WentzelKramersBrillouin (WKB) approximation [51, 52, 53]. Since in this study, the applied field is an intense pulse with the amplitude of the electric field in the range of 0.2-2 (V/Å), we solve the TDSE exactly. In the presence of this ultrafast field, we assume that the electron dynamics is coherent.The assumption that the dynamics is coherent is valid as long as the duration of the pulse, which is $\approx$ 4 fs, is less than the characteristic electron scattering time in these materials, which occur during times ranging from $\sim 10-20$ fs to $\sim 200-800$ fs [54, 55, 56, 57, 58, 59, 60, 61].

Based on these arguments, we neglect the electron collisions (dephasing) for a few fs duration of the excitation pulse and describe the electron dynamics as coherent by TDSE. The coherency of electron dynamics allows us to solve the TDSE independently for each point in the reciprocal space. using a time-step variant fourth-order Runge-Kutta method [62] for different 2D materials. The corresponding wave functions, which are solutions of Schrödinger equation (2.3) within a single band (α) approximation, i.e., without interband coupling, are the Houston functions [63],

$$\Phi^{(H)}_{\alpha\mathbf{q}}(\mathbf{r},t) = \Psi^{(\alpha)}_{\mathbf{k}(\mathbf{q},t)}(\mathbf{r}) e^{-\frac{i}{\hbar}\int_{-\infty}^{t} dt_1 E_\alpha[\mathbf{k}(\mathbf{q},t_1)]}, \tag{2.6}$$

A general solution of the TDSE is expressed in the basis of Houston functions $\Phi^{(H)}_{\alpha\mathbf{q}}(\mathbf{r},t)$

$$\Psi_{\mathbf{q}}(\mathbf{r},t) = \sum_{\alpha=c,v} \beta_{\alpha\mathbf{q}}(t)\Phi^{(H)}_{\alpha\mathbf{q}}(\mathbf{r},t), \tag{2.7}$$

where v, c denote the valence band and the conduction bands, respectively; $\beta_{\alpha\mathbf{q}}(t)$ are expansion coefficients.

For a two-band Hamiltonian with energies E_α and E_{α_1} and eigenfunctions $\left|\Phi^{(\alpha)}\right\rangle$ and $\left|\Phi^{(\alpha_1)}\right\rangle$ the expansion coefficients are found by replacing the general solution of the TDSE expressed in Eq. 2.7 into Eq. 2.3 as following

$$i\hbar\frac{d}{dt}\left(\beta_\alpha\left|\Psi^{(\alpha)}\right\rangle+\beta_{\alpha_1}\left|\Psi^{(\alpha_1)}\right\rangle\right)=(H_0-e\mathbf{rF})\left(\beta_\alpha\left|\Psi^{(\alpha)}\right\rangle+\beta_{\alpha_1}\left|\Psi^{(\alpha_1)}\right\rangle\right) \tag{2.8}$$

then

$$\begin{aligned}
&i\hbar\frac{d\beta_\alpha}{dt}\left|\Phi^{(\alpha)}\right\rangle\exp{(-\frac{i}{\hbar}\int E_\alpha dt)}+\beta_\alpha\left|\Phi^{(\alpha)}\right\rangle E_\alpha\exp{(-\frac{i}{\hbar}\int E_\alpha dt)}\\
&+i\hbar\frac{d\beta_{\alpha_1}}{dt}\left|\Phi^{(\alpha_1)}\right\rangle\exp{(-\frac{i}{\hbar}\int E_{\alpha_1}dt)}+\beta_{\alpha_1}\left|\Phi^{(\alpha_1)}\right\rangle E_{\alpha_1}\exp{(-\frac{i}{\hbar}\int E_{\alpha_1}dt)}\\
&=\beta_\alpha\left|\Phi^{(\alpha)}\right\rangle E_\alpha\exp{(-\frac{i}{\hbar}\int E_\alpha dt)}+e\mathbf{rF}\beta_\alpha\left|\Phi^{(\alpha)}\right\rangle\exp{(-\frac{i}{\hbar}\int E_\alpha dt)}\\
&+\beta_{\alpha_1}\left|\Phi^{(\alpha_1)}\right\rangle E_{\alpha_1}\exp{(-\frac{i}{\hbar}\int E_{\alpha_1}dt)}+e\mathbf{rF}\beta_{\alpha_1}\left|\Phi^{(\alpha_1)}\right\rangle\exp{(-\frac{i}{\hbar}\int E_{\alpha_1}dt)}
\end{aligned} \tag{2.9}$$

by multiplying two side of Eq.2.9 in $\left\langle\Phi^{(\alpha)}\right|$ since $\left\langle\Phi^{(\alpha)}\middle|\Phi^{(\alpha_1)}\right\rangle=0$ and $\left\langle\Phi^{(\alpha)}\middle|\Phi^{(\alpha)}\right\rangle=1$, $\left\langle\Phi^{(\alpha_1)}\middle|\Phi^{(\alpha_1)}\right\rangle=1$, we get

$$\frac{d\beta_{\alpha\mathbf{q}}(t)}{dt}=\left\langle\Phi^{(\alpha)}\right|e\mathbf{rF}\left|\Phi^{(\alpha_1)}\right\rangle\beta_{\alpha_1\mathbf{q}}\exp{(-\frac{i}{\hbar}\int[E_{\alpha_1}-E_\alpha]dt)} \tag{2.10}$$

by multiplying two sides of Eq. 2.9 in $\left\langle\Phi^{(\alpha_1)}\right|$, we get

$$\frac{d\beta_{\alpha_1\mathbf{q}}(t)}{dt}=\left\langle\Phi^{(\alpha_1)}\right|e\mathbf{rF}\left|\Phi^{(\alpha)}\right\rangle\beta_{\alpha\mathbf{q}}\exp{(-\frac{i}{\hbar}\int[E_\alpha-E_{\alpha_1}]dt)} \tag{2.11}$$

where $\left\langle\Phi^{(\alpha_1)}\right|e\mathbf{r}\left|\Phi^{(\alpha)}\right\rangle$ is the interband dipole matrix element,$D_{\alpha\alpha_1}$ which can be derived in the momentum space as following

$$D_{\alpha\alpha_1}=\frac{\hbar}{i}\frac{\left\langle\Phi^{(\alpha_1)}\right|\hat{V}\left|\Phi^{(\alpha)}\right\rangle}{E_\alpha-E_{\alpha_1}} \tag{2.12}$$

in which $\hat{V} = \frac{1}{\hbar}\frac{\partial H_0}{\partial k}$ is the matrix element of the velocity operator. Two equations 2.10 and 2.11 can be generalized to be used for any n-band Hamiltonian

$$\frac{d\beta_{\alpha\mathbf{q}}(t)}{dt} = -\frac{i}{\hbar}\sum_{\alpha_1\neq\alpha}\mathbf{F}(t)\mathbf{Q}_{\alpha\alpha_1,\mathbf{q}}(t)\beta_{\alpha_1\mathbf{q}}(t), \tag{2.13}$$

where $\alpha, \alpha_1 \in \{1, 2, , 3, ..., n\}$

$$\mathbf{Q}_{\alpha\alpha_1,\mathbf{q}}(t) = \mathbf{D}_{\alpha\alpha_1}[\mathbf{k}(\mathbf{q},t)] \times \exp\left(-\frac{i}{\hbar}\int dt\left(E_\alpha[\mathbf{k}(\mathbf{q},t)] - E_{\alpha_1}[\mathbf{k}(\mathbf{q},t)]\right)\right), \tag{2.14}$$

$$\mathbf{D}_{\alpha\alpha_1}[\mathbf{k}(\mathbf{q},t)] = \left\langle\Psi_k^{(\alpha)}|e\mathbf{r}|\Psi_k^{(\alpha_1)}\right\rangle. \tag{2.15}$$

Here $\Psi_{\mathbf{k}}^{(\alpha)}$ are eigenfunctions of the Hamiltonian without an optical field, H_0 where $\alpha \in \{v, c\}$, and $\mathbf{D}_{\alpha\alpha_1}$ is the interband dipole matrix element, which determines optical transitions between the valence and conduction band. We solve numerically the system of equations (2.13) with an initial condition that the valence band is occupied and the conduction bands are empty ($\beta_{v\mathbf{q}} = 1$). We characterize the corresponding electron dynamics for all 2D materials (TMDC, graphene, CTI, and TI) in terms of the conduction band (CB) population, generated electric charge current, and the transferred charge. Additionally, spin current, transferred spin, and magnetization are calculated for TIs and valley and spin polarization for TMDCs. The time-dependent CB population is defined as $N_{CB}(\mathbf{q},t) = |\beta_{c\mathbf{q}}(t)|^2$, after the pulse ends, there remains population in CB called the residual value of CB population, $N_{CB}^{(res)}(\mathbf{q})$. The residual conduction band population is a measure of the irreversibility of the optical process. In this work, we study both $N_{CB}^{(res)}(\mathbf{q})$ as a function of lattice momentum and the net residual CB population

$$N^{(res)} = \sum_{\mathbf{q}} N_{CB}^{(res)}(\mathbf{q}). \tag{2.16}$$

The electric current, $\mathbf{J}(t) = (J_x(t), J_y(t))$, generated during the pulse is determined by the following expression

$$J_j(t) = \frac{e}{a^2} \sum_{\mathbf{q}} \sum_{\alpha_1,\alpha_2=v,c} \beta^*_{\alpha_1\mathbf{q}} V_{j}^{\;\alpha_1\alpha_2} \beta_{\alpha_2\mathbf{q}}(t), \tag{2.17}$$

where $p = x, y$, a is the lattice constant, and $V_p^{\alpha_1\alpha_2}$ are the matrix elements of the velocity operator calculated between the CB and VB states. Two components of the interband dipole matrix element can be calculated from the following expressions

$$V_x^{cv} = iD_x(\mathbf{k})[E_c(\mathbf{k}) - E_v(\mathbf{k})]/\hbar, \tag{2.18}$$

$$V_y^{cv} = iD_y(\mathbf{k})[E_c(\mathbf{k}) - E_v(\mathbf{k})]/\hbar, \tag{2.19}$$

Transferred charge is a result of the charge current and describes the residual polarization of the system

$$Q_{tr,p} = \int_{-\infty}^{\infty} dt J_p(t) \tag{2.20}$$

For TI, since the spin of electron is locked to its momentum, in addition to the charge current and transferred charge, spin current and transferred spin are calculated.
The expression for the spin current is the following expression

$$J_p^{S_j}(t) = (\Delta q_x)(\Delta q_y) \sum_{\mathbf{q}} \sum_{\alpha=v,c} \beta^*_{\alpha_1\mathbf{q}}(t) S_j^{\alpha} V_p^{\alpha}(k) \beta_{\alpha_2\mathbf{q}}(t), \tag{2.21}$$

where $S_j^\alpha = \left\langle \Psi_k^{(\alpha)} | \sigma_j | \Psi_k^{(\alpha)} \right\rangle$, $j = x, y$, and z. Also the net transferred spin is nonzero for TI due to the generated spin current

$$S_{tr,p}^{j} = \int_{-\infty}^{\infty} dt J_p^{S_j}(t) \tag{2.22}$$

2.2 Numerical Approach to Solve Main Equations

To find electron dynamics in 2D materials subjected to ultrafast and intense laser pulses Eq. 2.13 should be solved . Eq. 2.13 is the first order differential equation which has the following form

$$\begin{aligned} y'(t) &= f(t,y) \\ y(t_0) &= y_0, \end{aligned} \tag{2.23}$$

Unfortunately there is not any analytical solution for this equation. However, there are many advanced numerical methods to solve the first order differential equations (Eq.2.23) which are classified in two major categories, linear multistep methods and Runge-Kutta methods. Linear multistep methods include Adams-Moulton method, backward differentiaton method (BDF), and Adams-Bashforth method. Classic fourth-order method , Forfarded Euler method, Heun's method, Fehlberg RK1 method, and Dormand-Prince method are examples of Runge-Kutta methods.

In general, Runge-Kutta methods calculate $f(t,y)$ multiple times to find higher accuracy. A scheme of a classical 4th-order Runge-Kutta methods can be expressed as the following [64, 65, 66]

$$\begin{aligned} y_{n+1} &= y_n + \frac{h}{6}(K_0 + 2K_1 + 2K_2 + K_3) \\ K_0 &= f(t_n, y_n) \\ K_1 &= f(t_n + \frac{h}{2}, y_n + \frac{h}{2}K_0) \\ K_2 &= f(t_n + \frac{h}{2}, y_n + \frac{h}{2}K_1) \\ K_3 &= f(t_n + h, y_n + hK_2) \end{aligned}$$

where h is the step size. More frequently the Runge-Kutta methods are used in pairs, which means a low-order Runge-Kutta method and a higher-order Runge-Kutta method are computed with the same evolution. One of the most popular Runge-Kutta method pairs is Dorman-Prince 4(5) [67]. Dormand-Prince 4(5) computes seven different slopes K_0, K_1, K_2 ,K_3, K_4, K_5,and K_6 used to find two approximation of the next point, $O(h^4)$ and $O(h^5)$. In this method, the error in the low-order method is estimated by the difference between two methods [67]. Additionally, this method uses various step size to minimize the error.

To calculate Eq. 2.13 numerically we use the ode45 solver, the first recommended choice, in MATLAB which is based on Dorman-Prince 4(5) [68].

Parallel Processing in MATLAB To calculate eq. 2.13 numerically we use the parallel processing in MATLAB [69, 70, 71] to decrease the processing time .

In general, there are two primary parallelism methods, known as shared-memory multiprocessors and distributed-memory multiprocessors [72, 73]. The main difference between these methods is the memory that they use. In shared-memory multiprocessors, all processors use a single memory. However, in distributed-memory multiprocessors, all processors have their local memory.

Both parallelism methods have issues and advantages. For example, in shared-memory multiprocessors, an issue known as race condition arises when two processors change one or more variables at the same time. To solve this issue, several synchronizing methods are suggested to lock a section of the code to one processor. Although this method is easy to use in coding, its delay time of execution due to a shared access bus from all processors to the shared memory is remarkable.

In another hand, the distributed-memory multiprocessors method provides a bus to a processor to connect to its local memory and speeds up the executions. However, there are issues with this method if processors need computed data from other processors during execution time. Complex synchronization methods solve these problems. Nowadays, distributed-memory multiprocessors method is a standard method for scaling networks inexpensively.

We write our codes in MATLAB to calculate electron dynamics numerically in 2D materials. The significant part of the processing time is consumed in processing for-loops in our codes. Therefore we use the advantage of parallel processing in MATLAB and replace a for-loop with a parfor loop which is a MATLAB built-in function based on distributed-memory multiprocessors method [69].

CHAPTER 3

GRAPHENE

3.1 Introduction

Graphene is a truly 2D material which is made of carbon atoms located in honeycomb lattices. Graphene is known as a 2D Dirac material with interesting electrical properties. Graphene is the basic building block of well-known 3D graphite, 1D nanotubes, and 0D fullerenes [74, 75, 76]. For close to 500 years graphite has been known as a mineral and scientists have known that graphite is a layered material bound together by the weak van der Wals interactions [77]. However, it took a long time for graphene to be formed experimentally for two main reasons. The first reason is that it was expected to be thermodynamically unstable [78]. The second reason is the lack of sensing devices capable of searching for one-atom-thick graphene. In the following section, the crystal structure of graphene is explained since it can be used to explain some electrical properties of graphene.

3.1.1 Crystal Structure of Graphene

From the chemical point of view, the chemical structure of graphene has sp^2 hybridization [79]. In quantum mechanics any superposition of $|2s\rangle$ orbital and $n\,|2p\rangle$ orbitals is called sp^n hybridization. Based on this description, for graphene, the $|2s\rangle$ orbital mixes with two $|2p\rangle$ orbitals which causes the formation of σ bonds between carbon atoms. In addition to σ bonds, unhybridized 2p orbitals from neighboring carbon atoms which are perpendicular to the plane of structure form π bonds. Because of the existence of both single ($\sigma : 1.47\text{Å}$) and double ($\pi : 1.35\text{Å}$) bonds, the nearest distance between two carbon atoms is 1.42 Å. In graphene, sp^2 hybridization causes the orientation of carbon atom orbitals in the xy plane and creates 120° angles in the plane as shown in Fig. 3.1 (a). In another word, sp^2 hybridization causes carbon atoms to assemble honeycomb lattices. However, the honeycomb lattice of graphene is not a Bravais lattice since it is made of two sublattices A and B. Therefore, its Bravais lattice can be viewed as a two-atom (A and B) basis hexagonal lattice. In the real space, three nearest neighbor vectors which connect sublattice A to sublattice B are given by [77, 80]

$$\delta_1 = \frac{a}{2}(\frac{1}{\sqrt{3}}, 1), \qquad \delta_2 = \frac{a}{2}(\frac{1}{\sqrt{3}}, -1), \quad \text{and} \quad \delta_3 = -a(\frac{1}{\sqrt{3}}, 0) \tag{3.1}$$

where $a = 2.46$Å is the lattice constant and it is equal to $\sqrt{3}$ times the nearest distance between two carbon atoms (1.42 Å). Two lattice vectors can be written as the following

$$a_1 = \frac{a}{2}(\sqrt{3}, 1) \quad \text{and} \quad a_2 = \frac{a}{2}(\sqrt{3}, -1) \tag{3.2}$$

The reciprocal lattice vectors defined with respect to the hexagonal Bravais lattice are given by

$$b_1 = \frac{2\pi}{\sqrt{3}a}(1, \sqrt{3}) \quad \text{and} \quad b_2 = \frac{2\pi}{\sqrt{3}a}(1, -\sqrt{3}) \tag{3.3}$$

The first Brillouin zone of graphene has 6 corners which consist of distinguished points K and K′ called Dirac points. In the reciprocal space their position are given by

$$K = (\frac{2\pi}{\sqrt{3}a}, \frac{2\pi}{3a}) \quad \text{and} \quad K' = (\frac{2\pi}{\sqrt{3}a}, -\frac{2\pi}{3a}) \tag{3.4}$$

Dirac points play a significant role in the electronic properties of graphene.

3.1.2 Electronic Properties of Graphene

From the electrical point of view, graphene is known as a zero-gap semiconductor. In graphene low energy charge carriers are massless Dirac fermions. Moreover for the low energy cases, the energy dispersion of graphene is relativistic. In other words, the energy of an electron depends on its momentum linearly and the Dirac relativistic massless equation is used to describe the electron's behavior in low energy cases.

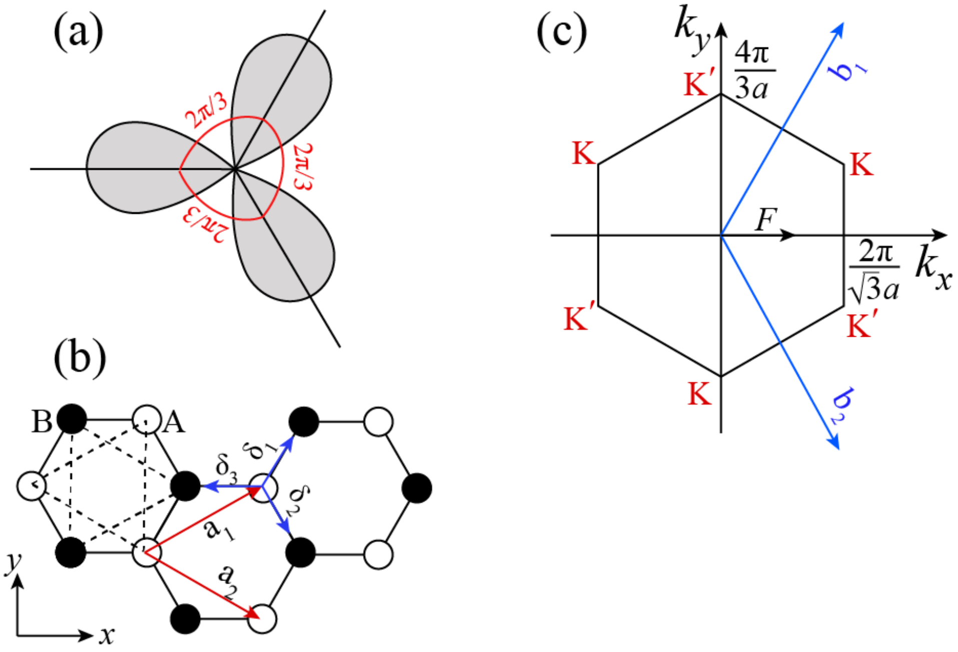

Figure (3.1) (Color online)(a)Schematic representation of the sp^2 hybridization. Local orbital of carbon atoms form angle of $\frac{2\pi}{3}$. (b) Honeycomb lattice of 2D graphene which is made of two triangular sublattices A and B. Carbon atoms shown by white circles belong to sublattice A and shown by black circles belong to sublattice B. a_1 and a_2 represent lattice vectors and the nearst neighbor vectors are shown by δ_1, δ_2, and δ_3. (c) The first Brillouin zone with inequivalent valleys K and K′. The recprocal lattice vectors are shown by b_1 and b_2.

Effective Low Energy Hamiltonian The low energy Hamiltonian known as the Dirac-like Hamiltonian in the vicinity of each Dirac points K or K′ is described by [81]

$$H_0 = \hbar v_f \begin{pmatrix} 0 & k_x + ik_y \\ k_x - ik_y & 0 \end{pmatrix} \tag{3.5}$$

Where $\hbar = \frac{h}{2\pi}$ is the reduced Planck's constant and the fermi velocity (v_f) is $10^6(m/s)$. This Hamiltonian is valid for 2D wave vectors as long as they satisfy the criteria $|\mathbf{k}| << 2\pi/a$ ($a = 2.46\mathring{A}$) in the vicinity of K and K' valleys in the Brillouin zone [81]. As mentioned earlier, the energy dispersion near the valley is linear given by

$$E_{c,v} = \pm\hbar v_f \sqrt{k_x^2 + k_y^2} = \pm\hbar v_f \left|\mathbf{k}\right| \tag{3.6}$$

and corresponding eigenvectors are given by

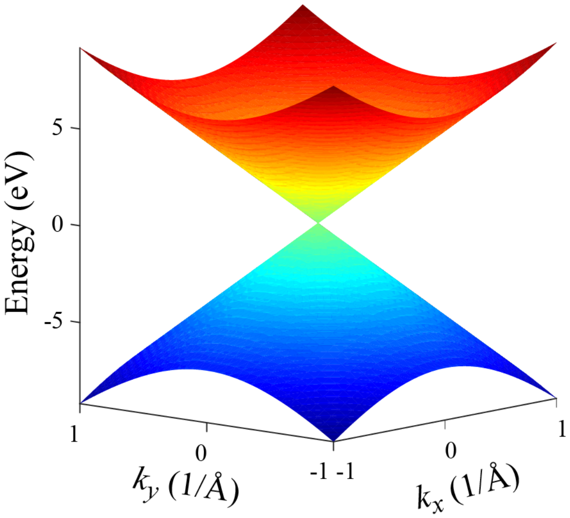

Figure (3.2) (Color online) Energy dispersion of graphene obtained from $\mathbf{k}\cdot\mathbf{p}$ theory near the valley K or K′ (k_x, k_y)=(0,0).

$$\Psi_{c,v} = \frac{e^{i\mathbf{kr}}}{\sqrt{2}} \begin{pmatrix} 1 \\ \pm e^{-i\phi_k} \end{pmatrix} \tag{3.7}$$

where $\mathbf{k} = (k_x, k_y) = |\mathbf{k}| e^{i\phi_k}$.

Tight Binding Hamiltonian Tight binding (TB) method is a semi-emprical method to be used to find the electronic band structure of the materials in the first Brillouin zone. The nearest neighbor TB Hamiltonian of graphene is a very simple Hamiltonian which takes into account only the hopping of an electron from sublattice A or B to the nearest neighbor located in sublattice B or A respectively.

$$H_0 = \begin{pmatrix} 0 & \gamma f(\mathbf{k}) \\ \gamma f^*(\mathbf{k}) & 0 \end{pmatrix} \tag{3.8}$$

where $\gamma = -3.03(eV)$ and $f(k) = \exp(i\frac{ak_x}{\sqrt{3}}) + 2\exp(-i\frac{ak_x}{2\sqrt{3}})\cos(\frac{ak_y}{2}) = |f(\mathbf{k})| e^{i\phi_{f(\mathbf{k})}}$. Corresponding energies for conduction band (π^* band) and valence band (π band)and corresponding eigenvectors are given as follows

$$E_{c,v} = \mp\gamma |f(\mathbf{k})| \tag{3.9}$$

and

$$\Psi_{\mathbf{k}}^{(\mathrm{c,v})}(\mathbf{r}) = \frac{e^{i\mathbf{kr}}}{\sqrt{2}} \begin{pmatrix} \mp 1 \\ e^{-i\phi_{f(\mathbf{k})}} \end{pmatrix} \tag{3.10}$$

3.2 Results and Discussion

We study electron dynamics in graphene in the presence of applied ultrafast and intense pulses with different electric field waveforms. The applied pulses have about $\sim 4-5$ fs duration and the electric field of the pulses have amplitudes $\sim 0.1 - 2$ V/Å We define various electric field waveforms, F, by using Hermit polynomials, H,

$$F^{(n)}(t) = (\frac{-1}{2}) f_0 e^{-u^2} H^{(n)}(u) \tag{3.11}$$

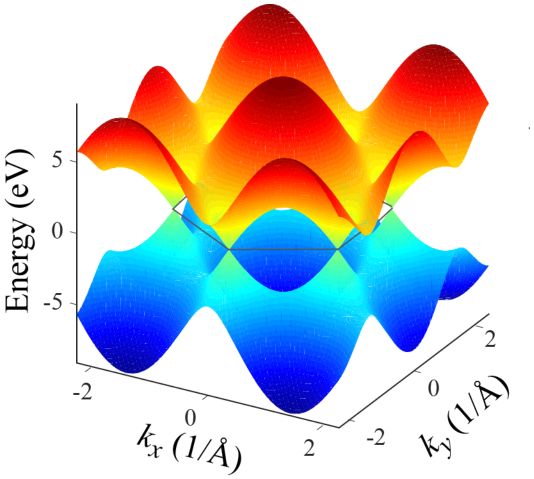

Figure (3.3) (Color online)Energy dispersion of graphene obtained within tight binding approximation.

where $u = t/\tau$, $\tau = 1$ fs, n represents the degree of the Hermit polynomials and f_0 is the amplitude of the applied field. In this study, we choose Hermit polynomials of degree of 2, 4, and 6 since these field profiles satisfy the following condition

$$\int_{-\infty}^{\infty} F^{(n)}(t)dt = 0, \qquad n = 2, 4, 6 \tag{3.12}$$

Therefore, applied fields have the following waveforms

$$F^{(2)}(t) = (\frac{-1}{2})f_0 e^{-u^2} H^{(2)}(u) = f_0(\frac{-1}{2})e^{-u^2}(4u^2 - 2) \tag{3.13}$$

$$F^{(4)}(t) = (\frac{1}{12})f_0 e^{-u^2} H^{(4)}(u) = f_0(\frac{1}{12})e^{-u^2}(16u^4 - 48u^2 + 12) \tag{3.14}$$

$$F^{(6)}(t) = (\frac{-1}{120})f_0 e^{-u^2} H^{(6)}(u) = f_0(\frac{-1}{120})e^{-u^2}(64u^6 - 480u^4 + 720u^2 - 120) \tag{3.15}$$

Vector potential, A, governs intraband electron dynamics defined by the integral of the applied field

$$A^{(n)}(t) = -\int_{-\infty}^{t} F^{(n)}(t')dt' \tag{3.16}$$

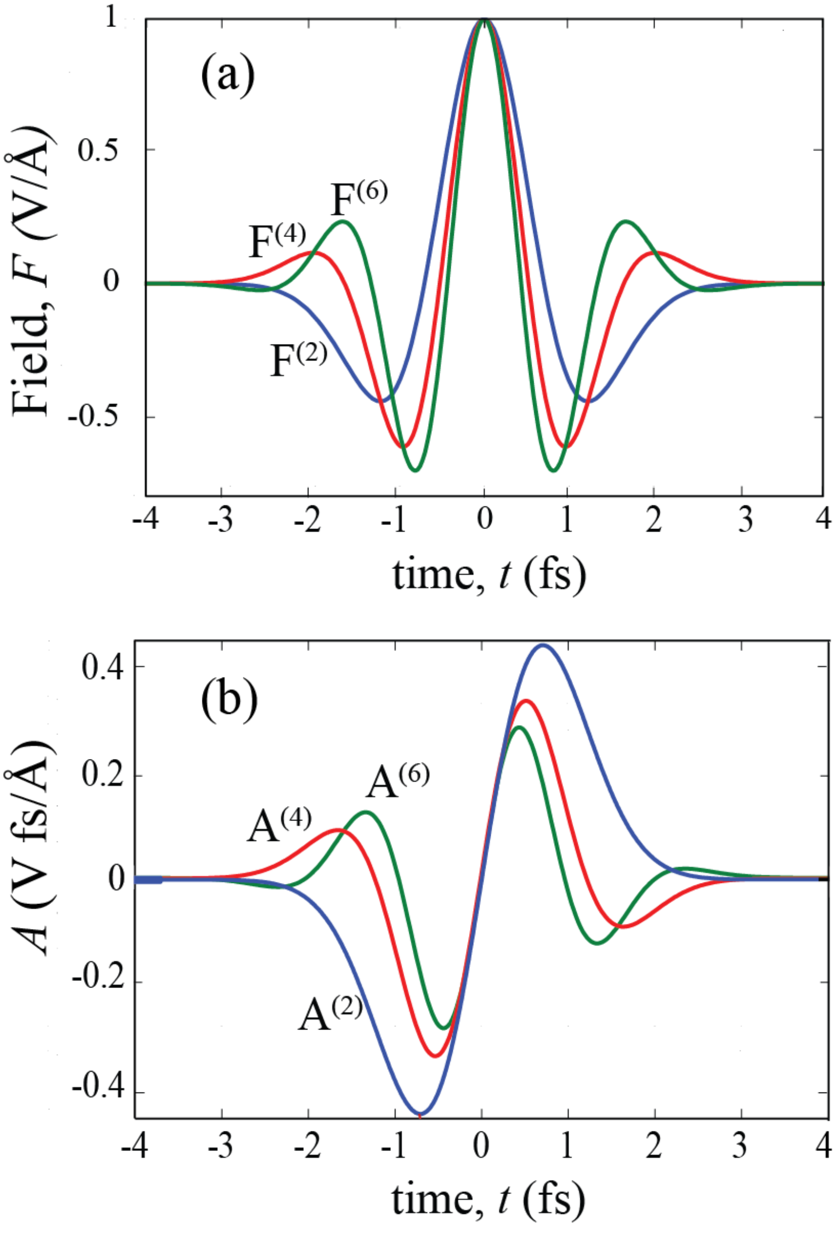

Figure (3.4) (Color online)(a) Electric field waveforms $F^{(2)}$ (blue), $F^{(4)}$ (red), and $F^{(6)}$ (green). (b) Corresponding vector potentials $A^{(2)}$ (blue), $A^{(4)}$ (red), and $A^{(6)}$ (green). The amplitude of the field, f_0, is 1 V/Å

For applied fields with various waveforms , $F^{(2)}$, $F^{(4)}$, and $F^{(6)}$, vector potentals $A^{(2)}$, $A^{(4)}$, and $A^{(6)}$, are associated with fields respectively as the following

$$\begin{aligned} A^{(2)}(t) &= \int_{-\infty}^{t} (\frac{-1}{2})e^{-u^2} H^{(2)}(u)dt_1 = f_0 t e^{-u^2} && (3.17)\\ A^{(4)}(t) &= \int_{-\infty}^{t} (\frac{1}{12})e^{-u^2} H^{(4)}(u)dt_1 = (\frac{-1}{3}) f_0 t(2u^2-3)e^{-u^2} && (3.18)\\ A^{(6)}(t) &= \int_{-\infty}^{t} (\frac{-1}{120})e^{-u^2} H^{(6)}(u)dt_1 = (\frac{1}{15}) f_0 t(4(u^2-5)u^2+15)e^{-u^2} && (3.19) \end{aligned}$$

In the presence of such ultrafast and intense pulses, we use analytical and numerical methods presented in chapter 2 to solve the time-dependent Schrodinger equation. The obtained results are presented in two sections. The first section includes the results considering the TB Hamiltonian of graphene for the first Brillouin zone. The results of low energy model of graphene are included in the second section.

Tight Binding Hamiltonian With the TB Hamiltonian given in Eq. 3.8 and corresponding valence and conduction bands' energies and eigenvectors (Eq. 3.9 and Eq. 3.10), valence and conduction bands' velocities and interband dipole matrix element are calculated using $\hat{V} = \frac{1}{\hbar}\frac{\partial H_0}{\partial k}$ and Eq. 2.12 from methodology chapter as the following expressions

$$V_x^{cc} = -V_x^{vv} = \frac{a\gamma}{\sqrt{3}\hbar}(\sin(\frac{akx}{\sqrt{3}} + \phi_k) + \sin(\frac{akx}{\sqrt{3}} + \phi_k)\cos(\frac{aky}{2})); \qquad (3.20)$$

$$V_x^{cv} = -i\frac{2a\gamma}{\hbar}\sin\left(\frac{akx}{\sqrt{3}} + \phi_k\right)\cos\left(\frac{aky}{2}\right); \qquad (3.21)$$

$$D_x = \frac{ea}{2\sqrt{3}}\frac{(1+\cos(\frac{aky}{2})(\cos(\frac{3ak_x}{2\sqrt{3}}) - 2\cos(\frac{ak_y}{2}))}{1+4\cos(\frac{ak_y}{2})(\cos(\frac{3ak_x}{2\sqrt{3}}) + \cos(\frac{ak_y}{2}))}. \qquad (3.22)$$

Fig. 3.5 represents the x-component of interband dipole matrix element for the first Brillouin zone. As shown in this figure, the interband dipole matrix has singularity at the corners of the Brillouin zone (K and K′ points). Ultrafast electron dynamics in graphene induced by ultrafast laser pulses are determined by two fundamental properties of graphene: 1)

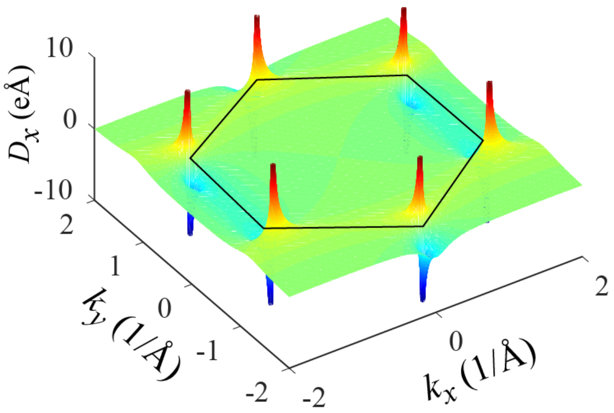

Figure (3.5) (Color online)x-component of interband dipole matrix. The first Brillouin zone of the reciprocal space is shown by solid black line.

having zero bandgaps at valleys, 2) singularity of interband dipole matrix at valleys. Due to these fundamental properties, electron dynamics in graphene is irreversible. The residual conduction band population is used to define the irreversibility of the system. The residual conduction band population is defined as a population which remains in the conduction band after the pulse ends. Fig. 3.6 shows the distribution of the residual conduction band population in reciprocal space after the applied linear pulse, $F^{(2)}$, ends. The distribution includes hot spots or interference fringes due to the interference of two passages per optical period of the same region of enhanced interband coupling. The distribution of the residual conduction band population after the applied linear pulse $F^{(4)}$ ends is shown in Fig. 3.7. In this distribution, the outmost fringes are due to the interference of two passages per optical period in the same region of enhanced interband coupling is similar to the distribution of the residual conduction band of $F^{(2)}$. However, the internal structure of this distribution is due to the interference of four passages per optical period in the same region of enhanced interband coupling. Therefore multiple crossings of the Dirac point creates connected fringes as an internal structure.

The residual distribution of Fig. 3.8 shows interference fringes which is similar to the residual distribution of Fig. 3.7 without any separate fringes. The electric field amplitude is 2 V/Å and it is the same for the residual distributions of Fig. 3.6, Fig. 3.7, and Fig.3.8.

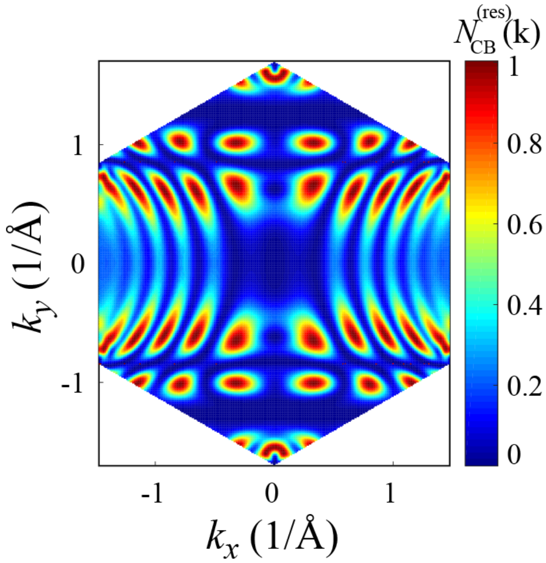

Figure (3.6) (Color online)Conduction band population $N_{\mathrm{CB}}(k,t) = |\beta_{ck}(t)|^2$ as a function of the wave vector for applied field $F^{(2)}$and amplitude of electric field 2 (V/Å). Only the first Brillouin zone of the reciprocal space is shown.

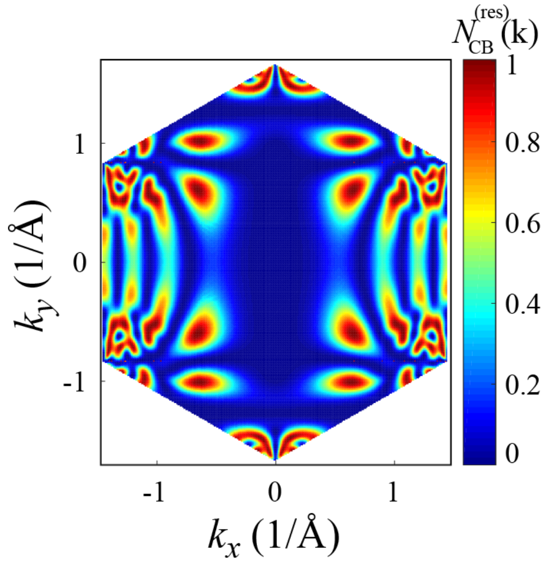

Figure (3.7) (Color online)Conduction band population $N_{\mathrm{CB}}(k,t) = |\beta_{ck}(t)|^2$ as a function of the wave vector for applied field $F^{(4)}$and amplitude of electric field 2 (V/Å). Only the first Brillouin zone of the reciprocal space is shown.

For the same amplitude of the applied field, the vector potential of $F^{(2)}$ is greater than the others. As a result, the electron trajectory is longer for an applied field $F^{(2)}$. That explains why there are residual distribution in broader area in the reciprocal space in comparison to the others. Nonzero residual conduction band populations determine the irreversibility of the graphene for the linearly applied pulses with different waveforms and the same amplitude of applied fields, 2 V/Å. Such irreversible electron dynamics occurs for all pulse amplitudes F0 with three different waveforms as Fig. 3.9 clearly demonstrates.

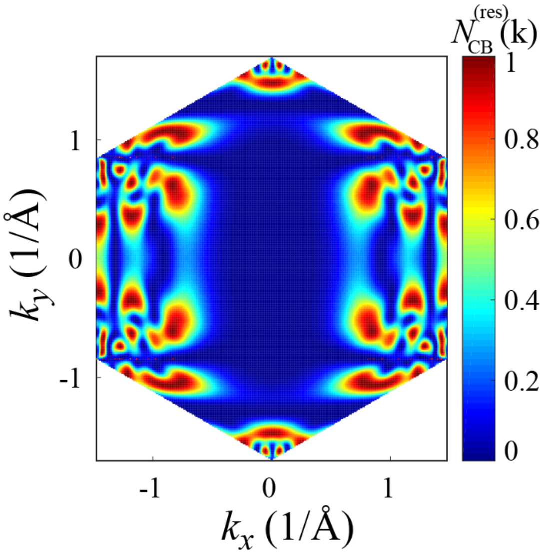

Figure (3.8) (Color online)Conduction band population $N_{\mathrm{CB}}(k,t) = |\beta_{ck}(t)|^2$ as a function of the wave vector for applied field $F^{(6)}$and amplitude of electric field 2 (V/Å). Only the first Brillouin zone of the reciprocal space is shown.

The asymmetric distributions of conduction and valence bands population during the pulses create electric charge currents, $\mathbf{J}$(t). In Fig. 3.10, Fig. 3.11, and Fig. 3.12, the current densities, $\mathbf{J}$(t), are shown as functions of time together with each corresponding vector potential, $\mathrm{A}^{(2)}$, $\mathrm{A}^{(4)}$, and $\mathrm{A}^{(6)}$ respectively. For all three waveforms of applied pulse, current densities follow the profiles of the vector potentials.

Fig. 3.13 shows currents for applied pulses with different waveforms. While theses currents have almost same maxima the area under the current curves, called transferred charge, are different.

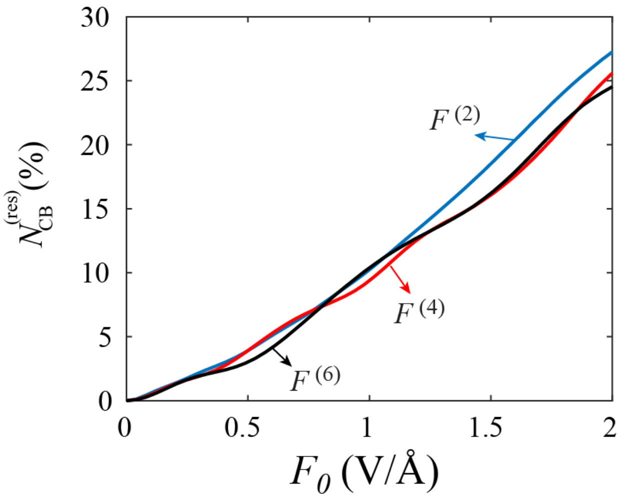

Figure (3.9) (Color online) Residual conduction band population as a funtion of field amplitude for $F^{(2)}$ (blue), $F^{(4)}$ (red), and $F^{(6)}$ (black).

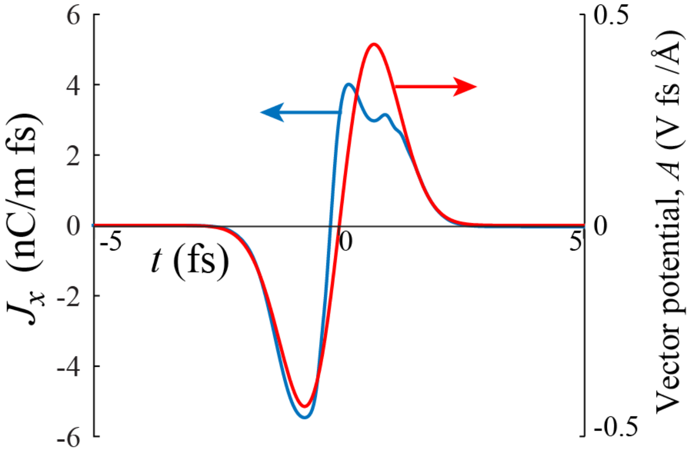

Figure (3.10) Electric current density in graphene as a function of time for amplitude $F_0 = 2.0$ (V/Å) (blue solid line) and the vector potential associated by the applied field, $F^{(2)}$, is shown by red solid line.

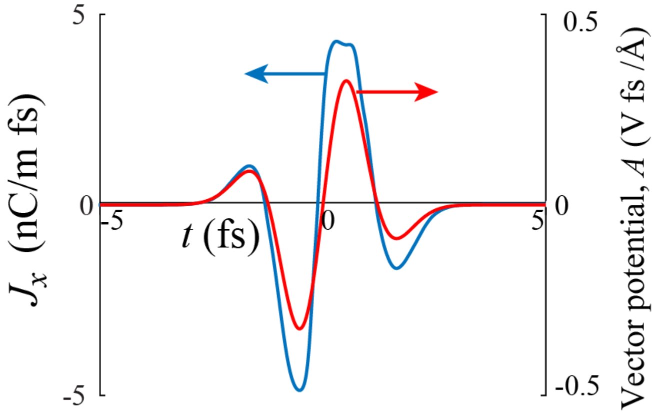

Figure (3.11) Electric current density in graphene as a function of time for amplitude $F_0 = 2.0$ (V/Å) (blue solid line) and the vector potential associated by the applied field, $F^{(4)}$, is shown by red solid line.

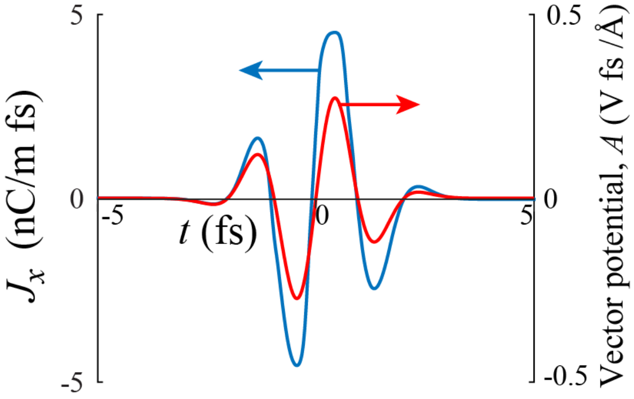

Figure (3.12) Electric current density in graphene as a function of time for amplitude $F_0 = 2.0$ (V/Å) (blue solid line) and the vector potential associated by the applied field, $F^{(6)}$, is shown by red solid line.

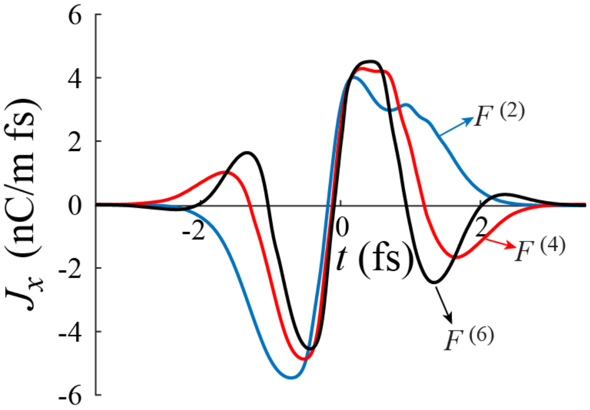

Figure (3.13) Electric current density in graphene as a function of time for amplitude $F_0 = 2.0$ (V/Å) where blue solid line is the waveform of the current for applied field $F^{(2)}$, red solid line is the waveform of the current for applied field $F^{(4)}$, and black solid line is the waveform of the current for applied field $F^{(2)}$.

The generated electric current results in finite charge transfer, Q_{tr}, which is defined by Eq. 2.20. Besides nonzero residual conduction band population, the transferred charge

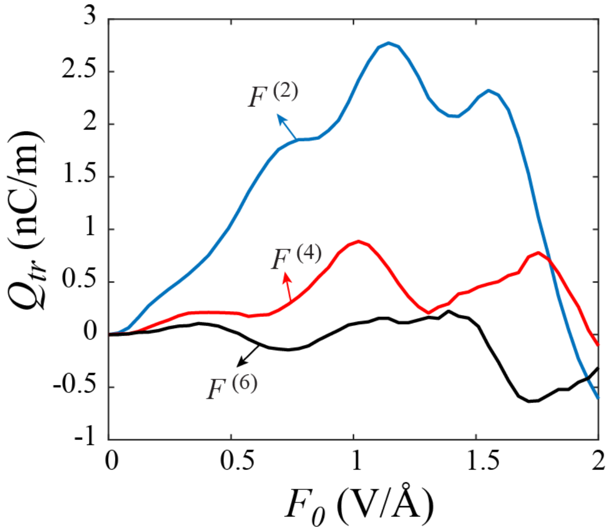

Figure (3.14) (Color online) Transferred charge as a function of field amplitude for $F^{(2)}$ (blue), $F^{(4)}$ (red), and $F^{(6)}$ (black)

can be considered as the other effect of irreversibility or the time asymmetry of the electron dynamics in graphene. As shown in Fig. 3.14, transferred charge for an applied field $F^{(2)}$ is five times greater than the transferred charge due to other applied field waveforms. Therefore it can be concluded that increasing the frequency of the field decreases the magnitude of transferred charge. Positive or negative signs of Q_{tr} determine weather the transferred charge is in the direction of the maximum of the applied field or in the opposite direction respectively.

Low Energy approximation To better understanding the behavior of electron dynamics in the vicinity of Dirac points, K and K′, the low energy effective approximation is used. In the low energy approximation we consider the Hamiltonian of Eq. 3.5 to derive the interband dipole matrix element like the following expression

$$D_x = -\frac{1}{2}\frac{k_y}{k_x^2 + k_y^2} \tag{3.23}$$

Since we apply x-polarized pulse normal to the sample, we calculate only the x component

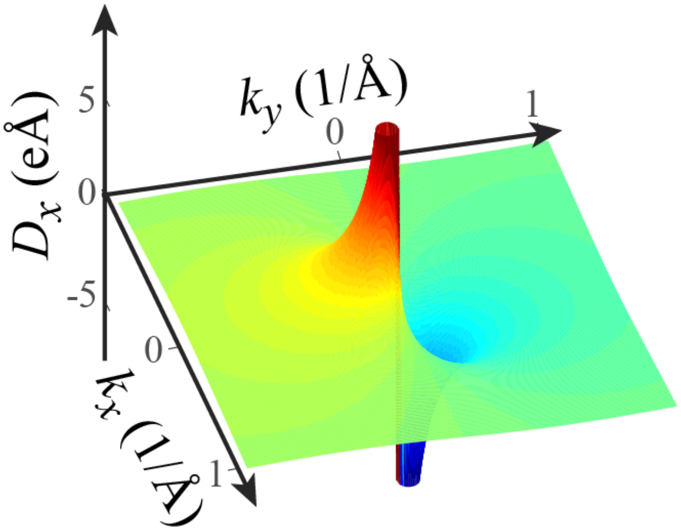

Figure (3.15) (Color online) X-component of the dipole matrix element in the low energy approximation at Dirac point.

of the interband dipole matrix element. With the wave functions represented in Eg. 3.7 for both conduction and valence bands, the velocity operator has the following matrix elements

$$V_{cc,x} = \hbar v_f \frac{k_x}{\sqrt{k_x^2 + k_y^2}}, \tag{3.24}$$

$$V_{vv,x} = -\hbar v_f \frac{k_x}{\sqrt{k_x^2 + k_y^2}}, \tag{3.25}$$

For the applied field $F^{(2)}$, the residual conduction band population is shown in Fig. 3.16. By increasing the amplitude of the applied field, more interference fringes with very high contrast: one and zero, the maximum and the minimum population probability, are created in the reciprocal space in the vicinity of the Dirac point. Due to the singularity of the interband dipole matrix, the distribution of the residual conduction band population is not uniform on the reciprocal space as shown in Fig. 3.16.

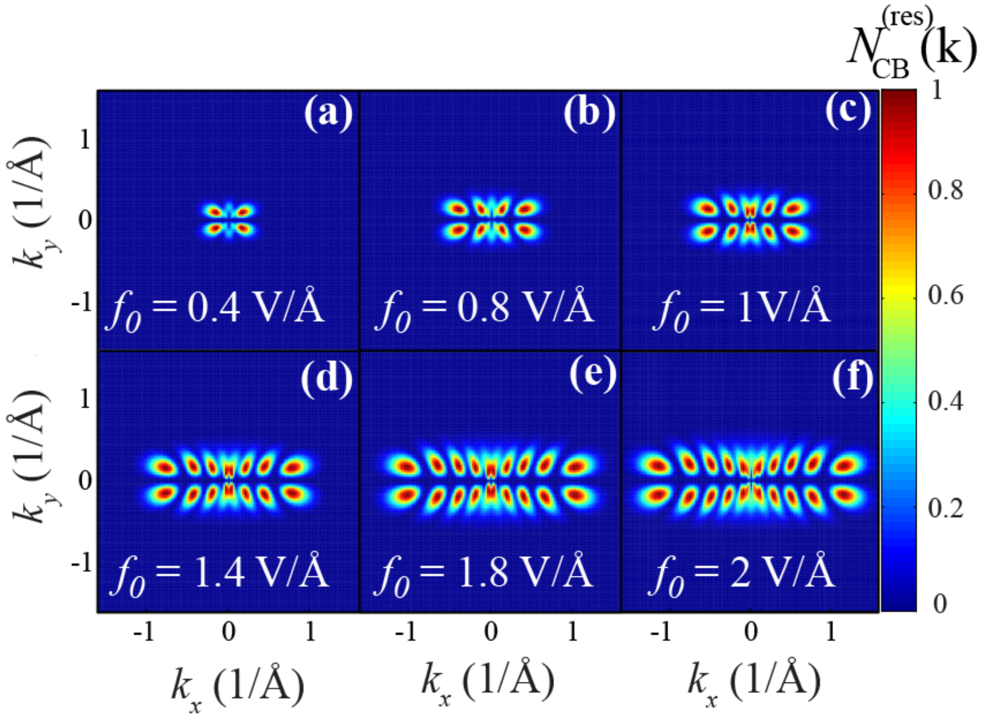

Figure (3.16) Distribution of residual conduction band population for applied field $F^{(2)}$ with different amplitudes 0.4-2 V/Å. The applied pulse is linearly polarized in x direction. The Dirac point is located in $(k_x, k_y) = (0, 0)$. Different colors correspond to different values of the residual conduction band population as shown in the figure.

Time evolution of the distribution of conduction band population for an applied field $F^{(2)}$ is represented in Fig. 3.17. From the initial time t_0 when the pulse is applied to t_1, due to the negative electric field electrons are accelerated to the left (we disregard the sign of electron charge). Therefore, electrons located on the right side of the Dirac point cross the

Dirac point for the first time. Due to the singularity of the interband dipole matrix at Dirac point, the large population of electrons is excited from the valence band to the conduction band. The length of the populated zone for this time interval is proportional to the amplitude vector potential of the applied field ($e/\hbar A$). From t_1 to t_2, the amplitude of the applied field is positive so the electrons are accelerated to the right and the electrons located on the right side of the Dirac point cross the Dirac point for the second time with different accumulated phases causing the creation of the interference fringes of the reciprocal space. In the time intervals, [t_2-t_3] and [t_3-t_4] the same process occurs for the electrons located on the left side of the Dirac point. After the pulse ends, the distribution of the residual conduction band population has high contrast peaks called interference fringes.

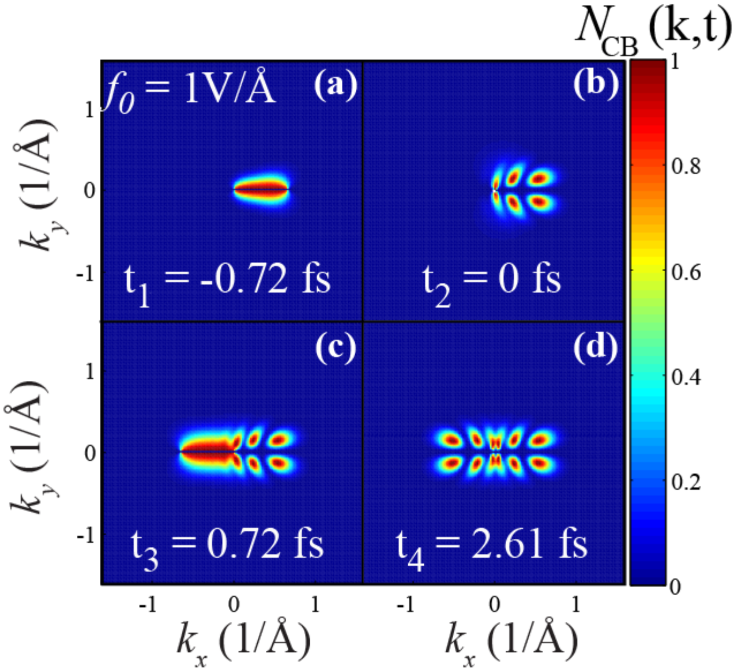

Figure (3.17) Distribution of conduction band population at different moment of times for applied field $F^{(2)}$. (a) $t_1 = -0.72$ fs this time is the time of the minimum value of vector potential corresponding to the applied field. (b) $t_2 = 0$ fs this time is the time of 0 value of vector potential corresponding to the applied field. (c) $t_3 = 0.72$ fs this time is the time of the minimum value of vector potential corresponding to the applied field. (d) $t_4 = 2.61$ fs this time is the final time after the applied field ends. The amplitude of the applied field is 1 V/Å. The Dirac point is located in $(k_x, k_y) = (0, 0)$. Different colors correspond to different values of the conduction band population as shown in the figure.

The distribution of the residual conduction band population for an applied field $F^{(4)}$ is shown in Fig. 3.18 for different field amplitudes. By increasing the amplitude of the applied field, the distribution of the residual conduction band population is increasing too. For this applied waveform, there are interference fringes similar to the distribution for the waveform $F^{(2)}$; unlike the distribution for the waveform $F^{(2)}$, there are internal structures created by electrons which pass the Dirac point multiple times.

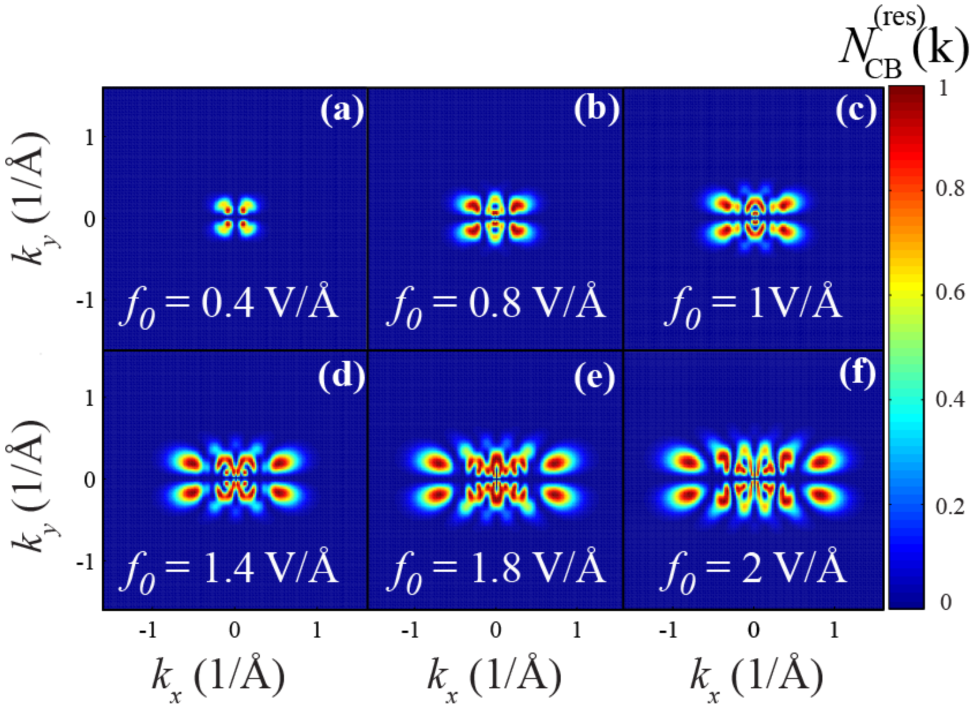

Figure (3.18) Distribution of residual conduction band population for applied field $F^{(4)}$ with different amplitudes 0.4-2 V/Å. The applied pulse is linearly polarized in x direction. The Dirac point is located in $(k_x, k_y) = (0, 0)$.Different colors correspond to different values of the residual conduction band population as shown in the figure.

Time evolution of conduction band population (Fig. 3.19) in the presence of field $F^{(4)}$ shows how the interference fringes of the residual conduction band population are created. In time interval $[t_0, t_1]$ the applied field is positive and the corresponding vector potential is short, so the small region on the left side of the Dirac point is populated. In time interval $[t_1, t_2]$, the electric field is negative, and the corresponding vector potential is large, so it creates small fringes on the left side of the Dirac point and creates a relatively large populated area on the right side of the Dirac point. In time interval $[t_2, t_3]$, the electric field is positive, and the corresponding vector potential is large, so it creates interference fringes on the right side of the Dirac point. In time interval $[t_3, t_4]$, the electric field is positive, and the corresponding vector potential is large, so it creates internal structure on the left side of the Dirac point since the electrons located in a small area on the left cross the Dirac point for the third time. $[t_4, t_5]$, the electric field is negative, and the corresponding vector potential is large; so it creates fringes on the left side and completes the internal structure on the left side of the Dirac point since the electrons located in the small area on the left cross the Dirac point for the fourth time and electrons located in the small area on the right of the Dirac point crosses the Dirac point for the third time and create internal structure on the right of the Dirac point as well. $[t_5, t_6]$, the electric field is positive, and the corresponding vector potential is small, so it completes the internal structure on the right side of the Dirac point since the electrons located in a small area on the right cross the Dirac point for the fourth time.

The residual conduction band population for the applied field $F_{(0)}$ with different amplitude is shown in Fig. 3.20. As the amplitude of the applied field increases so does the corresponding vector potential. Therefore a larger area of the reciprocal space near the Dirac point includes interference fringes.

Fig. 3.21 represents the time evolution of the conduction band for the applied field $F^{(6)}$ with the amplitude of 1 V/Å. As shown in this figure, due to the fact that electron trajectory crosses the Dirac point multiple times some connected interference fringes are created unlike the distribution for $F^{(2)}$ which includes separate interference fringes.

3.3 Conclusion

Electron dynamics in graphene is highly irreversible and strongly depends on the waveform of the applied pulse. This irreversibility is due to the gapless electrical structure of graphene and the singularity of the interband dipole matrix element at Dirac points. The ultrashort optical pulse causes the charge transfer through the system. The direction of

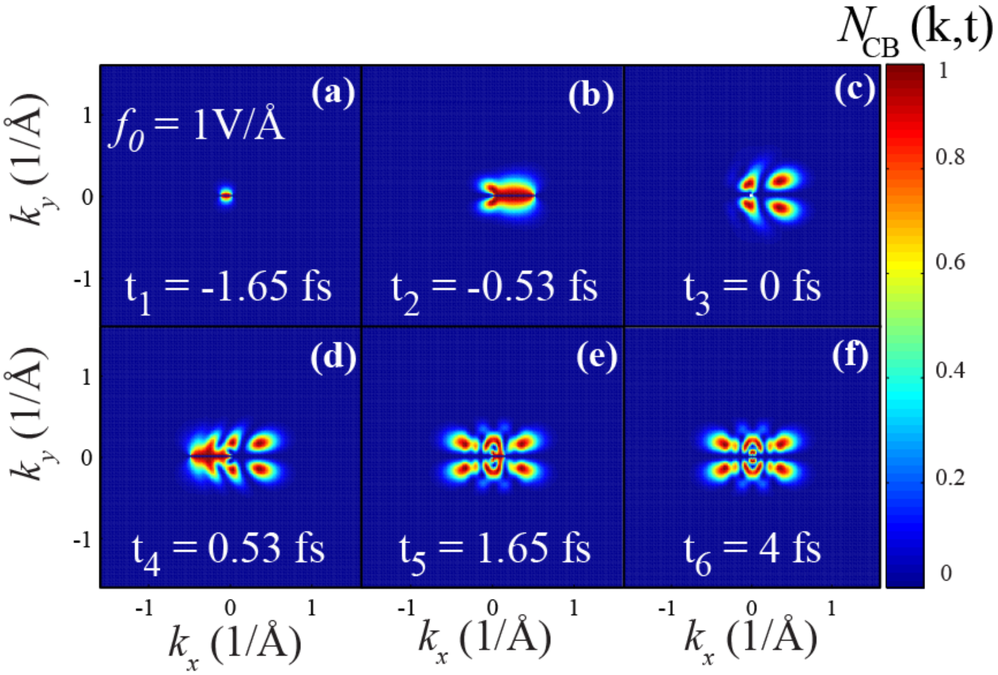

Figure (3.19) Distribution of conduction band population at different moment of times for applied field $F^{(4)}$. (a) $t_1 = -1.65$ fs this time is the time of the first local maximum value of vector potential corresponding to the applied field. (b) $t_2 = -0.53$ fs this time is the time of the minimum value of vector potential corresponding to the applied field. (c) $t_3 = 0$ fs this time is the time of 0 value of vector potential corresponding to the applied field. (d) $t_4 = 0.53$ fs this time is the time of the maximum value of vector potential corresponding to the applied field. (e) $t_5 = 1.65$ fs this time is the time of the last local minimum value of vector potential corresponding to the applied field. (f) $t_6 = 4$ fs this time is the final time after the applied field ends.The amplitude of the applied field is 1 V/Å. The Dirac point is located in $(k_x, k_y) = (0, 0)$.Different colors correspond to different values of the conduction band population as shown in the figure.

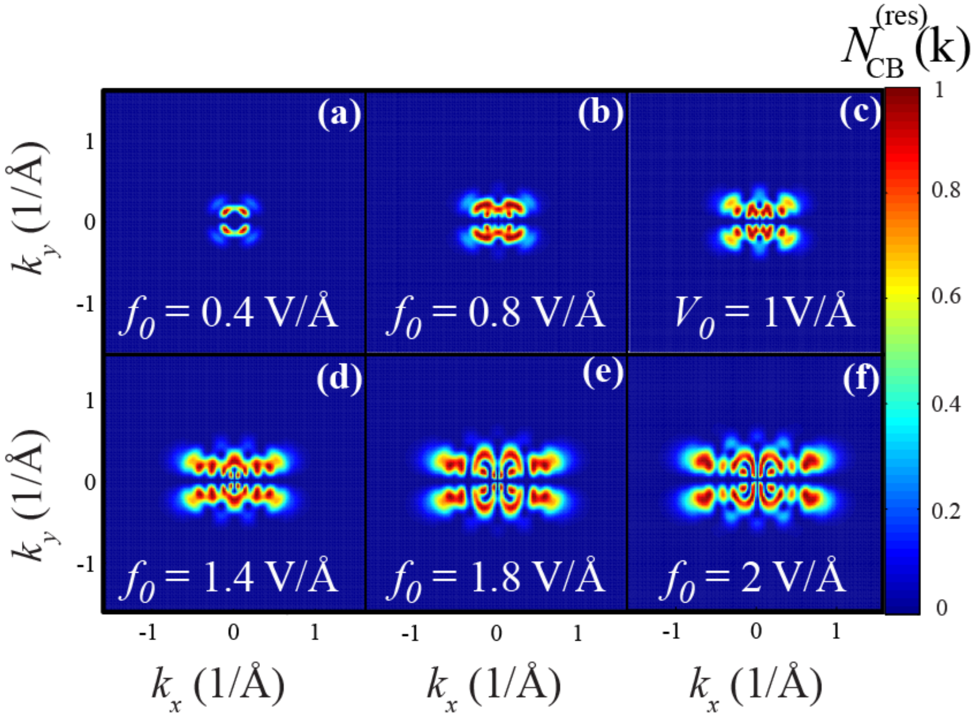

Figure (3.20) Distribution of residual conduction band population for applied field $F^{(6)}$ with different amplitudes 0.4-2 V/Å. The applied pulse is linearly polarized in x direction. The Dirac point is located in $(k_x, k_y) = (0, 0)$. Different colors correspond to different values of the residual conduction band population as shown in the figure.

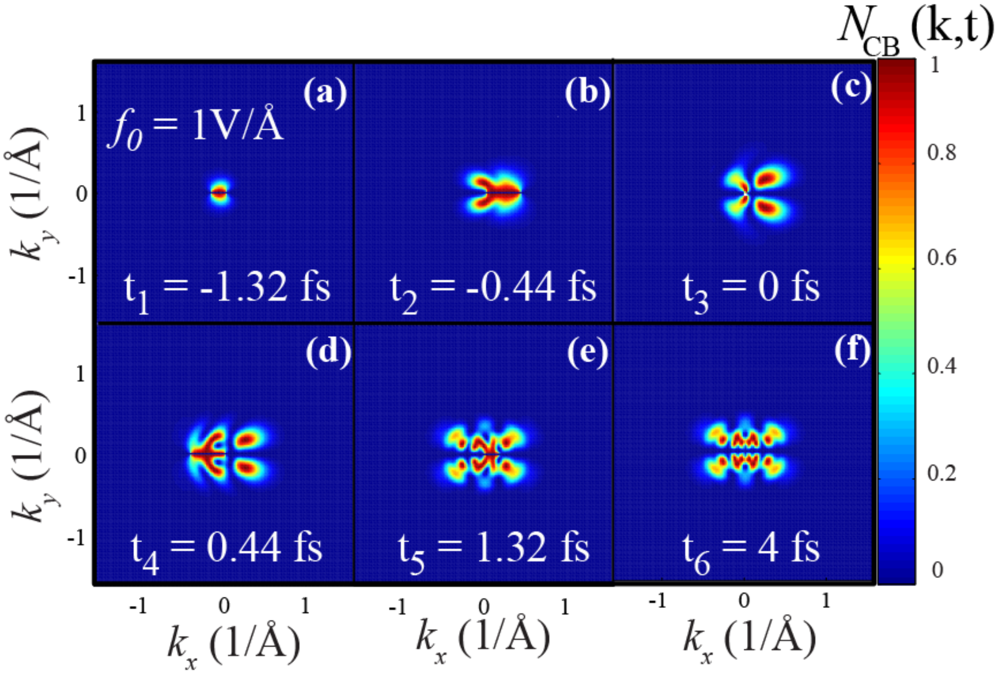

Figure (3.21) Distribution of conduction band population at different moments of time for an applied field $F^{(6)}$. (a) $t_1 = -1.32$ fs this time is the time of the first local maximum value of vector potential corresponding to the applied field. (b) $t_2 = -0.44$ fs this time is the time of the minimum value of vector potential corresponding to the applied field. (c) $t_3 = 0$ fs this time is the time of 0 value of vector potential corresponding to the applied field. (d) $t_4 = 0.44$ fs this time is the time of the maximum value of vector potential corresponding to the applied field. (e) $t_5 = 1.32$ fs this time is the time of the last local minimum value of vector potential corresponding to the applied field. (f) $t_6 = 4$ fs this time is the final time after the applied field ends.The amplitude of the applied field is 1 V/Å. The Dirac point is located in $(k_x, k_y) = (0, 0)$. Different colors correspond to different values of the conduction band population as shown in the figure.

transferred charge can be in the direction of field maximum or the opposite direction depending on the waveform and the amplitude of the applied pulse.

CHAPTER 4

TOPOLOGICAL INSULATOR

4.1 Introduction

In condensed matter physics, different quantum phases of matter are classified based on broken symmetry [82, 83, 84]. For example, liquid crystals have a broken translational symmetry. Magnets have a broken rotational symmetry and superconductors have a broken gauge symmetry. Broken symmetry is used as a unique order parameter to describe the quantum phases of matters universally [82, 83, 84]. The new quantum state of matter called the Quantum Hall state [85] does not fit into the matter classification based on the symmetry-breaking order parameters [83, 84].Therefore topological invariance was introduced as a new way of classifing quantum states . In mathematics 2D surfaces are topologically equivalent if they have the same number of holes since one can be converted to others without creating any hole [83]. In physics, two gapped states are topologically equal if one state can be obtained from the other by the smooth change of its Hamiltonian without closing the gap. In the new classification based on the topology, topological order parameters defined as invariant integrals over the reciprocal space play the role of symmetry-breaking order parameters in the conventional classification [83].

The first experimentally known topological phase of matter is a quantum Hall state which is not invariant under time reversal because of the presence of a magnetic field [86]. However, time reversal symmetry is not broken for the new topological phase known as a topological insulator (TI) [83, 83].

TIs act like ordinary insulators in their bulk and like conductors at their edges or surfaces depending on their dimensionality, 3 or 2 respectively [83, 83]. The time reversal symmetry protects these conducting edge states or surface states. In conducting states, the directions of the spin of an electron and its momentum are locked as shown in Fig. 4.1.

This is a result of the strong spin-orbit coupling (SOC) in these materials. Due to the spin-momentum locking, the back scattering or U turn is forbidden in TIs in the absence of magnetic impurities. There are many studies which predict topologically insulator materials which lead to the first generation of TIs including Bi/Sb and then to the second generation materials including Bi_2Se_3, Bi_2Te_3, Sb_2Te_3, and their alloys [87, 88].

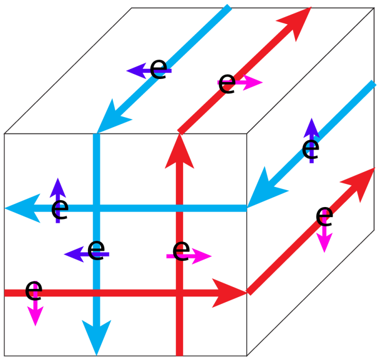

Figure (4.1) Schematic view of spin-momentum locking on the surfaces of a 3d topological insulator. Long arrows show directions of the momentum and short arrows represent the direction of the electron spin.

4.1.1 Crystal Structure of Bi_2Se_3

The rhombohedral crystalline structure of Bi_2Se_3 with five atoms per unit cell is shown in Fig. 4.2 [1, 89, 90]. Its crystal structure is made of five atomic layers, called a quintuple layer, and it has threefold symmetry along the z-axis, twofold symmetry along the x-axis, inversion symmetry, and time reversal symmetry [1, 91, 92, 93]. The electron configuration of Bi and Se are $6s^2 6p^3$ and $4s^2 4p^4$ respectively [91]. Therefore, the p orbitals, the outmost shells, of Bi and Se are used to drive the model Hamiltonian of this TI [91, 1].

4.1.2 Low Energy Effective Hamiltonian

We start with the effective low energy model Hamiltonian of surface states of the 3D topological insulator near the Γ point, the only Dirac point of the surface states [94]

$$H_0 = A_1 + A_2 k_{||}^2 + A_3(\sigma_x k_y - \sigma_y k_x) + A_4(k_+^3 + k_-^3)\sigma_z \tag{4.1}$$

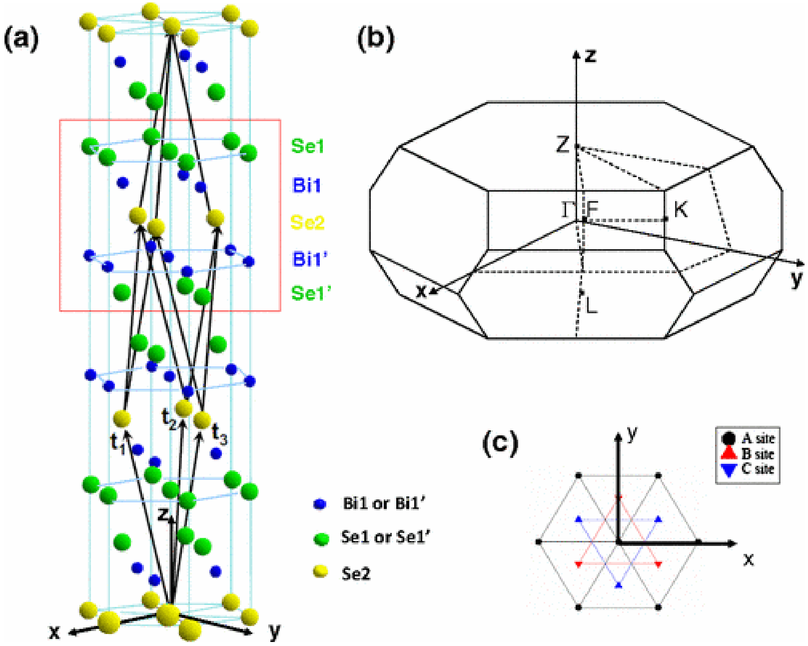

Figure (4.2) (Color online) (a) Rhombohedral crystal structure of Bi_2Se_3. t_1, t_2, and t_3 are lattice vectors.(b) The first Brillouin zone of Bi_2Se_3. (c) Top view of the triangle lattice with three possible positions A, B, and C. [1]

where σ_x, σ_y, and σ_z are Pauli matrices, $k_\pm = k_x \pm ik_y = k_{||}e^{\pm i\theta}$, and A_1, A_2, A_3, and A_4 are constants and equal to $0.034(eV)$, $23.725(eV.\mathring{A}^2)$, $3.297(eV.\mathring{A})$, and $25.045(eV.\mathring{A}^3)$ respectively. The cubic term in the low energy Hamiltonian is called a hexagonal warping term [95]. The valence and the conduction band energies are expresses as following

$$E_{c,v} = A_1 + A_2(k_x^2 + k_y^2) \pm \sqrt{A_3^2(k_x^2 + k_y^2) + 4A_4^2k_x^2(k_x^2 - 3k_y^2)^2} \tag{4.2}$$

where c and v stand for conduction and valence bands receptively. Fig. 4.3 represents the energy dispersion of the Bi_2se_3 surface state near Γ point (0,0). Here the Fermi energy is 0.034(eV).

Calculated x and y components of the dipole matrix element for the surface state of Bi_2Se_3 are the following expressions:

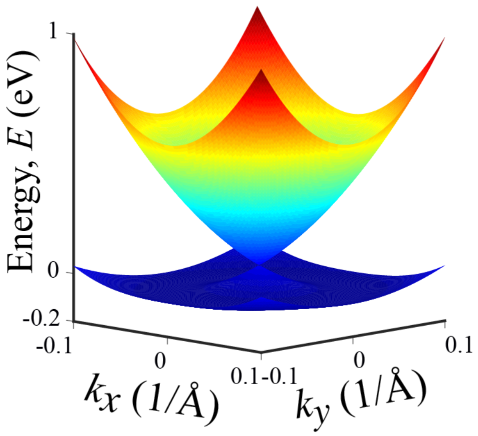

Figure (4.3) Low energy dispersion near Γ point located at (0,0).

$$D_x = N\left(-\frac{1}{2}\frac{k_y}{k_x^2+k_y^2} - i\frac{2k_x^4+3k_y^2(k_x^2-k_y^2)}{(k_x^2+k_y^2)\sqrt{(4k_x^2(k_x^2-3k_y^2)^2+(\frac{A_3}{A_4})^2(k_x^2+k_y^2))}}\right) = |D_x|\exp{(\phi_k)} \quad (4.3)$$

$$D_y = N\left(\frac{1}{2}\frac{k_x}{k_x^2+k_y^2} + i\frac{k_xk_y(7k_x^2+3k_y^2)}{(k_x^2+k_y^2)\sqrt{4k_x^2(k_x^2-3k_y^2)^2+(\frac{A_3}{A_4})^2(k_x^2+k_y^2))}}\right) = |D_y|\exp{(\phi_k)} \quad (4.4)$$

where $N = e\left(1+\frac{4k_x^2(k_x^2-3k_y^2)^2}{(\frac{A_3}{A_4})^2(k_x^2+k_y^2)}\right)^{-\frac{1}{2}}$. Similar to the interband dipole matrix of graphene, there are singularities at the Dirac points for both x and y components of interband dipole matrix of Bi_2Se_3. However, unlike graphene, both components of the interband dipole matrix of Bi_2Se_3 have imaginary parts which are due to the cubic term or warping term of the surface states Hamiltonian (Fig. 4.4).

Fig. 4.4 represents (a) the x-component and (b) the y-component of the interband dipole matrix as vectors where the lengths of the vectors correspond to the modules of D_x, and D_y and directions of vectors correspond to the phase of D_x and D_y respectively.

Considering the surface states Hamiltonian with warping terms causes the creation of branches in the distributions of the x and y components of the interband dipole matrix on the reciprocal space as shown in Fig. 4.4.

Intraband velocities of an electron in the x and y directions are calculated analytically

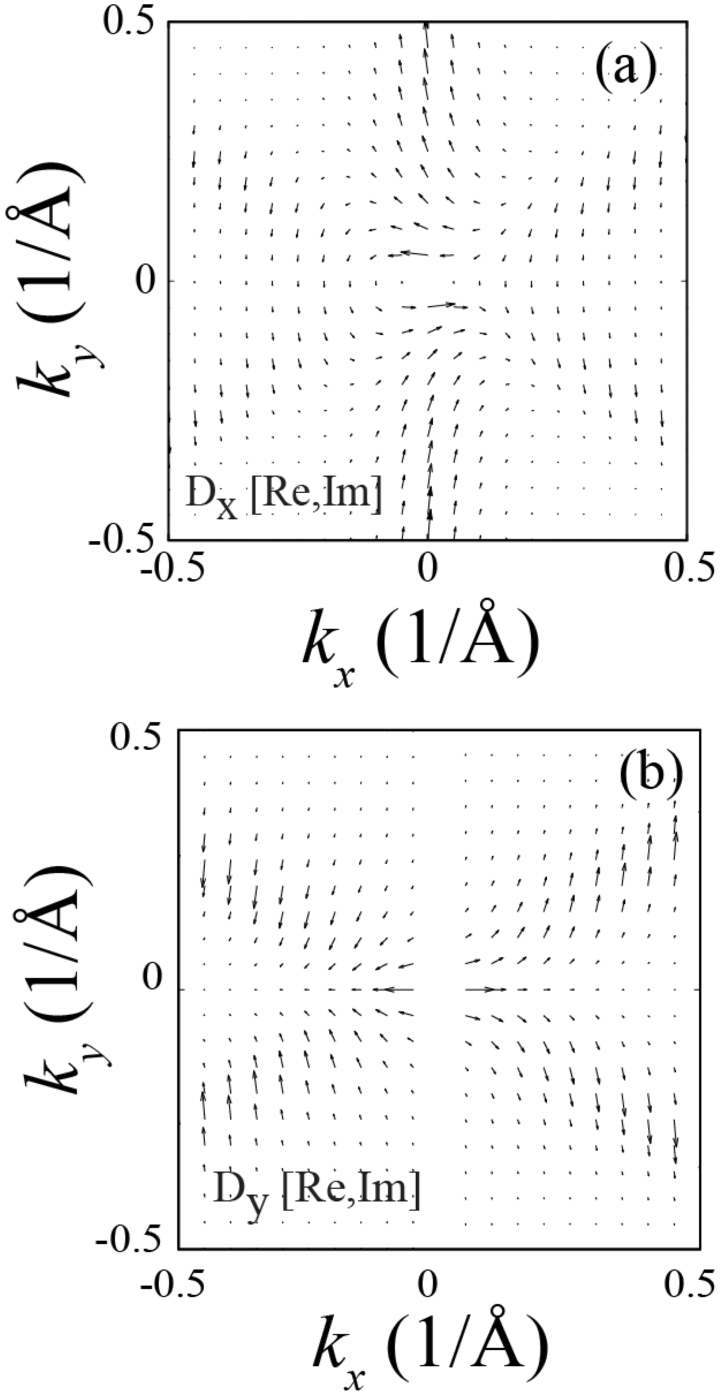

Figure (4.4) (a) x-component of interband dipole matrix is shown with vectors. The length of the vectors shows modules of D_x and the direction corresponds to the phase of D_x. (b) y-component of interband dipole matrix is shown with vectors. The length of the vectors shows modules of D_y and the direction corresponds to the phase of D_y.

as follows.

$$V_{c,x} = \frac{2k_x}{\hbar}(A_2 + \frac{\frac{1}{2}A_3^2 + 2A_4^2(k_x^2 - 3k_y^2)^2 + 4A_4^2k_x^2(k_x^2 - 3k_y^2)}{\sqrt{A_3^2(k_x^2 + k_y^2) + 4A_4^2k_x^2(k_x^2 - 3k_y^2)^2}}) \tag{4.5}$$

$$V_{v,x} = \frac{2k_x}{\hbar}(A_2 - \frac{\frac{1}{2}A_3^2 + 2A_4^2(k_x^2 - 3k_y^2)^2 + 4A_4^2k_x^2(k_x^2 - 3k_y^2)}{\sqrt{A_3^2(k_x^2 + k_y^2) + 4A_4^2k_x^2(k_x^2 - 3k_y^2)^2}}) \tag{4.6}$$

$$V_{c,y} = \frac{2k_y}{\hbar}(A_2 + \frac{\frac{1}{2}A_3^2 - 12A_4^2k_x^2(k_x^2 - 3k_y^2)}{\sqrt{A_3^2(k_x^2 + k_y^2) + 4A_4^2k_x^2(k_x^2 - 3k_y^2)^2}}) \tag{4.7}$$

$$V_{v,y} = \frac{2k_y}{\hbar}(A_2 - \frac{\frac{1}{2}A_3^2 - 12A_4^2k_x^2(k_x^2 - 3k_y^2)}{\sqrt{A_3^2(k_x^2 + k_y^2) + 4A_4^2k_x^2(k_x^2 - 3k_y^2)^2}}) \tag{4.8}$$

4.2 Results and discussion

4.2.1 Linear Polarized Pulse

We apply a linear polarized pulse normal to the surface of a 3D TI, Bi_2Se_3, where the electric field component of the applied pulse has the following waveform

$$\mathbf{F}(t) = f_0 e^{-u^2}(1 - 2u^2) \tag{4.9}$$

where $\mathbf{F}(t) = (F_x(t), F_y(t)) = (F(t)\cos(\theta), F(t)\sin(\theta))$ and θ is the polarization angle of the applied field.

For a linear x-polarized pulse with an amplitude of 0.10 V/Å, the distribution of the residual conduction band population in the reciprocal space is shown in Fig. 4.5. The distribution includes "hot spots" and less populated branches which correspond to the distribution of the modulus of the x component of the interband dipole matrix shown in Fig. 4.4 (a). Due to the singularity of the dipole matrix at the Dirac point (Γ point) there is no residual population at that point.

To investigate the possibility of having the anisotropic electron dynamics in the surface states of the TI, a y-polarized pulse is applied normal to the surface of the TI. As shown

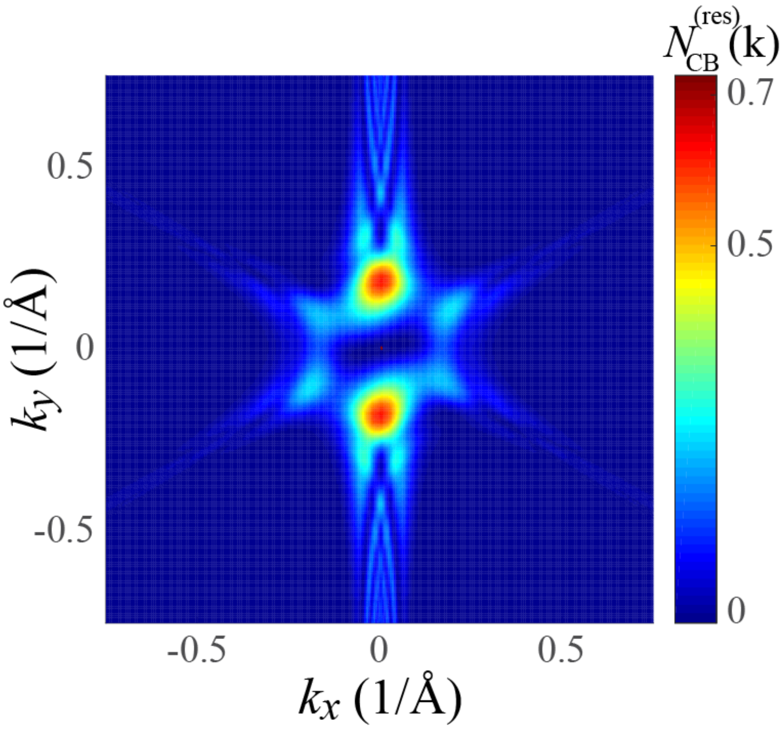

Figure (4.5) (Color online) Residual conduction band population for x -polarized pulse with the amplitude of electric field 0.10 V/Å.

in Fig. 4.6, the residual conduction band population corresponds to the distribution of the y-component of interband dipole matrix represented in Fig. 4.4 (b). The number of ”hot spots” and the distribution of the residual conduction band population are different from Fig. 4.5.

The distributions of the residual conduction band population for two linear pulses with $\pi/4$ and $\pi/3$ polarization are shown in Fig. 4.7, and Fig. 4.8 respectively. The distributions shown for different polarization of the applied field prove that the electron dynamics is anisotropic and irreversible in the surface states of Bi_2Se_3.

The total residual conduction band population near the Γ point for different linearly polarized fields are increased monotonically by increasing the amplitude of the applied fields as shown in Fig. 4.9. Moreover, according to these results for linearly polarized pulses, the applied pulse with y polarization causes a greater total conduction band population in comparison to other fields with different polarizations.

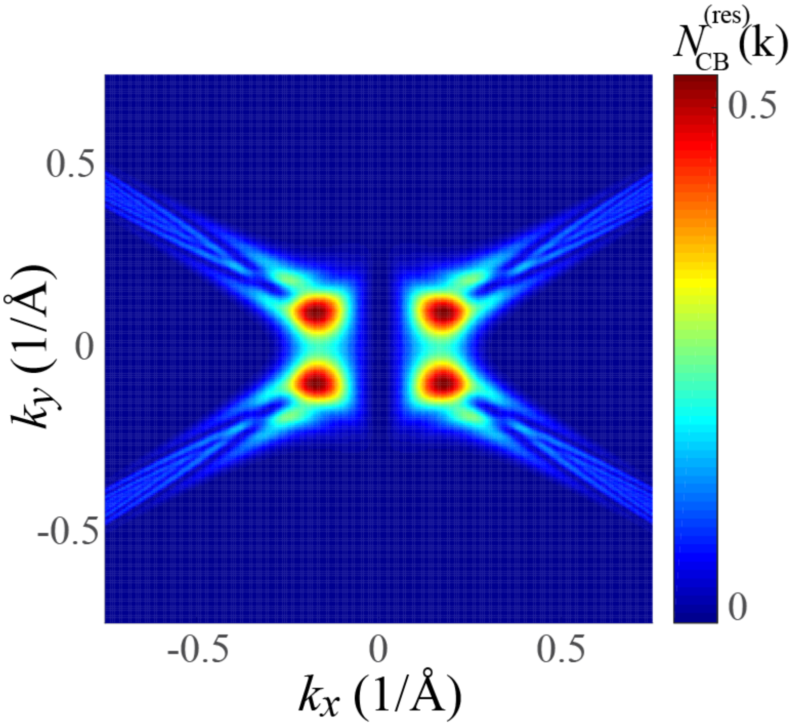

Figure (4.6) (Color online) (a) Residual conduction band population for y -polarized pulse with the amplitude of electric field 0.10 V/Å.

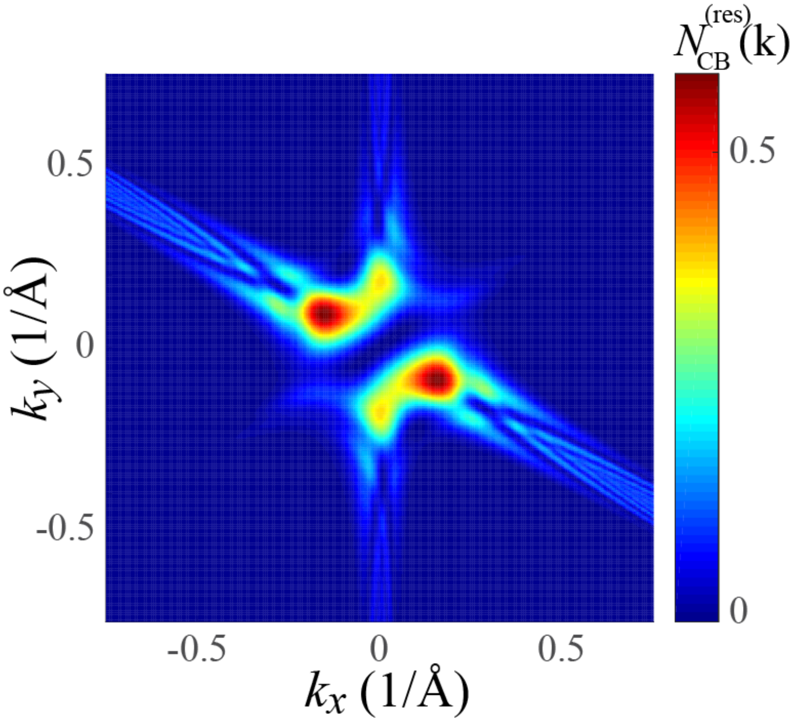

Figure (4.7) (Color online) Residual conduction band population for $\pi/4$ -polarized pulse with the amplitude of electric field 0.10 V/Å.

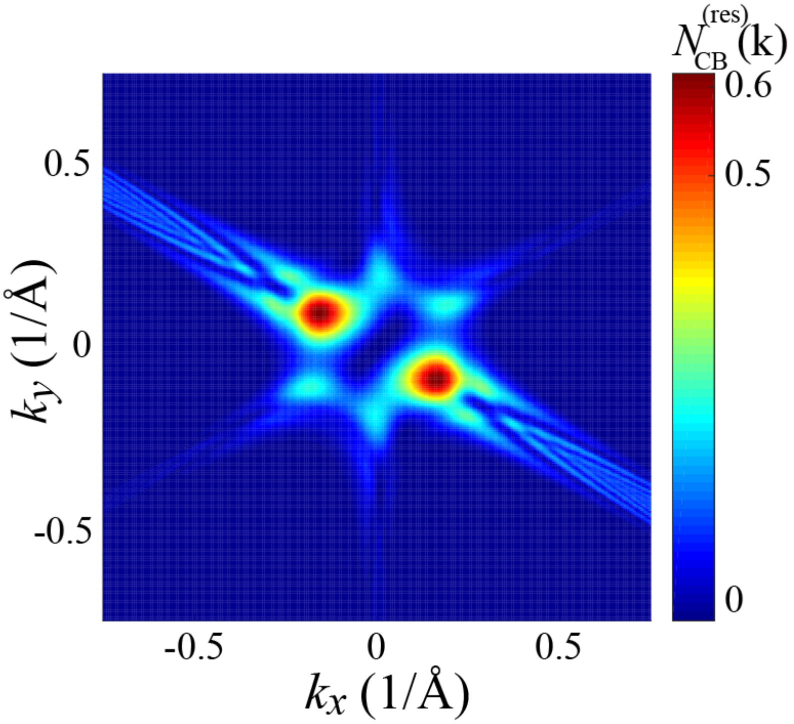

Figure (4.8) (Color online) Residual conduction band population for $\pi/3$ -polarized pulse with the amplitude of electric field 0.10 V/Å.

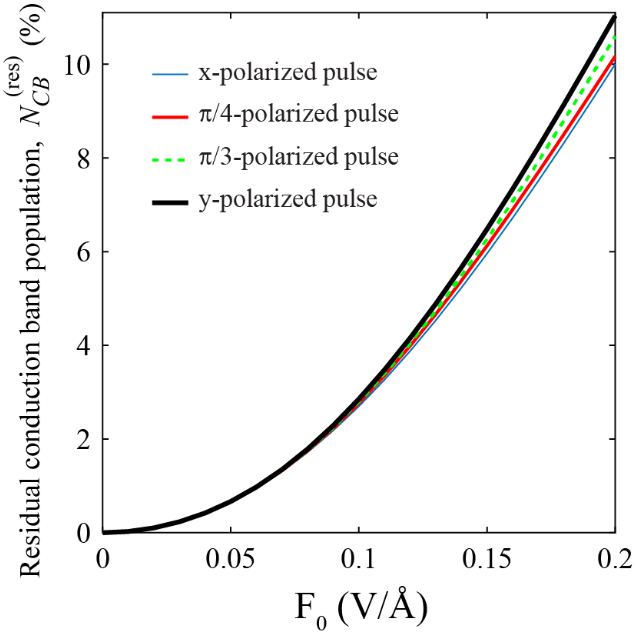

Figure (4.9) (Color online) Total residual conduction band population near Γ point in the reciprocal space as a function of field amplitude for different polarization x (blue solid line), $\pi/4$ (red solid line), $\pi/3$ (green dashed line), and y (black solid line).

During the pulse, the asymmetric distribution of the finite conduction band population generates the electric current. In Fig. 4.10, the electric charge current density is shown as a function of time for different field amplitudes of the x-polarized optical pulse.

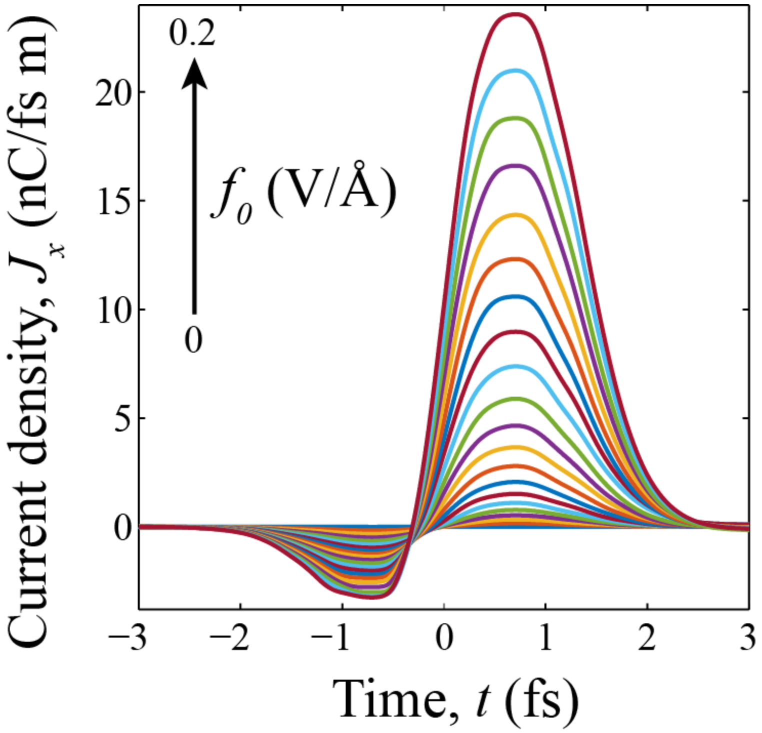

Figure (4.10) (Color online) Total current density, J_x, due to applied x-polarized pulse. The amplitude of the electric field is changed from 0 to 0.2 V/Å.

Total electric current density waveforms for different linearly polarized field in the direction of the applied pulses are shown in Fig. 4.11 where the amplitude of applied pulses is equal to 0.1 V/Å. As represented in this figure, a y-polarized pulse creates current density with the maximum of about 24 nC/fsm which is about 5 times larger than the maximum of the current density produced by a x-polarized pulse.

The transferred charge due to the applied ultrafast field is another factor used to determine the reversibility of the electron dynamics which can be calculated as the integral of the current density. Fig. 4.12 shows the monotonic dependence of the transferred charge in the x-direction for different polarizations on the amplitude of the applied field.

The calculated transferred charge in the y-direction shown in Fig. 4.13 also depends on

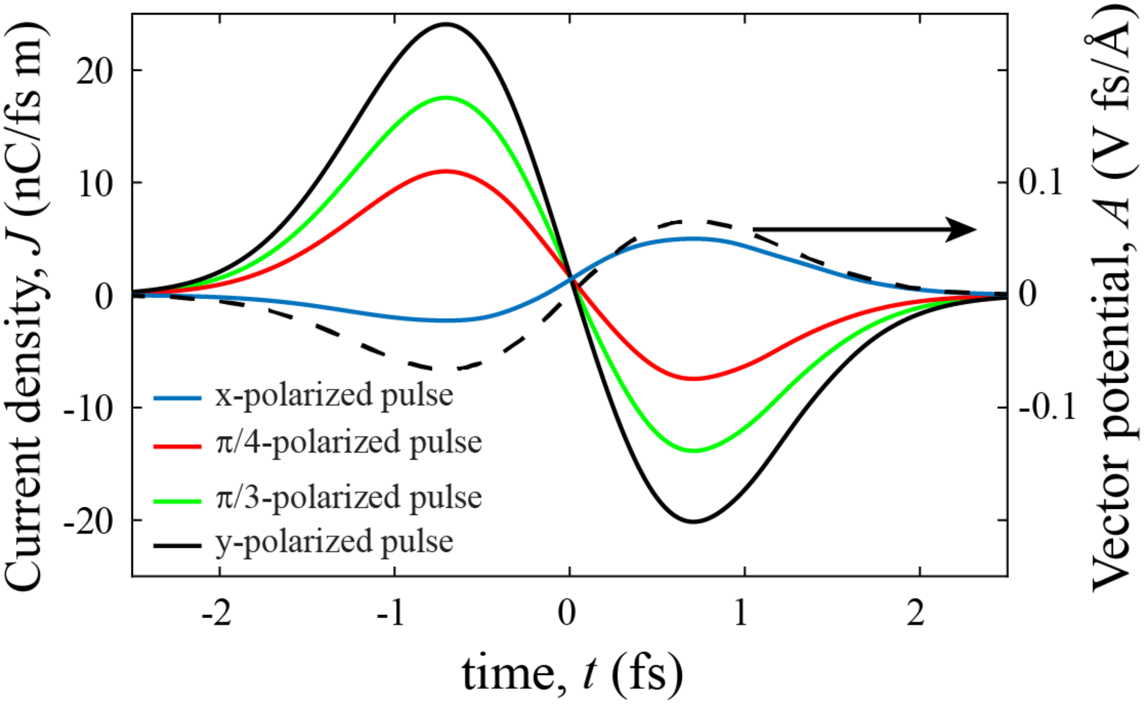

Figure (4.11) (Color online) Total current density, J, in the direction of applied linear polarized pulse, x (blue), $\pi/4$ (red), $\pi/3$ (green), and y (black).The black dashed line is the corresponding vector potential of the applied field. The amplitude of the electric field is 0.1 V/Å.

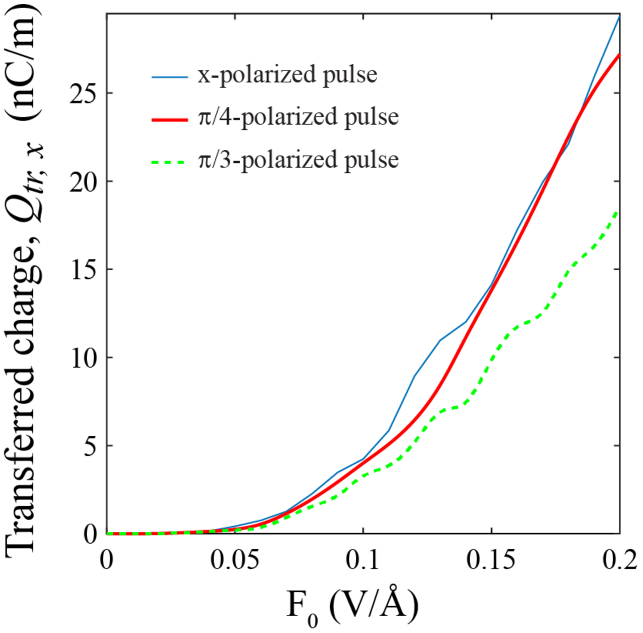

Figure (4.12) (Color online) Transferred charge in x direction as a function of field amplitude for different polarization x (blue solid line), $\pi/4$ (red solid line), and $\pi/3$ (green dashed line) the amplitude of the applied field monotonically. Since the current in y-direction has the highest amplitude, it causes the most transferred charges in comparison to the others for field amplitudes larger than 0.05 V/Å which is represented in Fig. 4.14. Where Q_{eff} stands for the effective transferred charge in the direction of the applied strong field.

Fig. 4.9 and Fig. 4.14show the total residual conduction band population and the effective transferred charge shown as functions of time for different polarization of the optical pulse, indicating that the electron dynamics is highly irreversible in the surface states of Bi_2Se_3 in the presence of linearly polarized pulses. Moreover, RCB population is highly anisotropic since its distribution strongly depends on the polarization of the applied field. The conduction band population distribution is characterized by hot spots, the number of which depends on the polarization of the pulse.

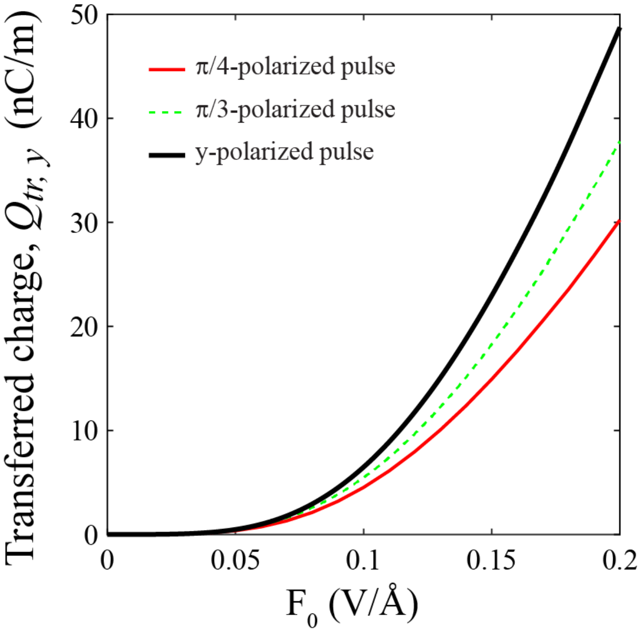

Figure (4.13) (Color online) Transferred charge in y direction as a function of field amplitude for different polarization $\pi/4$ (red solid line), $\pi/3$ (green dashed line), and y (black solid line).

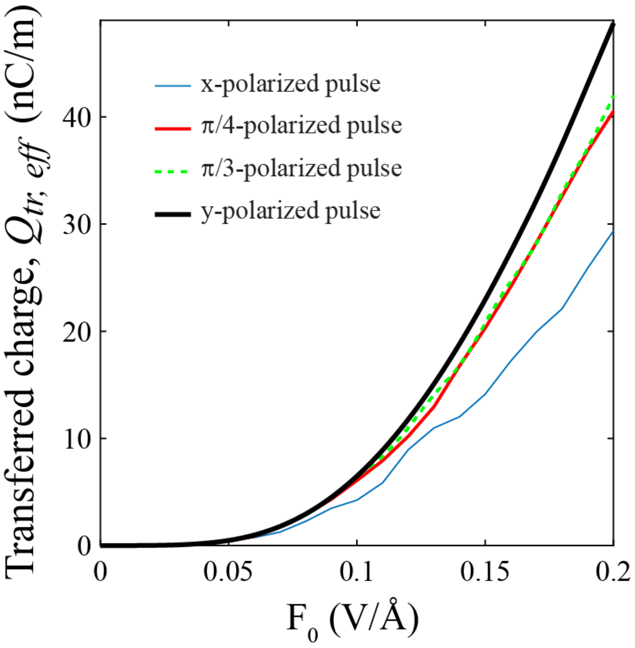

Figure (4.14) (Color online) Effective transferred charge in the direction of the applied field as a function of field amplitude for different polarization x (blue solid line), $\pi/4$ (red solid line), $\pi/3$(green dashed line), and y (black solid line).

4.2.2 Circular Polarized Pulse

We apply a circular pulse normal to the surfaces of a 3D TI, Bi_2Se_3, the electric field component of the applied pulse has the following waveform $\mathbf{F}(t) = (F_x(t), F_y(t))$

$$\begin{aligned} F_x(t) &= \pm f_0 e^{-u^2}(1-2u^2) \\ F_y(t) &= 2 f_0 u e^{-u^2} \end{aligned} \tag{4.10}$$

where, f_0 is the amplitude of the field, $u = t/\tau$, $\tau = 1$ fs, and $\pm$ is for the handedness of the circular pulse (+ for a right-handed circularly polarized pulse and - for a left-handed circularly polarized pulse). In the presence of an applied pulse with one cycle, electron's trajectory passes the Dirac point only one time in the reciprocal space.

We study residual conduction band population, the electric charge current, transferred charge, and transferred spin in the surface states of Bi_2Se_3 subjected to a one cycle circularly polarized pulse, two cycles of the circularly polarized pulse with same polarizations, and two cycles of the circularly polarized pulse with the opposite polarizations.

The distributions of residual conduction band population for applied one cycle right-handed polarized pulse in the reciprocal space near the Γ point are represented in Fig. 4.15. In this figure, the distributions are shown for different amplitudes of the applied field (0.05 V/Å, 0.10 V/Å, 0.15 V/Å, and 0.20 V/Å). For the single cycle of the pulse, the distribution includes interference fringes due to the warping terms in the effective low energy Hamiltonian.

The distributions of the residual conduction band population for applied one cycle left handed polarized pulse in the reciprocal space near the Γ point are represented in Fig. 4.16. Figures 4.15 and 4.16 show the chirality of the electron dynamics in surface states of $\mathrm{Bi_2Se_3}$ since two distributions for same amplitude of the applied field with different polarization are a mirror image of each other.

The applied two cycles of the circular pulse are expressed as following

$$\begin{aligned} F_x(t) &= \pm f_0(e^{-u^2}(1-2u^2) \pm e^{-(u-u_0)^2}(1-2(u-u_0)^2)) \\ F_y(t) &= 2f_0(ue^{-u^2} + (u-u_0)e^{-(u-u_0)^2}) \end{aligned} \tag{4.11}$$

where $u_0 = t_0/\tau$, the delay time for the second cycle $t_0 = 4$ fs, and $\tau = 1$ fs.

In the presence of the applied two cycles of the right-handed polarized pulse with the amplitudes of 0.1 V/Å, the residual conduction band population is shown in Fig. 4.17. The central part of distribution has interference fringes since electrons pass the Dirac point twice in the same direction.

In the presence of the applied two cycles of first right and then left-handed polarized pulses with the amplitudes of 0.1 V/Å, the residual conduction band population is shown in Fig. 4.18. The central part of distribution have interference fringes and it is viral due to the interference of pulses with opposite polarization. Additionally, there are interference fringes along six branches of the effective dipole matrix element.

Total residual conduction band populations for applied one cycle, two cycles with the same polarization and two cycles with opposite polarization are increasing monotonically by

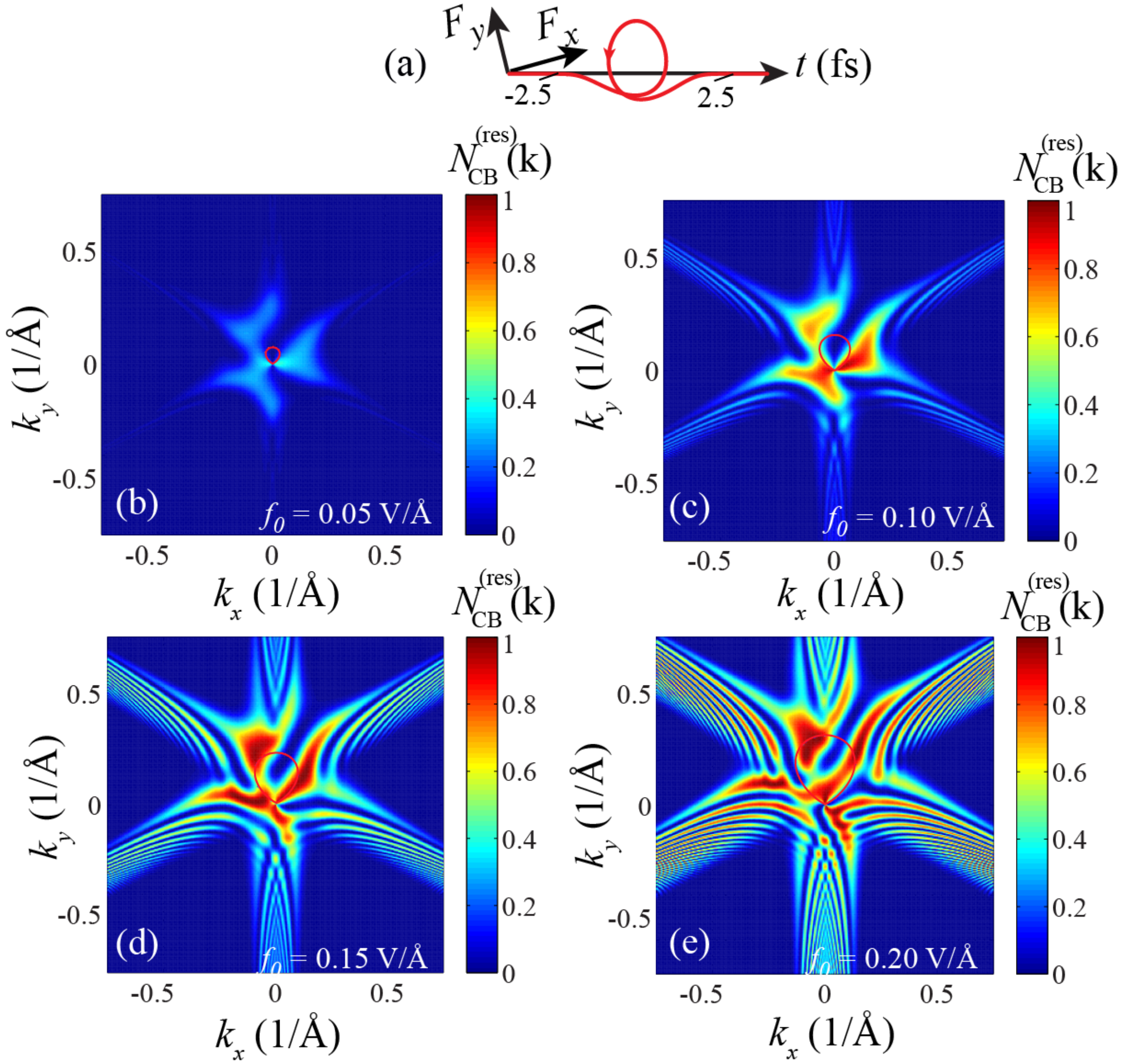

Figure (4.15) (color online) Residual conduction band population for (a) applied ultrafast right handed one cycle of circularly polarized pulse with amplitude (f_0) of (b) 0.05 V/Å, (c) 0.10 V/Å, (d) 0.15 V/Å, and (e) 0.20 V/Å. Red solid lines show the sparatrix corresponding to the amplitude of the applied field in each distribution.

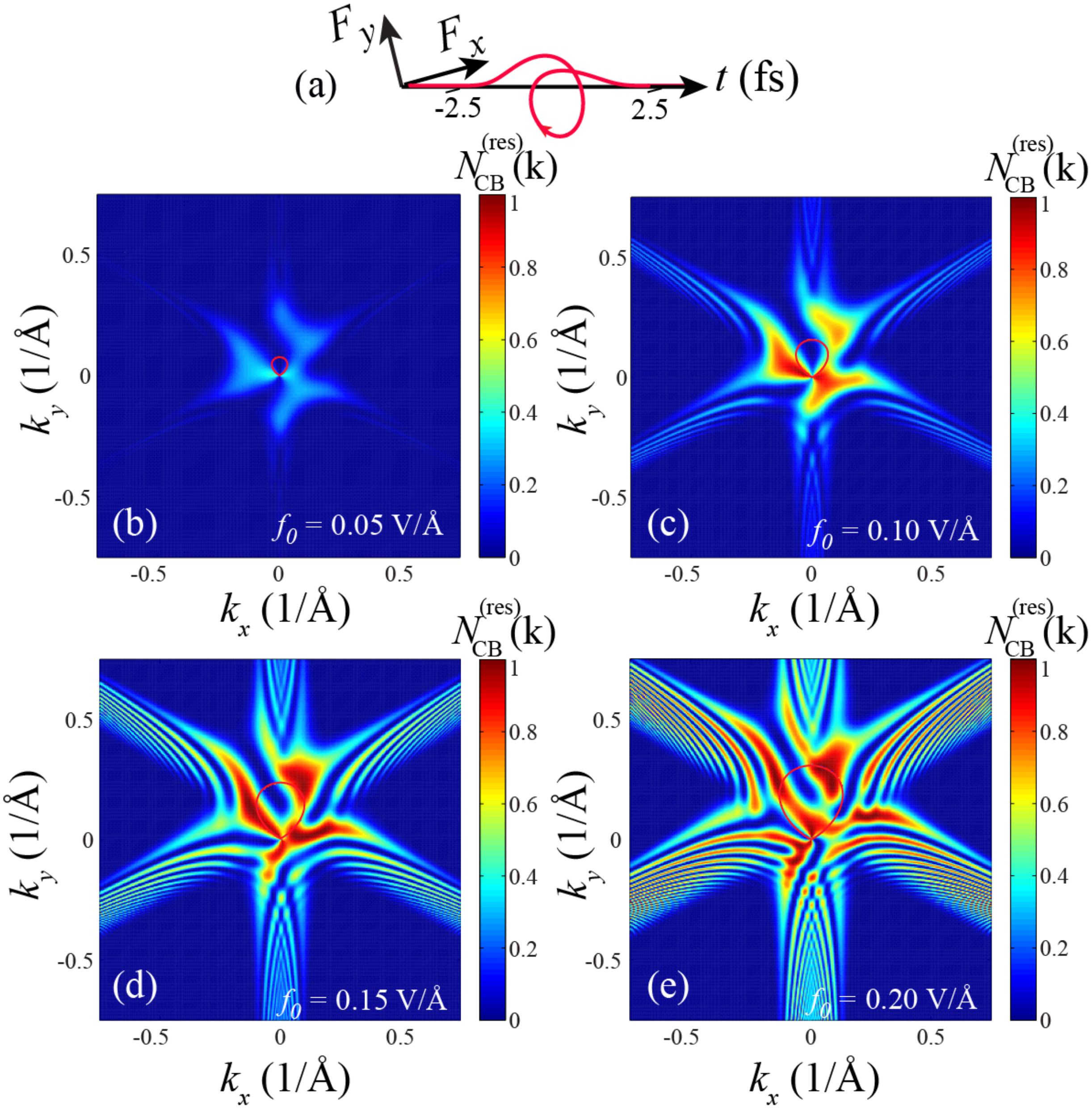

Figure (4.16) (color online) Residual conduction band population for (a) applied ultrafast left handed one cycle of circularly polarized pulse with amplitude (f_0) of (b) 0.05 V/Å, (c) 0.10 V/Å, (d) 0.15 V/Å, and (e) 0.20 V/Å. Red solid lines show the sparatrix corresponding to the amplitude of the applied field in each distribution.

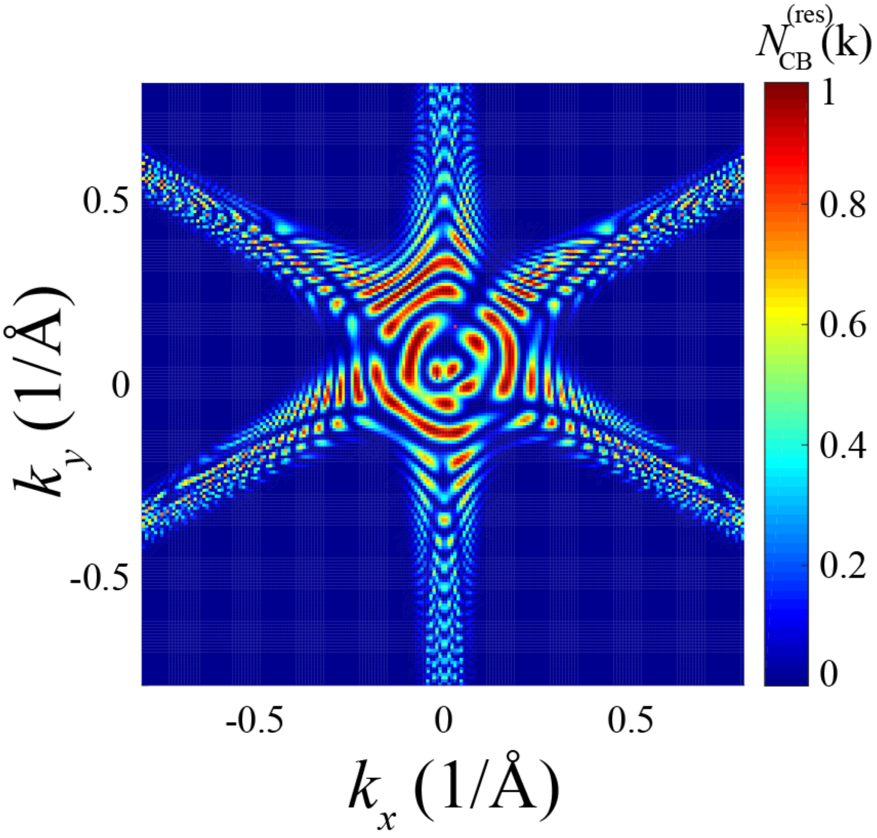

Figure (4.17) (Color online) Residual conduction band population for two-cycle right-handed circularly polarized pulse with the amplitude (f_0) of 0.1 V/Å.

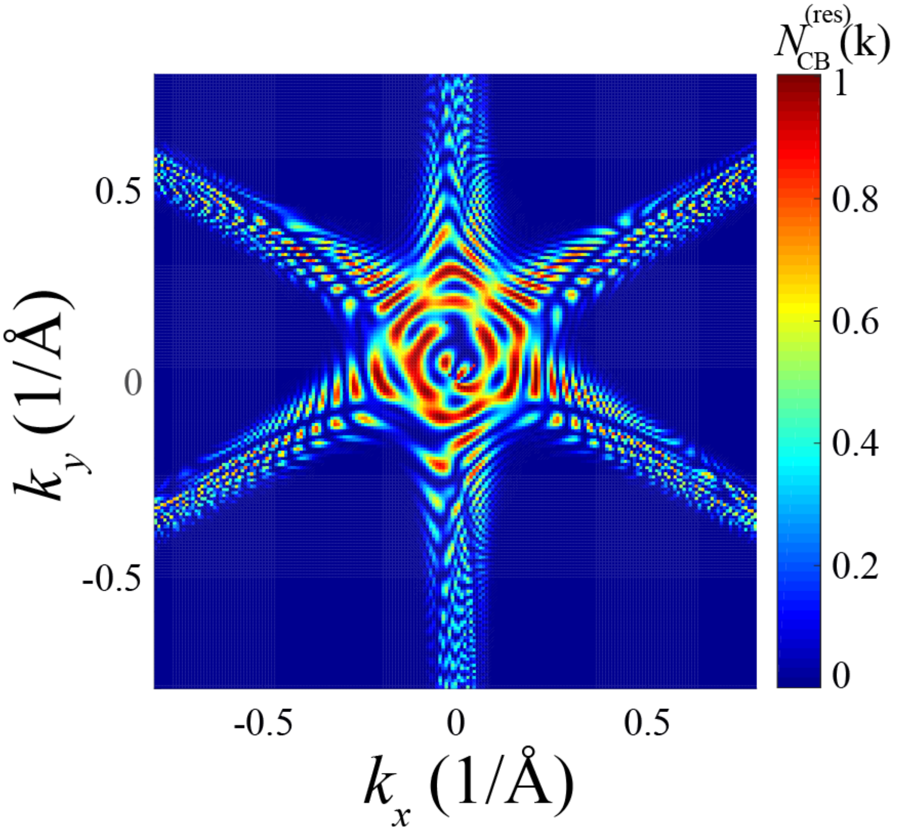

Figure (4.18) (Color online) Residual conduction band population for two-cycle one right-handed circularly polarized pulse and one left-handed circularly polarized pulse with the amplitude (f_0) of 0.1 V/Å.

increasing the amplitude of the applied field. For almost all amplitudes, the total residual conduction band for one cycle of the applied field is greater than the others.

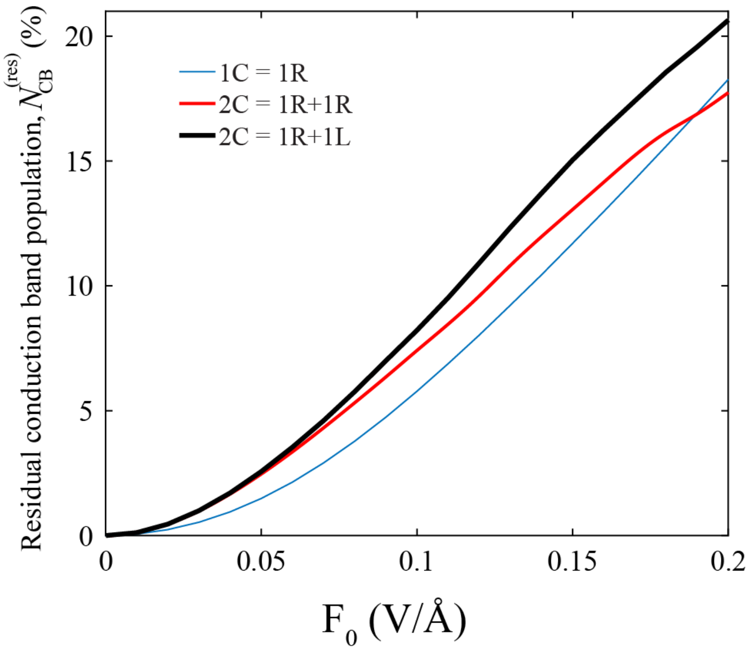

Figure (4.19) (Color online)Total residual conduction band population as a function of the amplitude of the applied one cycle right-handed circularly polarized pulse (blue line), two-cycle right-handed circularly polarized pulse (red line), two-cycle one right-handed circularly polarized pulse and one left-handed circularly polarized pulse (black line).

The asymmetric distribution of the conduction band population during the pulse creates current in both x and y directions. Fig. 4.20 shows the currents in x, J_x (a) and y J_y (b) directions for one cycle of the right-handed circularly polarized pulse. After the pulse ends, for the amplitudes of the field from 0 to 0.2 V/Å, J_x reaches almost zero. However the residual current in y-direction does not reach to zero for the $F_0 > 0.04$ V/Å. The maximum of J_y is almost 3 times larger than J_x for all amplitudes of the applied circular pulse.

For applied two cycles of the right-handed polarized pulse currents in x and y directions are shown in Fig. 4.21.

For applied one cycle of the right-handed and one cycle of the left-handed polarized pulse currents in x and y directions are shown in Fig. 4.22.

The transferred charge which is the integral of the current represents the residual polar-

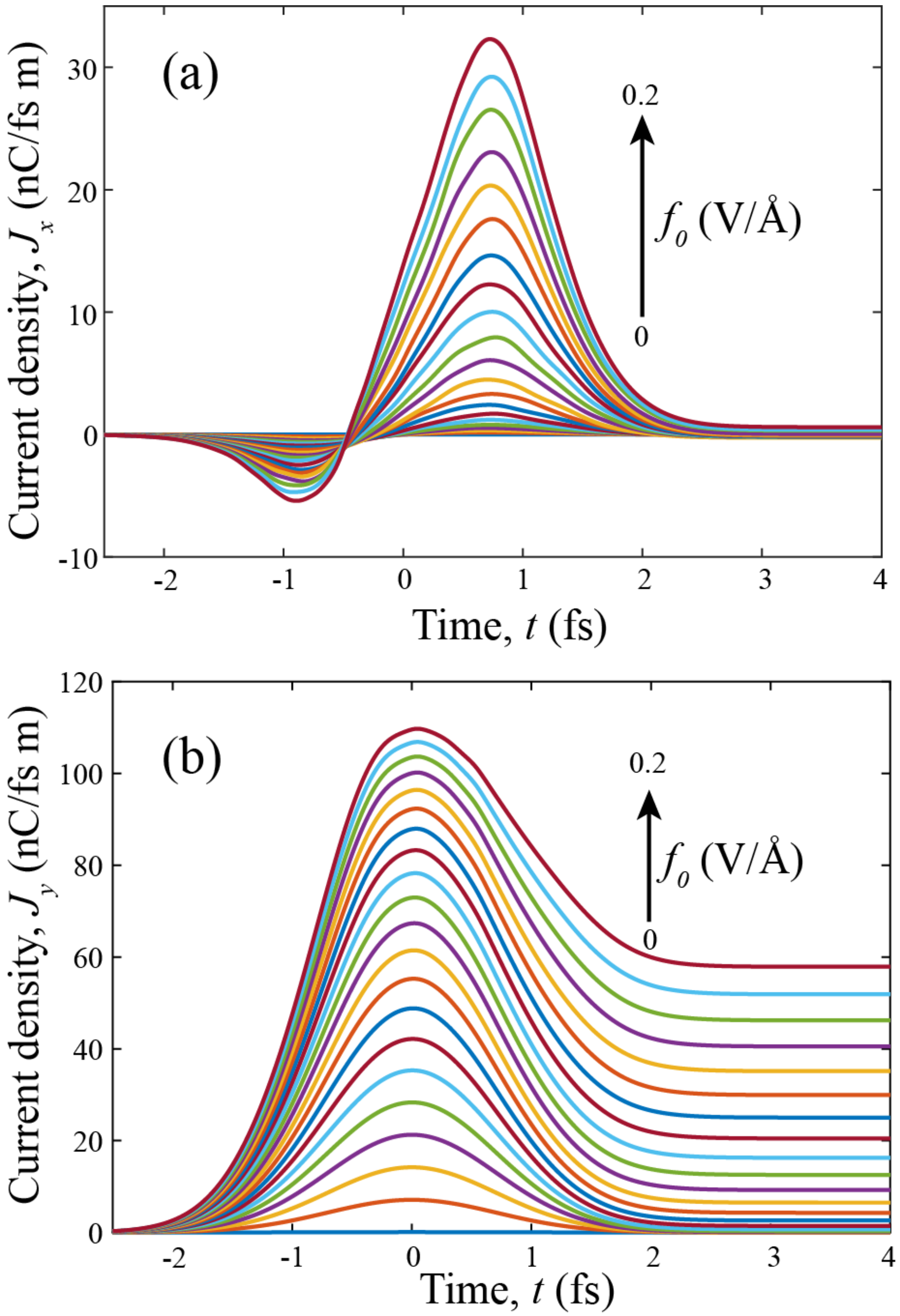

Figure (4.20) (Color online)Applied one cycle right-handed circularly polarized pulse (a) x-component of current density . (b) y-component of current density. The amplitude of the electric field changes from 0 to 0.2 V/Å.

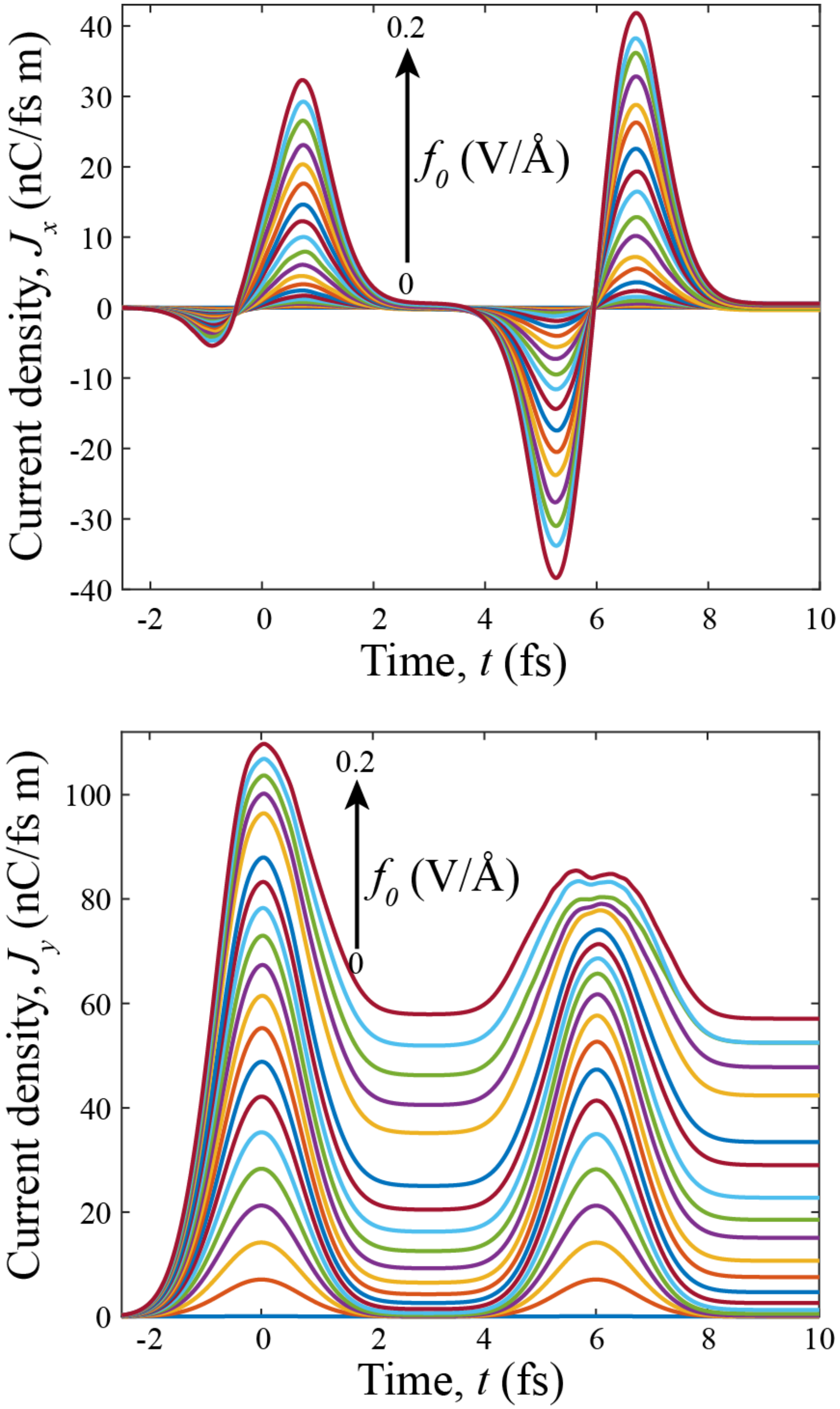

Figure (4.21) (Color online) (a) x-component of current density for applied 2-cycle right-circular polarized pulse. (b) y-component of current density for applied 2-cycle right-circular polarized pulse. The amplitude of the electric field is changed from 0 to 0.2 V/Å.

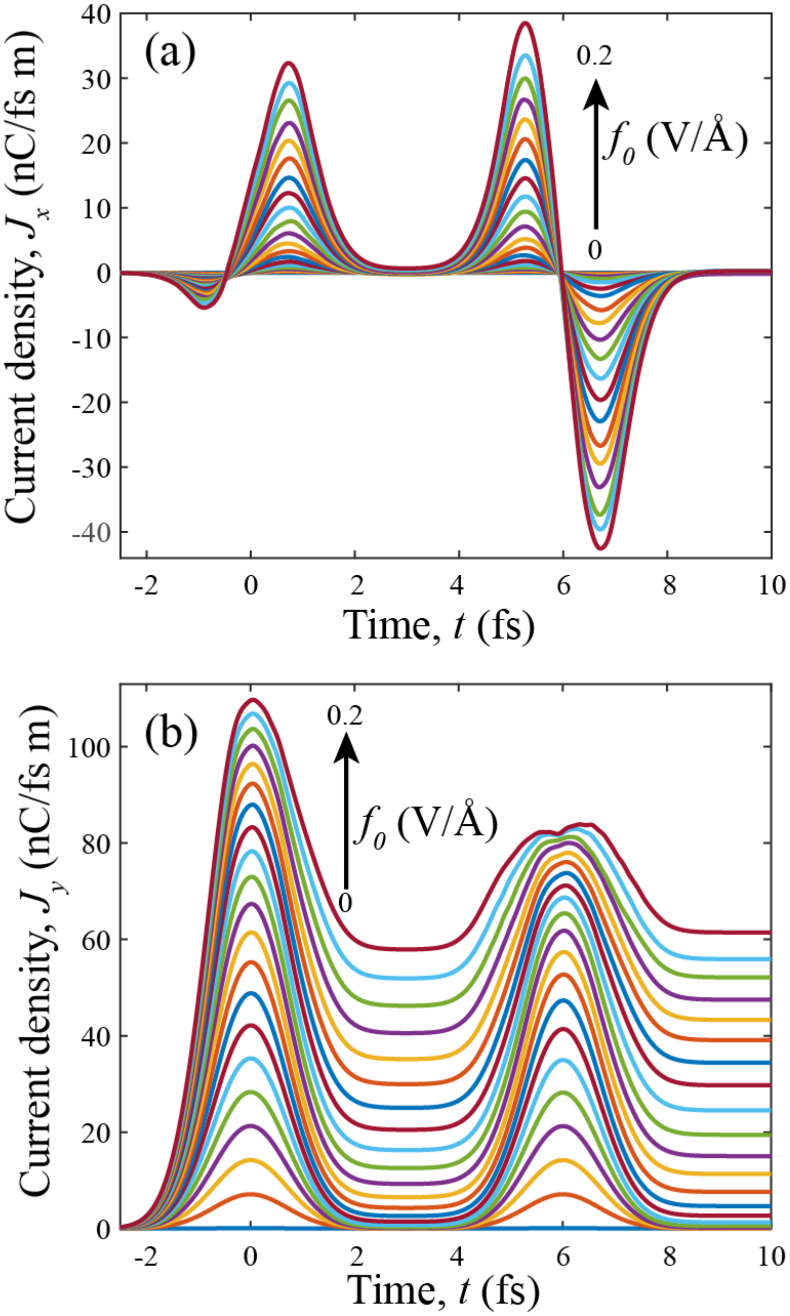

Figure (4.22) (Color online) (a) x-component of current density for applied 1-cycle right-circular polarized pulse and 1-cycle left-circular polarized pulse. (b) y-component of current density for applied 1-cycle right-circular polarized pulse and 1-cycle left-circular polarized pulse. The amplitude of the electric field is changed from 0 to 0.2 V/Å.

ization of a 2D material subjected to the ultrafast field. Fig. 4.23 represents the transferred charges in the x and y directions for applied one cycle and two cycles with same polarization and two cycles with opposite polarization. As shown in this figure, one cycle of the pulse creates fewer transferred charges in both the x and y directions. Additionally, the two cycles with the same polarization and two cycles with opposite polarization create almost the same number of transferred charges for different amplitudes of the applied field since they create the same current profile in the y-direction.

In addition to the transferred electric charge, there is transferred spin on the surfaces of a topological insulator due to the important property of the surfaces of the topological insulators which is the spin of an electron is locked to its momentum.

Fig. 4.24 represents the different transferred components of the spin for applied one cycle and two cycles with same polarization and two cycles with opposite polarization of circular pulse.

4.3 Conclusion

We study ultrafast electron dynamics of a 2D electron system on the surface of a 3D topological insulator. The electron dynamics in such system is highly irreversible and anisotropic. The irreversibility of the electron dynamics is due to zero band gap of the surface states. In this case, the interaction of the laser pulse with the system satisfies the nonadiabatic condition, $\omega_0 \Delta_g/\hbar$, where ω_0 is the laser frequency and Δ_g is the band gap. The anisotropy is due to cubic terms in the effective Hamiltonian of the system, which results in the anisotropy of the interband dipole matrix elements near the Dirac point. Such anisotropy produces hot spots in the distribution of the conduction band population in the reciprocal space, where the number of the spots depends on the polarization of the optical pulse. Redistribution of the electrons between the conduction and valence bands generates the electric current during the pulse. The magnitude of the current is also anisotropic and depends on the polarization of the pulse. Moreover, for a circularly polarized light the response of the system, unlike graphene, depends on the chirality (helicity) of the incident

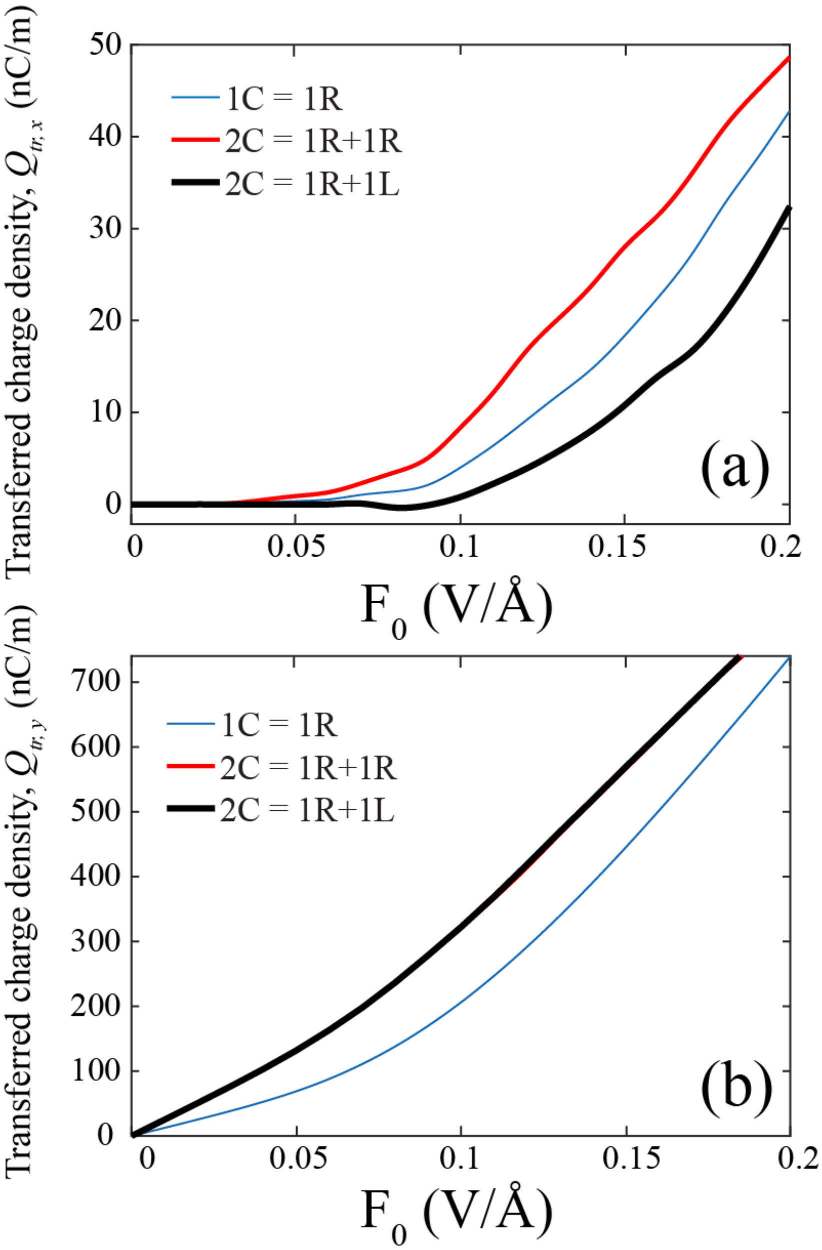

Figure (4.23) (Color online)Total transferred charge as a function of the amplitude of the applied one cycle right-handed circularly polarized pulse (blue line), two-cycle right-handed circularly polarized pulse (red line), two-cycle one right-handed circularly polarized pulse and one left-handed circularly polarized pulse (black line) (a) in x direction, and (b) in y direction.

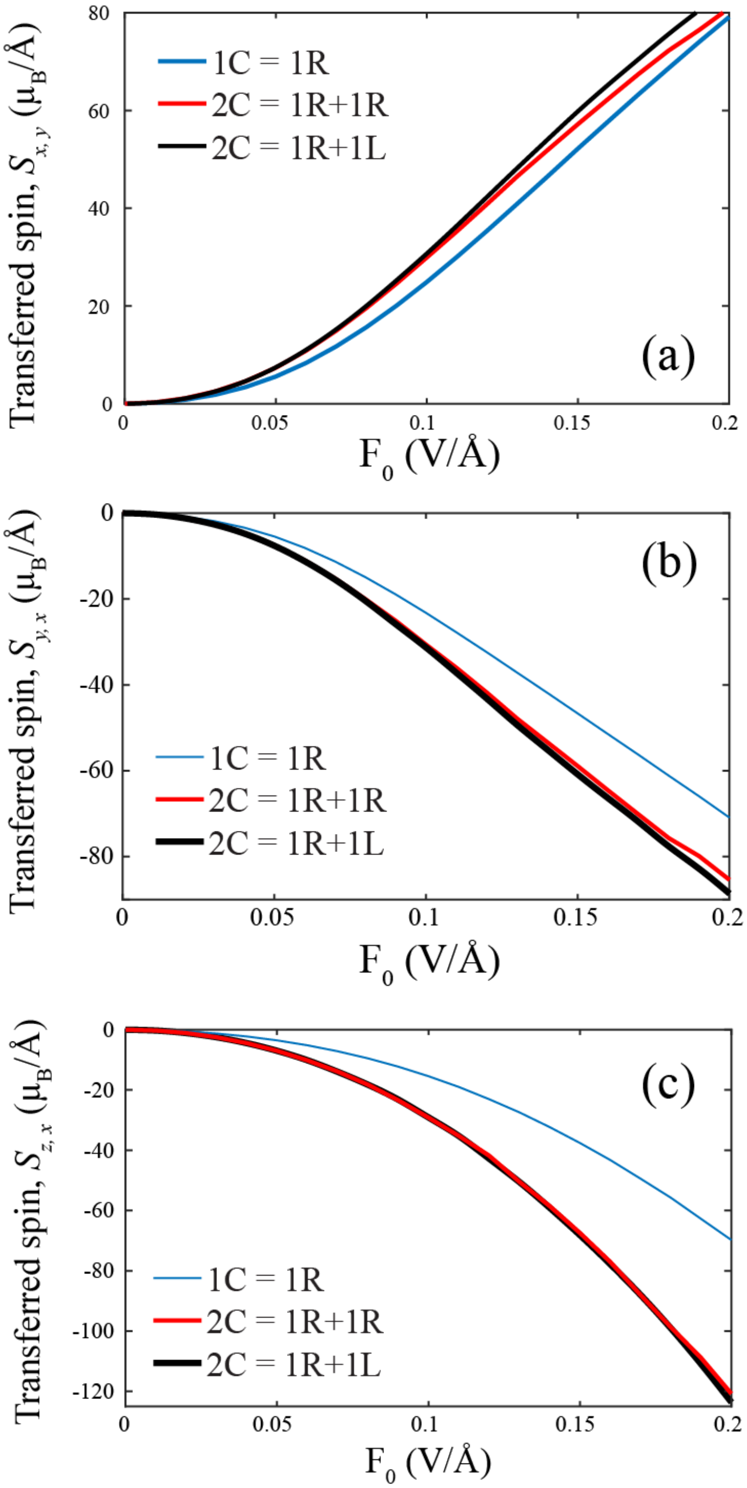

Figure (4.24) (Color online)Total transferred spin as a function of the amplitude of the applied one cycle right-handed circularly polarized pulse (blue line), two-cycle right-handed circularly polarized pulse (red line), two-cycle one right-handed circularly polarized pulse and one left-handed circularly polarized pulse (black line) (a) the x component of the spin in in y direction, and (b) the y component of the spin in in x direction, and (c) the z component of the spin in in x direction .

pulse. This is due to the hexagonal warping terms which are responsible for breaking full rotational symmetry down to three-fold rotational symmetry. Additionally, we calculated the transferred spin which can be used in spintronics applications.

CHAPTER 5

CRYSTALLINE TOPOLOGICAL INSULATOR

5.1 Introduction

Crystalline topological insulators (CTIs) belong to a new class of 3D topological insulators (TIs) in which a certain point group symmetry along with the time reversal symmetry (TR) protect conducting surface states [96, 97, 98]. In another word , the group symmetry of CTIs plays the role of spin-orbit coupling of TIs in protecting the metallic surfaces. Therefore breaking either T symmetry or group symmetry can destroy the conducting states.

Surface states of CTI that we choose to study electron dynamics have quadratic degeneracy, and they are protected by C4 symmetry as well as T symmetry [96].So it is interesting enough to investigate electron dynamics in the single valley quadratic surface state of CTI. Here we consider ultrafast electron dynamics in 2D electron systems, which, similar to graphene, are semimetals, but with a quadratic electron-energy dispersion. Such systems are realized at the surface of crystalline topological insulators (CTIs) [96], where the surface states are protected by the time-reversal and discrete rotational symmetries. An example of such a CTI is a tetragonal crystal with the C_4 symmetry, where the quadratic gapless bands are predicted to occur at the (001) crystal face [96]. We study below the electron dynamics in such materials under ultrashort optical pulses assuming that the dynamics is coherent and considering low-energy effective models for the surface state of CTI. The assumption that the electron dynamics are coherent, is valid as long as the duration of the pulse, which is ≈ 4 fs, is less than the characteristic electron scattering time in these materials, which one would expect on the time scale longer than 10 fs as in graphene – see below in the next paragraph.

Experimentally, the processes of energy-momentum relaxation in the photoexcited CB electron population occur during times ranging from $\sim 10 - 20$ fs to $\sim 200 - 800$ fs [54, 55, 56, 57, 58, 59, 60, 61]

We predict below that the ultrafast interband electron dynamics in CTIs results in characteristic CB electron distribution, which is formed due to the quantum-mechanical interference of the excitation events during consecutive crossing of lines in the reciprocal space of $\mathbf{k}_x = \epsilon \mathbf{k}_y$ (where $|\epsilon| \leq 1$ is a constant) near the degeneracy point (Γ-point) in the reciprocal space. At these lines, the dipole transitions are strongly enhanced. A fundamental difference from graphene is a high degree of anisotropy of the low energy dispersion, which results in a strong dependence on the polarization plane of the optical pulse. In particular, the CB population distribution in the reciprocal space has a single-peak or double-peak structure for different polarizations of the optical pulse.

5.1.1 Effective Low Energy Model

We describe surface states of a CTI within an effective low-energy $\mathbf{k}\cdot\mathbf{p}$ model determined by the following Hamiltonian [96]

$$\mathcal{H}_0 = \frac{\hbar^2 k^2}{2m_0} + \frac{\hbar^2 (k_x^2 - k_y^2)}{2m_1}\sigma_z + \frac{\hbar^2 k_x k_y}{2m_2}\sigma_x, \tag{5.1}$$

where σ_x, σ_z are Pauli matrices, m_0, m_1, m_2 are effective masses, (k_x, k_y) is a 2D wave vector with magnitude k. The Hamiltonian, $\mathcal{H}_0$, describes the valence band (VB) and the CB with the following energy dispersion

$$E_{c,v} = \frac{\hbar^2 k^2}{2m_0} \pm \hbar^2 \sqrt{\left(\frac{k_x^2 - k_y^2}{2m_1}\right)^2 + \left(\frac{k_x k_y}{2m_2}\right)^2} \tag{5.2}$$

The energy dispersion shown in Fig. 5.1 has quadratic band degeneracy at $k = 0$ which is anisotropic. With the known wave functions of the conduction and valence bands calculated from Hamiltonian (5.1), we obtain the following expressions for the x and y components of

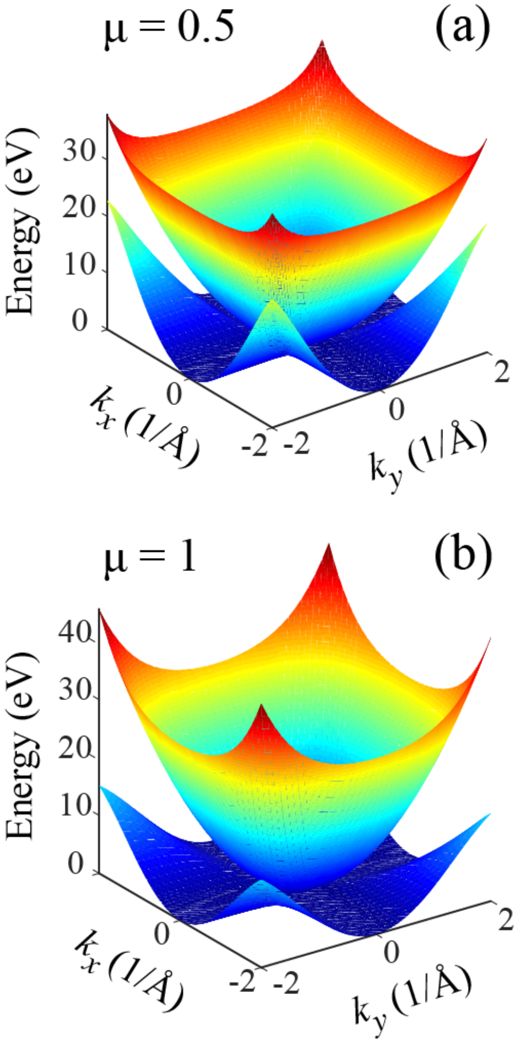

Figure (5.1) Energy dispersion for (a) $\mu = 0.5$ and (b) $\mu = 1$. $\mu = m_1/m_2$ where $m_0 = m1 = m_e$ and m_e is electron mass the dipole matrix elements:

$$D_x(\mathbf{k}) = \frac{e}{2i}\mu\frac{k_y\left(k_x^2+k_y^2\right)}{\left(k_x^2-k_y^2\right)^2+k_x^2k_y^2\mu^2} \tag{5.3}$$

and

$$D_y(\mathbf{k}) = \frac{-e}{2i}\mu\frac{k_x\left(k_x^2+k_y^2\right)}{\left(k_x^2-k_y^2\right)^2+k_x^2k_y^2\mu^2}, \tag{5.4}$$

where $\mu = m_1/m_2$. The dipole matrix elements, D_x and D_y, have maxima at the degeneracy point, $k = 0$. Near this point, the properties of the interband dipole coupling depend on polarization of the optical pulse, i.e. on angle θ, and on the ratio of effective masses, μ. For a given linear polarization of the pulse, the effective interband coupling is determined by the following expression

$$D_\theta(\mathbf{k}) = D_x(\mathbf{k})\cos\theta + D_y(\mathbf{k})\sin\theta. \tag{5.5}$$

The intraband dynamics determines the electron trajectory in the reciprocal space, which is along the direction of polarization of the pulse as given by Eq. (2.5). Along this trajectory, the interband coupling is characterized by effective dipole matrix element D_θ. Depending on polarization direction, dipole matrix element $D_\theta(\mathbf{k})$ as as function of crystal momentum k has either one or two peaks, as illustrated in Fig. 5.2. This is in contrast to a graphene monolayer, for which the effective coupling always has only one peak.

For the pulse polarization along the axis of symmetry of the system, i.e., axis x or y, the dipole coupling has two peaks – cf. Fig. (5.2) (a) and (b). For example, for $\theta = 0$ (polarization along axis x), the effective coupling is $D_{\theta=0} = D_x$, see Eq. (5.3). In the reciprocal space, dipole matrix element D_x has two maxima as shown in Figs. 5.2 (a) and (b). These maxima are at

$$\frac{k_x}{k_y} = \pm\sqrt{\sqrt{4-\mu^2}-1}. \tag{5.6}$$

With decreasing μ, the corresponding peaks become narrower as shown in Fig. 5.2 (b), while the area under each peak does not depend on μ, i.e., $\int_{-\infty}^{0} D_x dk_x = \int_0^\infty D_x dk_x = e\pi/2i$. For a generic direction of polarization, i.e. $\theta \neq \pi/4$, the effective dipole matrix element, D_θ, always has two peaks in the reciprocal space similar to Figs. 5.2 (a) and (b). Only for for $\theta = \pi/4$, this behavior degenerates to having only one peak as shown in Figs. 5.2 (c) and (d).

These matrix elements have the following forms

$$V_x^{cc} = \hbar k_x \left(\frac{1}{m_0} + \frac{1}{m_1} \frac{(k_x^2 - k_y^2) + \frac{1}{2}\mu^2 k_y^2}{\sqrt{(k_x^2 - k_y^2)^2 + \mu^2 (k_x k_y)^2}} \right), \tag{5.7}$$

$$V_y^{cc} = \hbar k_y \left(\frac{1}{m_0} + \frac{1}{m_1} \frac{(k_y^2 - k_x^2) + \frac{1}{2}\mu^2 k_x^2}{\sqrt{(k_x^2 - k_y^2)^2 + \mu^2 (k_x k_y)^2}} \right), \tag{5.8}$$

$$V_x^{vv} = \hbar k_x \left(\frac{1}{m_0} - \frac{1}{m_1} \frac{(k_x^2 - k_y^2) + \frac{1}{2}\mu^2 k_y^2}{\sqrt{(k_x^2 - k_y^2)^2 + \mu^2 (k_x k_y)^2}} \right), \tag{5.9}$$

$$V_y^{vv} = \hbar k_y \left(\frac{1}{m_0} - \frac{1}{m_1} \frac{(k_y^2 - k_x^2) + \frac{1}{2}\mu^2 k_x^2}{\sqrt{(k_x^2 - k_y^2)^2 + \mu^2 (k_x k_y)^2}} \right). \tag{5.10}$$

5.2 Results and Discussion

The results presented in this Section have been obtained for the following parameters of the system: $m_0 = m_e$, $m_1 = m_e$, and different values of parameter $\mu = m_1/m_2$, where m_e is electron mass.

In Fig. 5.3 the residual conduction band population, $N_{CB}^{(res)}(\mathbf{k})$, is shown as a function of wave vector $\mathbf{k}$ for different polarizations , i.e., angle θ, of the optical pulse and different values of parameter μ. The distribution of $N_{CB}^{(res)}(\mathbf{k})$ shows high contrast peaks, localized near the local maximum of the effective interband dipole coupling –cf. Fig. 5.2. Note the 4-fold rotational symmetry of distribution $N_{CB}^{(res)}$ in Fig. 5.3.

In Fig. 5.3, a region of large $N_{CB}^{(res)}$ contains fringes of high and low residual CB population. These fringes are due to the interference of two passages per optical period of the same region of enhanced interband coupling (see Appendix for more discussion). This fringe

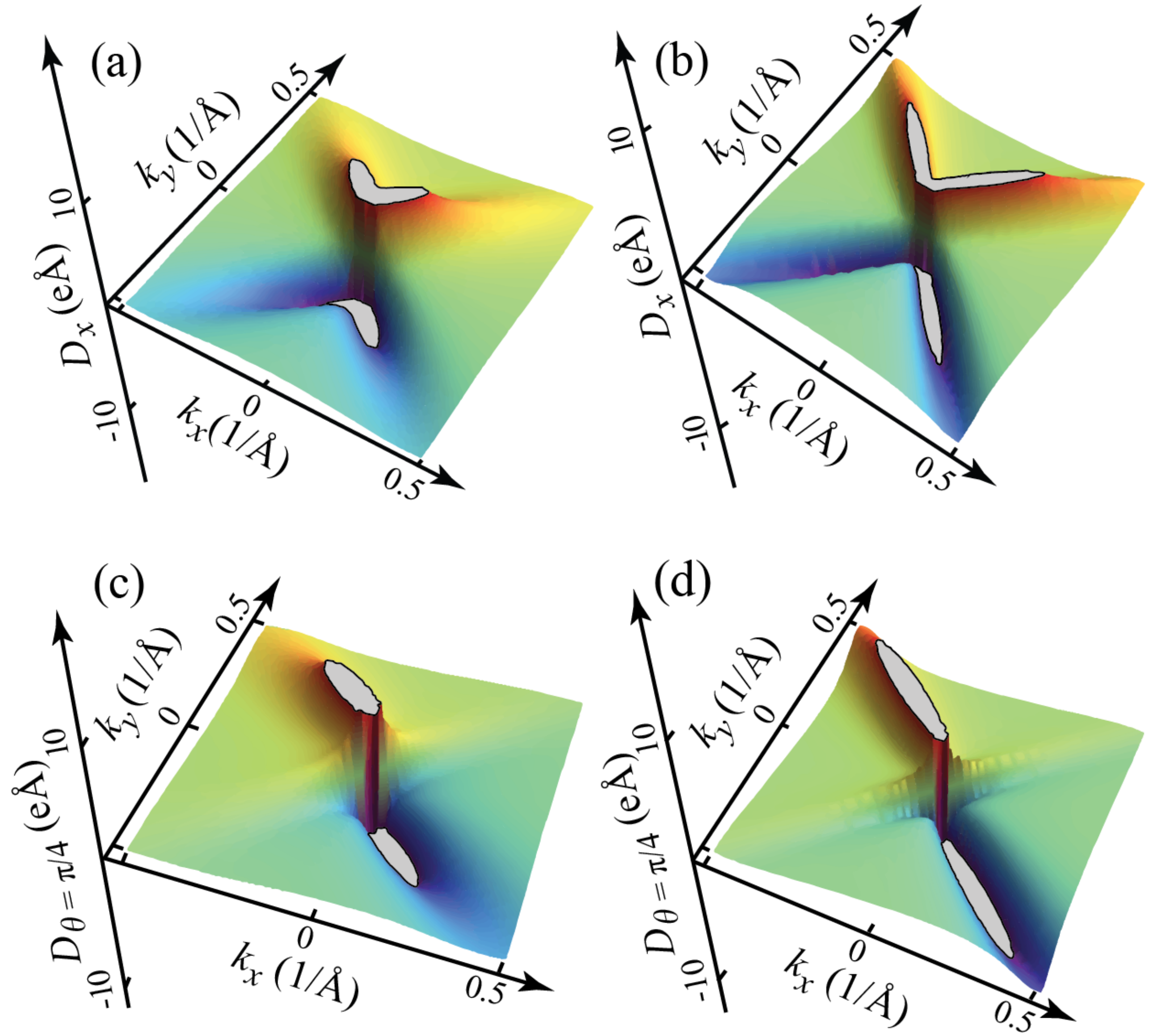

Figure (5.2) Interband dipole matrix element D_θ. (a) Polarization of the pulse is along axis x ($\theta = 0$) and $\mu = 1$. (b) The same as (a) but for $\mu = 0.5$. (c) Polarization of the pulse is along the diagonal ($\theta = \pi/4$) and $\mu = 1$. (d) The same as (c) but for $\mu = 0.5$.

structure is more developed with larger number of fringes for smaller values of μ [see Figs. 5.3 (d)-(f)]. This is due the fact that D_x becomes more localized and extended to larger values of k_y for smaller values of μ [see Fig. 5.2(a)]. This fringe structure is a self-referenced interferogram that contains information about dispersion and topological curvature of the electronic bands.

The net residual CB population, $N^{(res)}$, is shown in Fig. 5.4 as a function of the pulse amplitude, F_0. The dependence of $N^{(res)}$ on angle θ is different for smaller, $\mu = 0.5$, and larger, $\mu = 1.0$, values of μ. For $\mu = 0.5$, the net CB population is almost isotropic for all amplitudes of the pulse with small anisotropy at $F_0 < 1$ V/Å – see Fig. 5.4(b). For $\mu = 1.0$, the net CB population is isotropic for small field amplitudes, but becomes highly anisotropic at large amplitudes, $F_0 > 1.0$ V/Å – see Fig. 5.4(a). At such large amplitudes, the residual CB population is the smallest at $\theta = 0$. Similar anisotropy is also expected for $\mu = 1.0$, but for larger pulse amplitude, $F_0 > 2$ V/Å. The origin of such anisotropy is the overlap of two regions of large $N_{CB}^{(res)}(\mathbf{k})$ for polarization angle $\theta = 0$. These regions correspond to two maxima of interband dipole coupling, D_x. Since these maxima are more localized for smaller values of μ, then the anisotropy in $N^{(res)}(\theta)$ is more pronounced at $\mu = 0.5$.

The finite CB population during the pulse also produces an electric current, $\mathbf{J}(t)$, which can be found from Eq. (2.17). In Fig. 5.5, the current density, $\mathbf{J}(t)$, is shown as a function of time together with the corresponding vector potential, which is the time integral of the electric field. The current density almost follows the profile of the vector potential. The generated electric current results in finite charge transfer, Q_{tr}, which is defined by Eq. (2.14). From the current dynamics, shown in Fig. 5.5, it follows that the transferred charge is positive, which means that the direction of the charge transfer is the same as the direction of the field maximum.

The calculated transferred charge is shown in Fig. 5.6 as a function of the field amplitude, F_0. The transferred charge is positive for all F_0. It is approximately inversely proportional to parameter μ (see Fig. 5.6). There is also a weak dependence of Q_{tr} on the pulse polarization, i.e., angle θ. While for the net residual CB population, there is a strong dependence of

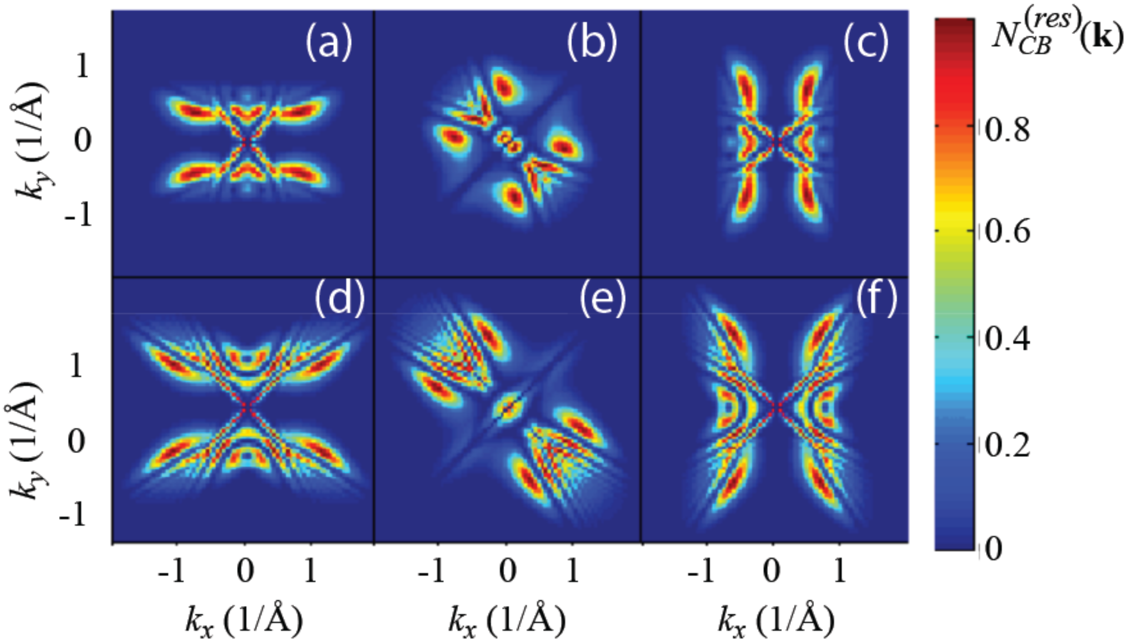

Figure (5.3) Residual conduction band population $N_{CB}^{(res)}$ as a function of wave vector $\mathbf{k}$ for different values of parameter μ and angle θ. The amplitude of the pulse is $F_0 = 1$ V/Å. (a) $\mu = 1$, $\theta = 0$; (b) $\mu = 1$, $\theta = \pi/4$; (c) $\mu = 1$, $\theta = \pi/2$; (d) $\mu = 0.5$, $\theta = 0$; (e) $\mu = 0.5$, $\theta = \pi/4$; (f) $\mu = 0.5$, $\theta = \pi/2$.

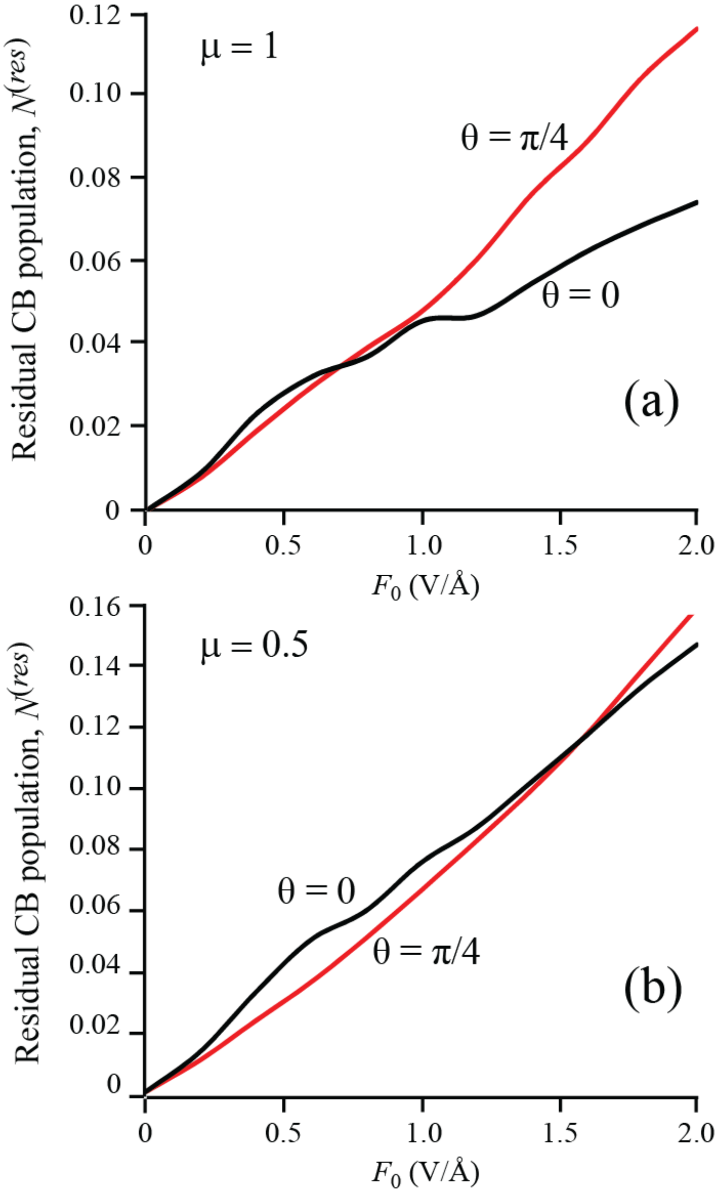

Figure (5.4) Residual conduction band population as a function of pulse amplitude F_0 for different values of angle θ (polarization of the pulse) and parameter μ. The black lines correspond to $\alpha = 0$ (polarization along axis x) and the dashed lines show the results for $\theta = \pi/4$. The values of parameter μ are 1.0 (a) and 0.5 (b).

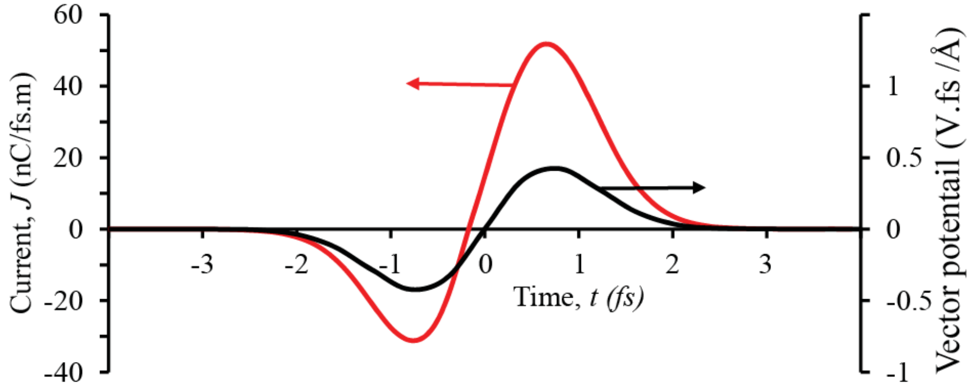

Figure (5.5) Electric current density as a function of time for amplitude $F_0 = 1.0$ V/Å. The parameter μ is 1.0. The red line shows the corresponding vector potential.

$N^{(res)}$ on angle θ, e.g., at $\mu = 1$ and $F_0 = 2.0$ V/Å, $N^{(res)}$ changes by almost 50% with θ, the transferred charge is almost isotropic with angle variations less than 5%.

For $\mu = 0.5$, the transferred charge, Q_{tr}, has the largest value at polarization angle $\theta = \pi/4$ for all amplitudes of the pulse. For $\mu = 1.0$, the transferred charge as a function of angle θ has maximum value at $\theta = 0$ for small amplitudes, $F_0 < 1$ V/Å, while at large amplitudes, $F_0 > 1$ V/Å, the maximum of Q_{tr} is realized at $\theta = \pi/4$. Thus, if Q_{tr} is measured as a function of angle θ at a given amplitude of the pulse, then for different amplitudes F_0 we expect different behavior. While for all F_0 the transferred charge as a function of θ has the periodicity of $\pi/2$, the positions of maxima and minima depend on F_0 and μ. If the system is characterized by parameter $\mu = 0.5$, then for all amplitudes F_0, the maximum of Q_{tr} occurs at $\theta = \pi/4$ and the minimum is at $\theta = 0$ or $\pi/2$. For larger values of μ, e.g., $\mu = 1.0$, at small amplitude F_0, the maximum of Q_{tr} is at $\theta = 0$ (or $\pi/2$) and the minimum is at $\theta = \pi/8$ [see 5.7(b)]. At larger amplitude F_0, the maximum of Q_{tr} is at $\theta = \pi/8$ and the minimum is at $\theta = 0$ $(\pi/2)$ - see Fig. 5.7(a).

To illustrate the nonmonotonic dependence of the residual conduction band population in the reciprocal space along the line of maxima of the interband dipole matrix element, i.e., along the dashed green lines shown in Fig. 5.2 we consider a simplified model of the interband coupling. For concreteness we assume that the pulse is polarized along axis x $(\theta = 0)$. In this case, the interband dipole matrix element as a function of k_x has two maxima. We consider

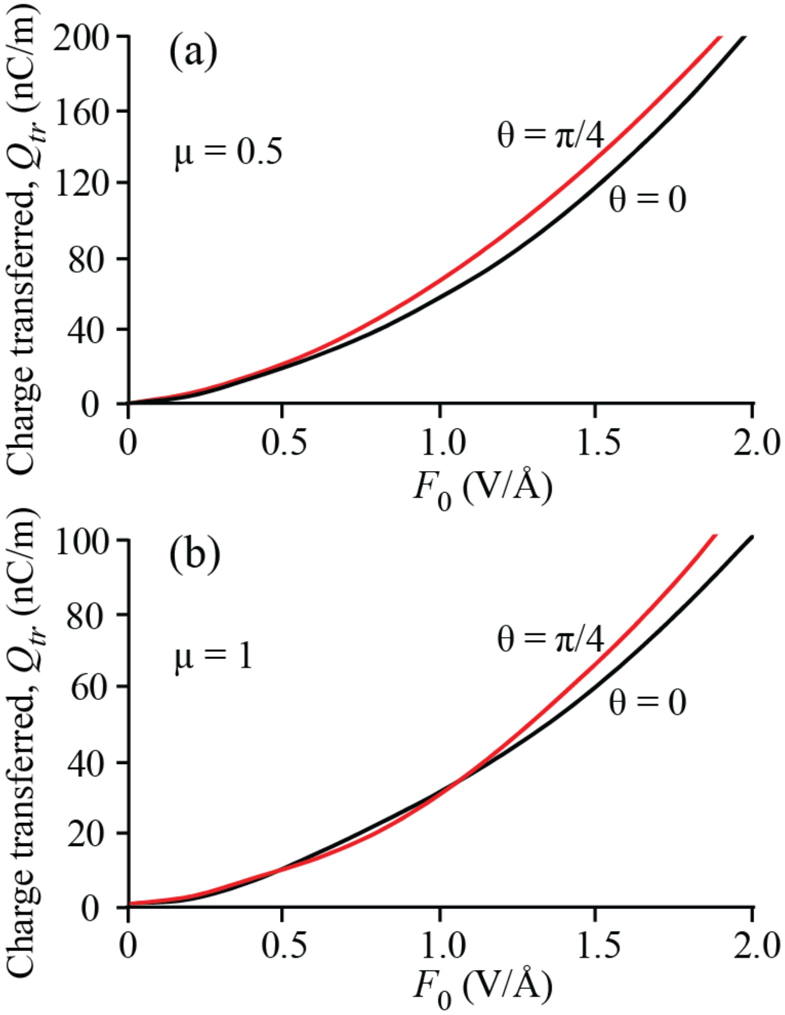

Figure (5.6) Transferred charge density through the system as a function of F_0 for different values of parameter μ and angle θ (polarization of the pulse).

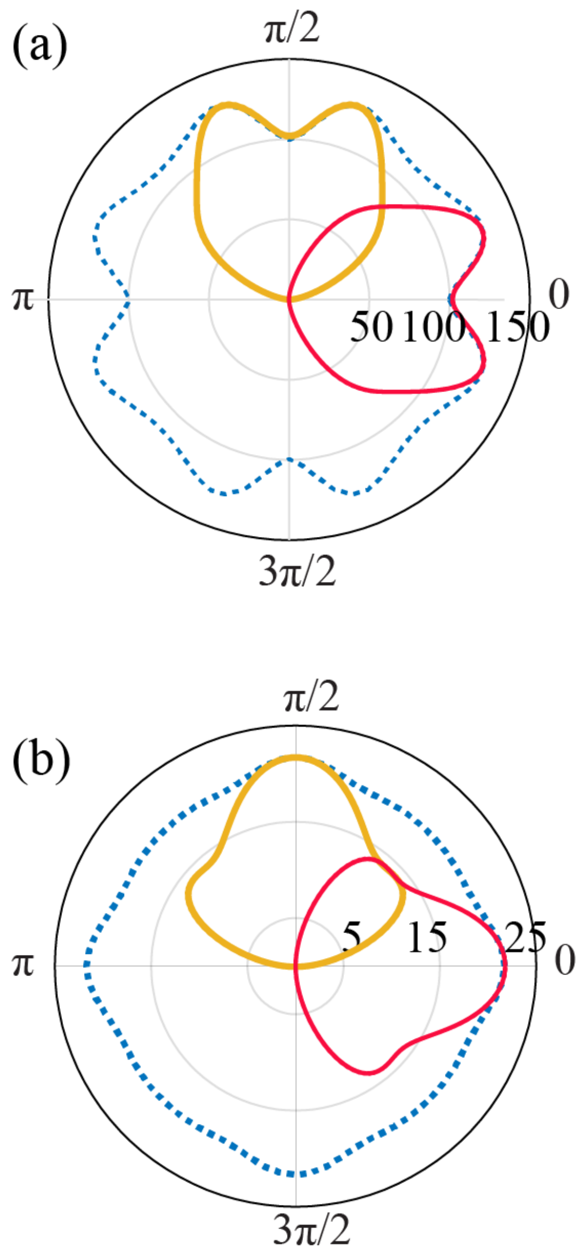

Figure (5.7) Transferred charge density through the system as a function of angle θ for $\mu = 1.0$. The transferred charge is calculated along the direction of polarization of the pulse. The amplitude of the optical pulse is (a) $F_0 = 2.0$ V/Åand (b) $F_0 = 0.8$ V/Å. Red and yellow solid lines show x and y components of transferred charges respectively.

the electron dynamics near one these maxima.

For x-polarized optical pulse the electron trajectory is determined by acceleration theorem and is shown schematically in Fig. 5.8(a) for initial wave vector $(k_{x,0}, k_{y,0})$. Such trajectory passes twice though the maximum of the dipole matrix elements, which is shown by dashed line. Such passages occur at moments of time t_1 and t_2. These moments of time correspond to equal values of vector potential as shown in Fig. 5.8(b). At these points the electric field has different values, F_1 and F_2 – see Fig. 5.8(c).

(a) Dashed lines show the positions of the maxima of the interband dipole coupling. The red line illustrates the electron trajectory in the reciprocal space, where $(k_{x,0}, k_{y,0})$ is the initial electron wave vector. The electron trajectory passes twice the region of large interband coupling (dashed line) at two moments of time, t_1 and t_2. These passages are shown by green dots (for x-polarized pulse these points coincide, but for illustration purpose the dots are shifted in space). (b) Vector potential of the optical pulse as a function of time. The moments of time t_1 and t_2 are the same as in panel (a). At these moments the vector potential is the same. (c) The electric field of the optical pulse as a function of time. At the moments of time t_1 and t_2 the magnitudes of electric field are not the same, $F_2 > F_1$.

To describe the interband dynamics corresponding to the trajectory shown in Fig. 5.8(a) we approximate the interband dipole coupling by step-like function, which is nonzero and constant only within narrow interval $k_{x,max} - \delta_x/2 < k_x < k_{x,max} + \delta_x/2$, where $k_{x,max}$ is the position of the maximum of D_x and δ_x is the width of the maximum – see Fig. 5.9. The value of the dipole matrix element within this interval is $i\delta_0/e$, where Δ_0 is related to Δ_x as $\Delta_0\delta_x = \pi/2$. The value of dipole matrix element at the peak and correspondingly the width of the peak depend on $k_{y,0}$. With increasing $k_{y,0}$, maximum D_0 decreases and width Δ_0 increases.

δ_x and its height Δ_0. Red line illustrates part of the electron trajectory in the reciprocal space – see Fig. 5.8(a). The trajectory passes twice through the maximum of the interband coupling. Along the trajectory strong interband mixing occurs only between points "1" and "2", and "3" and "4". The values of $\hat{\beta}$ at points "2" and "1" are related by transfer matrix T_1, at points "2" and "3" - by accumulation of dynamic phase, which is described by rotational matrix R, and at points "3" and "4" - by transfer matrix T_2.

We also assume that the width δ_x is small so that within the region of nonzero constant dipole matrix element, the energies, E_c and E_v, of VB and CB levels and electric field, F_c, are constant. Under these assumptions, the interband mixing occurs only within the region $k_{x,max} - \delta_x/2 < k_x < k_{x,max} + \delta_x/2$, where the system of Eqs. (**??**)-(**??**) takes the form

$$\frac{d\beta_{c\mathbf{q}}(t)}{dt} = -\frac{i}{\hbar}\Delta_0 F_c e^{-i(E_c-E_v)t/\hbar}\beta_{v\mathbf{q}}(t) \tag{5.11}$$

$$\frac{d\beta_{v\mathbf{q}}(t)}{dt} = -\frac{i}{\hbar}\Delta_0 F_c e^{-i(E_c-E_v)t/\hbar}\beta_{c\mathbf{q}}(t). \tag{5.12}$$

Taking into account acceleration theorem (2.4), we change the variable from t to k_x in the system of Eqs. (5.11)-(5.12). The new system of equations becomes

$$\frac{d\beta_{c\mathbf{q}}(k_x)}{dk_x} = -i\Delta_0 e^{-i\kappa k_x}\beta_{v\mathbf{q}}(k_x) \tag{5.13}$$

$$\frac{d\beta_{v\mathbf{q}}(k_x)}{dk_x} = -i\Delta_0 e^{i\kappa k_x}\beta_{c\mathbf{q}}(t), \tag{5.14}$$

where $\kappa = (E_c - E_v)/eF_c$. Solution of the system of equations (5.13)-(5.14) determines the relation between the coefficients $\hat{\beta}_L = (\beta_{c,L}, \beta_{v,L})$ at $k_x = k_{x,max} - \delta_x/2$ and coefficients $\hat{\beta}_R = (\beta_{c,R}, \beta_{v,R})$ at $k_x = k_{x,max} + \delta_x/2$,

$$\hat{\beta}_R = \hat{T}(\kappa)\hat{\beta}_L, \tag{5.15}$$

where $\hat{T}(\kappa)$ is the transfer matrix, which is given by the following expression

$$\hat{T}(\kappa) = i\hat{R}_\phi \hat{\Xi}_{\gamma,\Lambda}, \tag{5.16}$$

$$\hat{R}_\phi = \begin{pmatrix} e^{-i\phi} & 0 \\ 0 & e^{-i\phi} \end{pmatrix}, \tag{5.17}$$

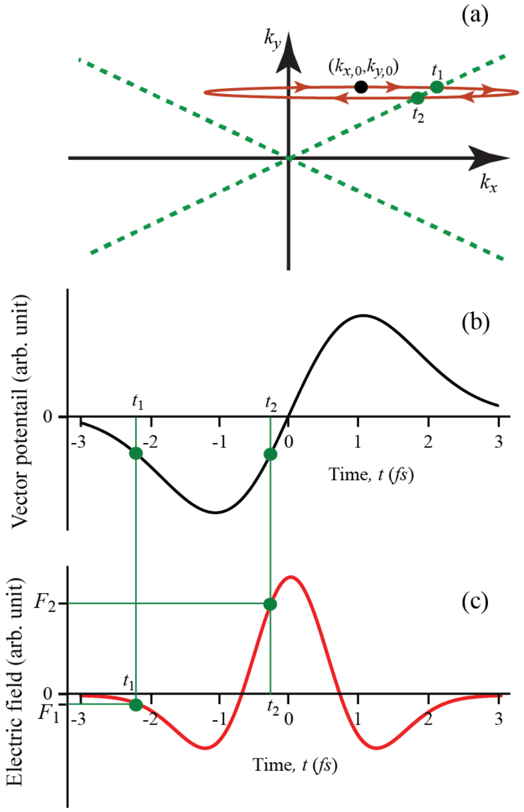

Figure (5.8) Illustration of electron interband dynamics for x-polarized optical pulse. (a) Dashed lines show the positions of the maxima of the interband dipole coupling. The red line illustrates the electron trajectory in the reciprocal space, where $(k_{x,0}, k_{y,0})$ is the initial electron wave vector. The electron trajectory passes twice the region of large interband coupling (dashed line) at two moments of time, t_1 and t_2. These passages are shown by green dots (for x-polarized pulse these points coincide, but for illustration purpose the dots are shifted in space). (b) Vector potential of the optical pulse as a function of time. The moments of time t_1 and t_2 are the same as in panel (a). At these moments the vector potential is the same. (c) The electric field of the optical pulse as a function of time. At the moments of time t_1 and t_2 the magnitudes of electric field are not the same, $F_2 > F_1$.

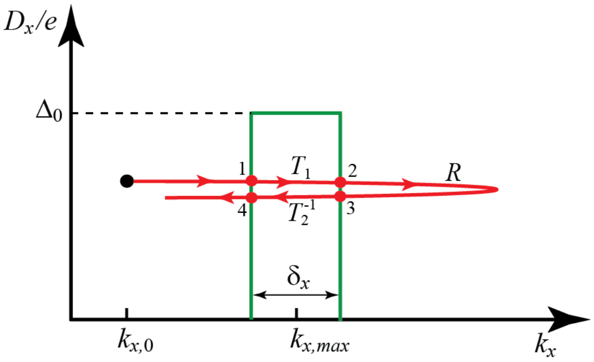

Figure (5.9) Approximation for the interband dipole coupling near the maximum. The width of the peak is δ_x and its height Δ_0. Red line illustrates part of the electron trajectory in the reciprocal space – see Fig. 5.8(a). The trajectory passes twice through the maximum of the interband coupling. Along the trajectory strong interband mixing occurs only between points "1" and "2", and "3" and "4". The values of $\hat{\beta}$ at points "2" and "1" are related by transfer matrix T_1, at points "2" and "3" - by accumulation of dynamic phase, which is described by rotational matrix R, and at points "3" and "4" - by transfer matrix T_2.

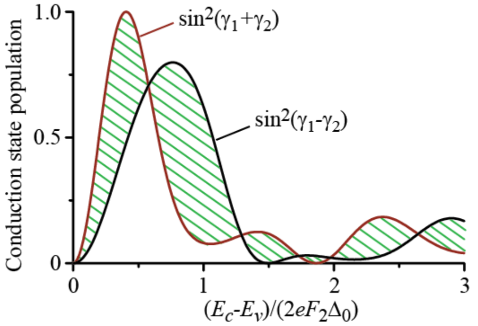

Figure (5.10) Residual population, $|\beta_c|^2$, of the conduction band state with initial wave vector $(k_{x,0}, k_{y,0})$ as a function of $\kappa_2/2\Delta_0 = (E_c - E_v)/(2eF_2\Delta_0)$. The parameter, κ_1, is $3\kappa_2$. The red line shows the function $\sin^2(\gamma_1 + \gamma_2)$, while the black line corresponds to $\sin^2(\gamma_1 - \gamma_2)$. Possible values of residual conduction band population are shown by dashed regions.

$$\hat{\Xi}_{\gamma,\Lambda} = \begin{pmatrix} -\cos\gamma e^{-\Lambda} & \sin\gamma \\ \sin\gamma & \cos\gamma e^{\Lambda} \end{pmatrix}. \tag{5.18}$$

Here the angles ϕ, γ, and Λ are defined by the following expressions

$$\phi = \kappa\delta_x, \tag{5.19}$$

$$\gamma = -\arcsin\left[\frac{\sin\left(\frac{\pi}{2}\sqrt{1+(\kappa/2\Delta_0)^2}\right)}{\sqrt{1+(\kappa/2\Delta_0)^2}}\right], \tag{5.20}$$

and

$$\Lambda = \arctan\left[\sqrt{1+\left(\frac{2\Delta_0}{\kappa}\right)^2}\cot\left(\frac{\pi}{2}\sqrt{1+\left(\frac{\kappa}{2\Delta_0}\right)^2}\right)\right]. \tag{5.21}$$

Then the electron interband dynamics along the trajectory shown in Fig. 5.9 by the red line is described by the following set of expressions: (i) between points "1" and "2" (see Fig. 5.9) the expansion coefficients $\hat{\beta}_2$ and $\hat{\beta}_1$ are related by the transfer matrix $\hat{T}(\kappa_1)$,

$$\hat{\beta}_2 = \hat{T}(\kappa_1)\hat{\beta}_1, \tag{5.22}$$

where $\kappa_1 = (E_c - E_v)/eF_1$. (ii) Between points "2" and "3" the interband dipole matrix element is zero, then the electron dynamics between these points is determined by accumulation of the dynamics phases without any interband mixing,

$$\hat{\beta}_3 = \hat{R}_\xi\hat{\beta}_2, \tag{5.23}$$

where angle $\xi = \int_{t_1}^{t_2} E_c(t)dt/\hbar$ depends on the path length between points "2" and "3". (iii) between points "3" and "4" the expansion coefficients $\hat{\beta}_3$ and $\hat{\beta}_4$ are related by the transfer matrix $\hat{T}(\kappa_2)$,

$$\hat{\beta}_4 = \hat{T}^{-1}(\kappa_2)\hat{\beta}_3, \tag{5.24}$$

where $\kappa_2 = (E_c - E_v)/eF_2$.

Combining relations (5.22)-(5.24), we obtain

$$\hat{\beta}_4 = \hat{T}^{-1}(\kappa_2)\hat{R}_\xi \hat{T}(\kappa_1)\hat{\beta}_1. \tag{5.25}$$

Substituting Eq. (5.16) into expression (5.25), we derive

$$\hat{\beta}_4 = \hat{\Xi}_{\gamma_2,-\Lambda_2}\hat{R}_{\xi+\phi_1-\phi_2}\hat{\Xi}_{\gamma_1,\Lambda_1}\hat{\beta}_1, \tag{5.26}$$

where the indexes 1 and 2 correspond to two values of electric field F_1 and F_2, respectively. Since $\beta_1 = (0, 1)$ (in the initial state the valence band is occupied), the residual conduction band population, which is the conduction band component of $\hat{\beta}_4$, is

$$\begin{aligned} |\beta_c|^2 &= \cos^2\gamma_2 \sin^2\gamma_1 + \cos^2\gamma_1 \sin^2\gamma_2 - \\ &\quad \frac{1}{2}\sin(2\gamma_1)\sin(2\gamma_2)\cos\varphi, \end{aligned} \tag{5.27}$$

where $\varphi = \Lambda_2 - \Lambda_1 + 2(\xi + \phi_1 - \phi_2)$, which depends on electron initial wave vectors. The magnitude of the residual conduction band population is in the range

$$\min\left\{\sin^2(\gamma_1-\gamma_2), \sin^2(\gamma_1+\gamma_2)\right\} < |\beta_c|^2 < \max\left\{\sin^2(\gamma_1-\gamma_2), \sin^2(\gamma_1+\gamma_2)\right\}. \tag{5.28}$$

The difference between γ_1 and γ_2 is in the value of electric field, all other parameters ($E_c - E_v$, Δ_0) are the same. The corresponding electric fields are shown in Fig. 5.8, where $F_2 > F_1$. In Fig. 5.10 we show $\sin^2(\gamma_1-\gamma_2)$ and $\sin^2(\gamma_1+\gamma_2)$ as a function of parameter $\kappa_2/2\Delta_0$ assuming that $\kappa_1 = 3\kappa_2$, i.e. $F_2 = 3F_1$. The possible values of $|\beta_c|^2$ are within the dashed region. Since the magnitude of Δ_0 is correlated with the position of the point along the dashed line of maxima [see Fig. 5.8(a)], i.e. with increasing k_y along the line of maxima, interband coupling Δ_0 decreases (at $k_y = 0$ $D_0 \to \infty$ and at $k_y \to \infty$ $D_0 = 0$), then the results shown in Fig. 5.10 illustrate the fact the maximum of $|\beta_c|^2$ is at finite distance from the degeneracy point, $k = 0$.

wave vector $(k_{x,0}, k_{y,0})$ as a function of $\kappa_2/2\Delta_0 = (E_c - E_v)/(2eF_2\Delta_0)$. The parameter, κ_1, is $3\kappa_2$. The red line shows the function $\sin^2(\gamma_1 + \gamma_2)$, while the black line corresponds to $\sin^2(\gamma_1 - \gamma_2)$. Possible values of residual conduction band population are shown by dashed regions.

5.3 Conclusion

Interband electron dynamics in ultrashort optical pulse strongly depends on the distribution of the interband dipole matrix elements in the reciprocal space. For the surface states of the crystalline topological insulator with quadratic gapless bands, the interband dipole matrix elements are singular at the degeneracy point and are anisotropic around this point. The distribution of the residual CB population in the reciprocal space is correlated with the corresponding distribution of the interband dipole matrix elements. Namely, the distribution of CB population shows high contrast peaks, localized near the local maximum of the interband dipole coupling. The number of high contrast peaks in $N_{CB}^{(res)}$ is correlated with the number of peaks in the dipole matrix elements as a function of wave vector along the direction of pulse polarization. The number of peaks changes from four to two with a rotation of the polarization direction.

The ultrashort optical pulse causes the charge transfer through the system. The charge is transferred in the direction of the maximum field. The magnitude of the transferred charge depends on the amplitude of the pulse and the direction of the pulse polarization.

CHAPTER 6

SUMMARY

In this dissertation we studied ultrafast processes in three different types of 2D materials, graphene, topological insulators, and crystalline topological insulators subjected to ultrafast laser pulses.

Graphene is shined by linear polarized pulses and the electric field waveforms of the applied pulses have strong effect on the dynamic of electrons. Electron dynamics in graphene is highly irreversible and strongly depends on the waveform of the applied pulse. This irreversibility is due to both the gapless electronic structure of graphene and the singularity of the interband dipole matrix element at the Dirac points. The ultrashort optical pulse causes the charge transfer through the system. The direction of transferred charge is in the direction of the field maximum or in the opposite direction depending on the waveform and the amplitude of the applied pulse.

We study ultrafast electron dynamics of a 2D electron system on the surface of a 3D topological insulator. The electron dynamics in such system is highly irreversible and anisotropic. The irreversibility of the electron dynamics is due to zero band gap of the surface states. In this case, the interaction of the laser pulse with the system satisfies the nonadiabatic condition, $\omega_0 >> \Delta_g/\hbar$, where ω_0 is the laser frequency and Δ_g is the band gap. The anisotropy is due to cubic terms in the effective Hamiltonian of the system, which results in the anisotropy of the interband dipole matrix elements near the Dirac point. Such anisotropy produces hot spots in the distribution of the conduction band population in the reciprocal space, where the number of the spots depends on the polarization of the optical pulse. Redistribution of the electrons between the conduction and valence bands generates the electric current during the pulse. The magnitude of the current is also anisotropic and depends on the polarization of the pulse. Moreover, for a circularly polarized light the response of the system, unlike graphene, depends on the chirality (helicity) of the incident pulse. This is due to the hexagonal warping terms which are responsible for breaking full rotational symmetry down to three-fold rotational symmetry. Additionally, due to the spin-momentum locking, there is spin current in addition to the charge current. we calculated the transferred spin which can be used in spintronics applications.

The crystalline topological insulator has a quadratic energy dispersion at the gamma point unlike graphene which has linear energy dispersion near the Dirac points. For the surface states of a a 3D crystalline topological insulator with quadratic gappless bands, the interband dipole matrix elements are singular at the degeneracy point and are anisotropic around this point. In the presence of an ultrafast linear polarized pulse the distribution of the residual conduction band population in the reciprocal space is correlated with the corresponding distribution of the interband dipole matrix elements. Namely, the distribution of conduction band population shows high contrast peaks, localized near the local maximum of the interband dipole coupling. The number of high contrast peaks in residual conduction band population is correlated with the number of peaks in the dipole matrix elements as a function of wave vector along the direction of pulse polarization. The number of peaks changes from four to two with rotation of the polarization direction. The ultrashort optical pulse causes the charge transfer through the system. The charge is transferred in the direction of the maximum field. The magnitude of the transferred charge depends on the amplitude of the pulse and the direction of the pulse polarization.

REFERENCES

[1] C.-X. Liu, X.-L. Qi, H. Zhang, X. Dai, Z. Fang, and S.-C. Zhang, "Model hamiltonian for topological insulators," *Phys. Rev. B*, vol. 82, p. 045122, 2010.

[2] S. S. Mao, F. Quere, S. Guizard, X. Mao, R. E. Russo, G. Petite, and P. Martin, "Dynamics of femtosecond laser interactions with dielectrics," *Applied Physics a Materials Science and Processing*, vol. 79, no. 7, pp. 1695–1709, 2004.

[3] H. Fattahi, H. G. Barros, M. Gorjan, T. Nubbemeyer, B. Alsaif, C. Y. Teisset, M. Schultze, S. Prinz, M. Haefner, M. Ueffing, A. Alismail, L. Vmos, A. Schwarz, O. Pronin, J. Brons, X. T. Geng, G. Arisholm, M. Ciappina, V. S. Yakovlev, D.-E. Kim, A. M. Azzeer, N. Karpowicz, D. Sutter, Z. Major, T. Metzger, and F. Krausz, "Third-generation femtosecond technology," *Optica*, vol. 1, no. 1, pp. 45–63, 2014.

[4] A. Schiffrin, T. Paasch-Colberg, N. Karpowicz, V. Apalkov, D. Gerster, S. Muhlbrandt, M. Korbman, J. Reichert, M. Schultze, S. Holzner, J. V. Barth, R. Kienberger, R. Ernstorfer, V. S. Yakovlev, M. I. Stockman, and F. Krausz, "Optical-field-induced current in dielectrics," *Nature*, vol. 493, no. 7430, pp. 70–74, 2013.

[5] M. Schultze, E. M. Bothschafter, A. Sommer, S. Holzner, W. Schweinberger, M. Fiess, M. Hofstetter, R. Kienberger, V. Apalkov, V. S. Yakovlev, M. I. Stockman, and F. Krausz, "Controlling dielectrics with the electric field of light," *Nature*, vol. 493, no. 7430, pp. 75–8, 2013.

[6] A. V. Mitrofanov, A. J. Verhoef, E. E. Serebryannikov, J. Lumeau, L. Glebov, A. M. Zheltikov, and A. Baltuška, "Optical detection of attosecond ionization induced by a few-cycle laser field in a transparent dielectric material," *Phys. Rev. Lett.*, vol. 106, pp. 147 401–1–4, 2011.

[7] E. Goulielmakis, V. S. Yakovlev, A. L. Cavalieri, M. Uiberacker, V. Pervak, A. Apolon-

ski, R. Kienberger, U. Kleineberg, and F. Krausz, “Attosecond control and measurement: Lightwave electronics,” *Science*, vol. 317, pp. 769–775, 2007.

[8] P. Balling and J. Schou, “Femtosecond-laser ablation dynamics of dielectrics: basics and applications for thin films,” *Reports on Progress in Physics*, vol. 76, no. 3, p. 036502, 2013.

[9] V. S. Yakovlev, T. Kruchinin, Stanislav Yu.and Paasch-Colberg, and F. Stockman, Mark I.and Krausz, “Ultrafast control of strong-field electron dynamics in solids,” *eprint arXiv:1502.02180*, 2015.

[10] A. Kaiser, B. Rethfeld, M. Vicanek, and G. Simon, “Microscopic processes in dielectrics under irradiation by subpicosecond laser pulses,” *Phys. Rev. B*, vol. 61, pp. 11 437–11 450, 2000.

[11] L. V.Keldysh, “Ionization in the field of a strong electromagnetic wave,” *Soviet Physics JETP*, vol. 20, no. 5, pp. 1307–1314, 1965.

[12] C. Baozhen, “A new derivation of keldysh’s formula,” *Chinese Physics Letters*, vol. 7, no. 5, p. 219, 1990.

[13] M. Gertsvolf, M. Spanner, D. M. Rayner, and P. B. Corkum, “Demonstration of attosecond ionization dynamics inside transparent solids,” *J. Phys. B*, vol. 43, pp. 131 002–1–5, 2010.

[14] M. Lenzner, J. Kruger, S. Sartania, Z. Cheng, C. Spielmann, G. Mourou, W. Kautek, and F. Krausz, “Femtosecond optical breakdown in dielectrics,” *Phys. Rev. Lett.*, vol. 80, pp. 4076–4079, 1998.

[15] R. H. Fowler and L. Nordheim, “Electron emission in intense electric fields,” *Proc. Royal Soc. London. Ser. A*, vol. 119, pp. 173–181, 1928.

[16] C. Zener, “A theory of the electrical breakdown of solid dielectrics,” *Proc. Royal Soc. A*, vol. 145, pp. 523–529, 1934.

[17] L. V. Keldysh, "Behavior of non-metalic crystals in strong electric fields," *J. Exptl. Theor. Phys. 33, 763-770 (1957); Translation: Sov. Phys. JETP*, vol. 6, pp. 994–1003, 1958.

[18] G. H. Wannier, "Wave functions and effective Hamiltonian for Bloch electrons in an electric field," *Phys. Rev.*, vol. 117, pp. 432–439, 1960.

[19] M. Lenzlinger and E. H. Snow, "Fowler-nordheim tunneling into thermally grown sio[sub 2]," *J. Appl. Phys.*, vol. 40, pp. 278–283, 1969.

[20] M. Kruger, M. Schenk, and P. Hommelhoff, "Attosecond control of electrons emitted from a nanoscale metal tip," *Nature*, vol. 475, pp. 78–81, 2011.

[21] S. Ghimire, A. D. DiChiara, E. Sistrunk, P. Agostini, L. F. DiMauro, and D. A. Reis, "Observation of high-order harmonic generation in a bulk crystal," *Nature Phys.*, vol. 7, pp. 138–141, 2011.

[22] M. Durach, A. Rusina, M. F. Kling, and M. I. Stockman, "Metallization of nanofilms in strong adiabatic electric fields," *Phys. Rev. Lett.*, vol. 105, pp. 086 803–1–4, 2010.

[23] L. Miaja-Avila, C. Lei, M. Aeschlimann, J. L. Gland, M. M. Murnane, H. C. Kapteyn, and G. Saathoff, "Laser-assisted photoelectric effect from surfaces," *Phys. Rev. Lett.*, vol. 97, pp. 113 604–1–4, 2006.

[24] M. Durach, A. Rusina, M. F. Kling, and M. I. Stockman, "Predicted ultrafast dynamic metallization of dielectric nanofilms by strong single-cycle optical fields," *Phys. Rev. Lett.*, vol. 107, pp. 086 602–1–5, 2011.

[25] A. Schiffrin, T. Paasch-Colberg, N. Karpowicz, V. Apalkov, D. Gerster, S. Muhlbrandt, M. Korbman, J. Reichert, M. Schultze, S. Holzner, J. V. Barth, R. Kienberger, R. Ernstorfer, V. S. Yakovlev, M. I. Stockman, and F. Krausz, "Optical-field-induced current in dielectrics," *Nature*, vol. 493, pp. 70–74, 2012.

[26] V. Apalkov and M. I. Stockman, “Theory of dielectric nanofilms in strong ultrafast optical fields,” *Phys. Rev. B*, vol. 86, pp. 165 118–1–13, 2012.

[27] ——, “Metal nanofilm in strong ultrafast optical fields,” *Phys. Rev. B*, vol. 88, pp. 245 438–1–7, 2013.

[28] H. K. Kelardeh, V. Apalkov, and M. I. Stockman, “Graphene in ultrafast and superstrong laser fields,” *Phys. Rev. B*, vol. 91, no. 4, p. 045439, 2015.

[29] ——, “Ultrafast field control of symmetry, reciprocity, and reversibility in buckled graphene-like materials,” *Phys. Rev. B*, vol. 92, no. 4, p. 045413, 2015.

[30] T. Otobe, M. Yamagiwa, J.-I. Iwata, K. Yabana, T. Nakatsukasa, and G. F. Bertsch, “First-principles electron dynamics simulation for optical breakdown of dielectrics under an intense laser field,” *Phys. Rev. B*, vol. 77, p. 165104, Apr 2008.

[31] V. Véniard, R. Taïeb, and A. Maquet, “Atomic clusters submitted to an intense short laser pulse: A density-functional approach,” *Phys. Rev. A*, vol. 65, p. 013202, Dec 2001.

[32] K. Yabana, T. Sugiyama, Y. Shinohara, T. Otobe, and G. F. Bertsch, “Time-dependent density functional theory for strong electromagnetic fields in crystalline solids,” *Phys. Rev. B*, vol. 85, pp. 045 134–1–11, 2012.

[33] P. J. Hasnip, K. Refson, M. I. J. Probert, J. R. Yates, S. J. Clark, and C. J. Pickard, “Density functional theory in the solid state,” *Philos Trans A Math Phys Eng Sci*, vol. 372, no. 2011, 2014.

[34] B. Chimier, O. Utza, N. Sanner, M. Sentis, T. Itina, P. Lassonde, F. Lgar, F. Vidal, and J. C. Kieffer, “Damage and ablation thresholds of fused-silica in femtosecond regime,” *Phys. Rev. B*, vol. 84, pp. 094 104–1–10, 2011.

[35] H. K. Kelardeh, V. Apalkov, and M. I. Stockman, “Graphene in ultrafast and superstrong laser fields,” *Phys. Rev. B*, vol. 91, pp. 0 454 391–8, 2015.

[36] A. Kara, H. Enriquez, A. P. Seitsonen, L. C. Lew Yan Voon, S. Vizzini, B. Aufray, and H. Oughaddou, “A review on silicene new candidate for electronics,” *Surf. Sci. Rep.*, vol. 67, no. 1, pp. 1–18, 2012.

[37] Q. Tang and Z. Zhou, “Graphene-analogous low-dimensional materials,” *Progr. Mater. Sci.*, vol. 58, no. 8, pp. 1244–1315, 2013.

[38] H. Rostami, A. Moghaddam, and R. Asgari, “Effective lattice hamiltonian for monolayer mos2: Tailoring electronic structure with perpendicular electric and magnetic fields,” *Phys. Rev. B*, vol. 88, no. 8, p. 085440, 2013.

[39] K. Takeda and K. Shiraishi, “Theoretical possibility of stage corrugation in si and ge analogs of graphite,” *Phys. Rev. B*, vol. 50, no. 20, pp. 14 916–14 922, 1994.

[40] C.-C. Liu, W. Feng, and Y. Yao, “Quantum spin hall effect in silicene and two-dimensional germanium,” *Phys. Rev. Lett.*, vol. 107, no. 7, p. 076802, 2011.

[41] C.-C. Liu, H. Jiang, and Y. Yao, “Low-energy effective hamiltonian involving spin-orbit coupling in silicene and two-dimensional germanium and tin,” *Phys. Rev. B*, vol. 84, no. 19, p. 195430, 2011.

[42] Y. Wang, J. Zheng, Z. Ni, R. Fei, Q. Liu, R. Quhe, C. Xu, J. Zhou, Z. Gao, and J. Lu, “Half-metallic silicene and germanene nanoribbons: Towards high-performance spintronics device,” *Nano*, vol. 07, no. 05, p. 1250037, 2012.

[43] F.-b. Zheng and C.-w. Zhang, “The electronic and magnetic properties of functionalized silicene: a first-principles study,” *Nanoscale Res. Lett.*, vol. 7, no. 1, p. 422, 2012.

[44] H. K. Kelardeh, V. Apalkov, and M. I. Stockman, “Ultrafast field control of symmetry, reciprocity, and reversibility in buckled graphene-like materials,” *Phys. Rev. B*, vol. 92, pp. 045 413–1–9, 2015.

[45] O. Kwon, T. Paasch-Colberg, V. Apalkov, B.-K. Kim, J.-J. Kim, M. I. Stockman, and D. E. Kim, “Semimetallization of dielectrics in strong optical fields,” *Sci. Rep.*, vol. 6, pp. 21 272–1–9, 2016.

[46] T. Paasch-Colberg, S. Y. Kruchinin, O. Saglam, S. Kapser, S. Cabrini, S. Muehlbrandt, J. Reichert, J. V. Barth, R. Ernstorfer, R. Kienberger, V. S. Yakovlev, N. Karpowicz, and A. Schiffrin, “Sub-cycle optical control of current in a semiconductor: from the multiphoton to the tunneling regime,” *Optica*, vol. 3, no. 12, pp. 1358–1361, 2016.

[47] T. Higuchi, C. Heide, K. Ullmann, H. B. Weber, and P. Hommelhoff, “Light-field-driven currents in graphene,” *Nature*, vol. 550, no. 7675, pp. 224–228, 2017.

[48] S. A. O. Motlagh, J.-S. Wu, V. Apalkov, and M. I. Stockman, “Ultrafast control of electron dynamics in 3d topological insulator,” *Journal of Physics: Conference Series*, vol. 906, no. 1, p. 012012, 2017.

[49] S. A. Oliaei Motlagh, V. Apalkov, and M. I. Stockman, “Interaction of crystalline topological insulator with an ultrashort laser pulse,” *Phys. Rev. B*, vol. 95, p. 085438, Feb 2017.

[50] F. Bloch, “Über die Quantenmechanik der Elektronen in Kristallgittern,” *Z. Phys. A*, vol. 52, pp. 555–600, 1929.

[51] P. W. LANGHOFF, S. T. EPSTEIN, and M. KARPLUS, “Aspects of time-dependent perturbation theory,” *Rev. Mod. Phys.*, vol. 44, pp. 602–644, Jul 1972.

[52] S. C. Miller and R. H. Good, “A wkb-type approximation to the schrödinger equation,” *Phys. Rev.*, vol. 91, pp. 174–179, Jul 1953.

[53] P. Bracken, “A Time Dependent Version of the Quantum WKB Approximation,” *ArXiv Mathematical Physics e-prints*, Aug. 2006.

[54] M. Breusing, S. Kuehn, T. Winzer, E. Malic, F. Milde, N. Severin, J. P. Rabe, C. Ropers, A. Knorr, and T. Elsaesser, "Ultrafast nonequilibrium carrier dynamics in a single graphene layer," *Physical Review B*, vol. 83, no. 15, p. 153410, 2011.

[55] K. J. Tielrooij, J. C. W. Song, S. A. Jensen, A. Centeno, A. Pesquera, A. Z. Elorza, M. Bonn, L. S. Levitov, and F. H. L. Koppens, "Photoexcitation cascade and multiple hot-carrier generation in graphene," *Nat. Phys.*, vol. 9, pp. 248–252, 2013.

[56] D. Brida, A. Tomadin, C. Manzoni, Y. J. Kim, A. Lombardo, S. Milana, R. R. Nair, K. S. Novoselov, A. C. Ferrari, G. Cerullo, and M. Polini, "Ultrafast collinear scattering and carrier multiplication in graphene," *Nat. Commun.*, vol. 4, 2013.

[57] I. Gierz, J. C. Petersen, M. Mitrano, C. Cacho, I. C. Turcu, E. Springate, A. Stohr, A. Kohler, U. Starke, and A. Cavalleri, "Snapshots of non-equilibrium Dirac carrier distributions in graphene," *Nat. Mater.*, vol. 12, no. 12, pp. 1119–24, 2013.

[58] M. W. Graham, S. F. Shi, D. C. Ralph, J. Park, and P. L. McEuen, "Photocurrent measurements of supercollision cooling in graphene," *Nat. Phys.*, vol. 9, pp. 103–108, 2013.

[59] J. C. Johannsen, S. Ulstrup, F. Cilento, A. Crepaldi, M. Zacchigna, C. Cacho, I. C. E. Turcu, E. Springate, F. Fromm, C. Raidel, T. Seyller, F. Parmigiani, M. Grioni, and P. Hofmann, "Direct view of hot carrier dynamics in graphene," *Phys. Rev. Lett.*, vol. 111, p. 027403, 2013.

[60] I. Gierz, F. Calegari, S. Aeschlimann, M. Chavez Cervantes, C. Cacho, R. T. Chapman, E. Springate, S. Link, U. Starke, C. R. Ast, and A. Cavalleri, "Tracking primary thermalization events in graphene with photoemission at extreme time scales," *Physical Review Letters*, vol. 115, no. 8, p. 086803, 2015.

[61] J. C. Johannsen, S. Ulstrup, A. Crepaldi, F. Cilento, M. Zacchigna, J. A. Miwa, C. Cacho, R. T. Chapman, E. Springate, F. Fromm, C. Raidel, T. Seyller, P. D. C. King,

F. Parmigiani, M. Grioni, and P. Hofmann, “Tunable carrier multiplication and cooling in graphene,” *Nano Letters*, vol. 15, no. 1, pp. 326–331, 2015.

[62] J. C. Butcher, “Coefficients for the study of runge-kutta integration processes,” *Journal of the Australian Mathematical Society*, vol. 3, no. 2, p. 185201, 1963.

[63] W. V. Houston, “Acceleration of electrons in a crystal lattice,” *Phys. Rev.*, vol. 57, pp. 184–186, 1940.

[64] C. Meador and A. S. Sarra, “A comparison of two 4th-order numerical ordinary differential equation methods applied to the rabinovich-fabrikant equations,” 2009.

[65] J. Defrutos and J. M. Sanzserna, “An easily implementable 4th-order method for the time integration of wave problems,” *Journal of Computational Physics*, vol. 103, no. 1, pp. 160–168, 1992.

[66] W. H. Press, S. A. Flannery, B. P.and Teukolsky, and W. T. Vetterling, *Numerical Recipes in FORTRAN: The Art of Scientific Computing, 2nd ed.* Cambridge, England: Cambridge University Press, 1992.

[67] T. Kimura, “On dormand-prince method,” 2009.

[68] D. Houcque, “Applications of matlab:ordinary differential equations (ode),” 2008.

[69] G. Sharma and J. Martin, “Matlab(a (r)): A language for parallel computing,” *International Journal of Parallel Programming*, vol. 37, no. 1, pp. 3–36, 2009.

[70] R. Choy and A. Edelman, “Parallel matlab: Doing it right,” *Proceedings of the Ieee*, vol. 93, no. 2, pp. 331–341, 2005.

[71] K. Jeremy and S. Ahalt, “Matlabmpi,” *Journal of Parallel and Distributed Computing*, vol. 64, no. 8, pp. 997–1005, 2004.

[72] M. Tripathy and C. R. Tripathy, “A comparative analysis of performance of shared memory cluster computing interconnection systems,” *Journal of Computer Networks and Communications*, vol. 2014, p. 9, 2014.

[73] S. Bagga, A. Girdhar, and M. C. Trivedi, “Spmd based time sharing intelligent approach for image denoising,” *Journal of Intelligent Fuzzy Systems*, vol. 32, no. 5, pp. 3561–3573, 2017.

[74] A. K. Geim and K. S. Novoselov, “The rise of graphene,” *Nat Mater*, vol. 6, no. 3, pp. 183–191, 2007.

[75] J. W. Jiang, “Graphene versus mos2: A short review,” *Frontiers of Physics*, vol. 10, no. 3, pp. 287–302, 2015.

[76] F. Schwierz, “Graphene transistors,” *Nature Nanotechnology*, vol. 5, no. 7, pp. 487–496, 2010.

[77] A. H. C. Neto, F. Guinea, N. M. R. Peres, K. S. Novoselov, and A. K. Geim, “The electronic properties of graphene,” *Rev. Mod. Phys.*, vol. 81, pp. 109–162, 2009.

[78] A. OHare, F. V. Kusmartsev, and K. I. Kugel, “A stable flat form of two-dimensional crystals: Could graphene, silicene, germanene be minigap semiconductors?” *Nano Letters*, vol. 12, no. 2, pp. 1045–1052, 2012.

[79] S. M.-M. Dubois, Z. Zanolli, X. Declerck, and J.-C. Charlier, “Electronic properties and quantum transport in graphene-based nanostructures,” *The European Physical Journal B*, vol. 72, no. 1, pp. 1–24, Nov 2009.

[80] J. C. Slonczewski and P. R. Weiss, “Band structure of graphite,” *Phys. Rev.*, vol. 109, pp. 272–279, 1958.

[81] S. Das Sarma, S. Adam, E. H. Hwang, and E. Rossi, “Electronic transport in two-dimensional graphene,” *Reviews of Modern Physics*, vol. 83, no. 2, pp. 407–470, 2011.

[82] J. P. Sethna, “Order Parameters, Broken Symmetry, and Topology,” *eprint arXiv:cond-mat/9204009*, Apr. 1992.

[83] X.-L. Qi and S.-C. Zhang, “Topological insulators and superconductors,” *Rev. Mod. Phys.*, vol. 83, pp. 1057–1110, Oct 2011.

[84] M. Z. Hasan and C. L. Kane, “Colloquium: Topological insulators,” *Rev. Mod. Phys.*, vol. 82, pp. 3045–3067, Nov 2010.

[85] K. v. Klitzing, G. Dorda, and M. Pepper, “New method for high-accuracy determination of the fine-structure constant based on quantized hall resistance,” *Phys. Rev. Lett.*, vol. 45, pp. 494–497, Aug 1980.

[86] F. D. M. Haldane, “Nobel lecture: Topological quantum matter,” *Rev. Mod. Phys.*, vol. 89, p. 040502, Oct 2017.

[87] J. Moore, “Topological insulators: The next generation,” *Nature Physics*, vol. 5, pp. 378–380, Jun. 2009.

[88] J. E. Moore, “The birth of topological insulators,” *Nature*, vol. 464, no. 7286, pp. 194–198, 2010.

[89] R. J. Cava, H. Ji, M. K. Fuccillo, Q. D. Gibson, and Y. S. Hor, “Crystal structure and chemistry of topological insulators,” *J. Mater. Chem. C*, vol. 1, pp. 3176–3189, 2013.

[90] Y. D. Glinka, S. Babakiray, T. A. Johnson, M. Holcomb, and D. Lederman, “Resonance-type thickness dependence of optical second harmonic generation in thin-films of the topological insulator bi2se3,” *Physical Review B*, vol. 91, 04 2015.

[91] H. Zhang, C.-X. Liu, X.-L. Qi, X. Dai, Z. Fang, and S.-C. Zhang, “Topological insulators in Bi2Se3, Bi2Te3 and Sb2Te3 with a single Dirac cone on the surface,” *Nature Phys.*, vol. 5, pp. 438–442, 2009.

[92] ——, “Topological insulators in bi2se3, bi2te3 and sb2te3 with a single dirac cone on the surface,” *Nature Physics*, vol. 5, p. 438, 2009.

[93] W. X. Feng and Y. G. Yao, “Three-dimensional topological insulators: A review on host materials,” *Science China-Physics Mechanics Astronomy*, vol. 55, no. 12, pp. 2199–2212, 2012.

[94] C.-X. Liu, X.-L. Qi, H. Zhang, X. Dai, Z. Fang, and S.-C. Zhang, “Model hamiltonian for topological insulators,” *Phys. Rev. B*, vol. 82, p. 045122, Jul 2010.

[95] L. , “Hexagonal warping effects in the surface states of the topological insulator bi_2te_3,” *Phys. Rev. Lett.*, vol. 103, p. 266801, Dec 2009.

[96] L. Fu, “Topological crystalline insulators,” *Phys. Rev. Lett.*, vol. 106, no. 10, p. 106802, 2011.

[97] Y. Ando and L. Fu, “Topological Crystalline Insulators and Topological Superconductors: From Concepts to Materials,” *Annual Review of Condensed Matter Physics*, vol. 6, pp. 361–381, Mar. 2015.

[98] T. H. Hsieh, H. Lin, J. Liu, W. Duan, A. Bansil, and L. Fu, “Topological crystalline insulators in the snte material class,” *Nature communications*, vol. 3, p. 982, 2012.